



University  
of Glasgow

Qin, Ning (1987) *Towards numerical simulation of hypersonic flow around space-plane shapes.*

PhD thesis

<http://theses.gla.ac.uk/4412/>

Copyright and moral rights for this thesis are retained by the author

A copy can be downloaded for personal non-commercial research or study, without prior permission or charge

This thesis cannot be reproduced or quoted extensively from without first obtaining permission in writing from the Author

The content must not be changed in any way or sold commercially in any format or medium without the formal permission of the Author

When referring to this work, full bibliographic details including the author, title, awarding institution and date of the thesis must be given

TOWARDS NUMERICAL SIMULATION OF HYPERSONIC FLOW  
AROUND SPACE-PLANE SHAPES

by

QIN Ning, B.Sc., M.Sc.

Thesis submitted to the Faculty of Engineering,  
the University of Glasgow for the degree of Doctor of Philosophy

October 1987

© N. Qin, 1987

*To*  
*My parents*

## CONTENTS

<b>Acknowledgements</b>	iv
<b>Declaration</b>	v
<b>Summary</b>	vi
<b>Nomenclature</b>	viii
<b>Chapter One: Introduction</b>	<b>1</b>
1.1 Hypersonic Interest and Projected Spacecraft	1
1.2 Classification and Modelling of Hypersonic Flow	2
1.3 Wind Tunnel Experimentation and Hypersonic CFD	4
1.4 Aim and Approaches of This Study	7
1.5 Arrangement of the Thesis	11
<b>Chapter Two: Governing Equations</b>	<b>12</b>
2.1 Introduction	12
2.2 Compressible N–S Equations in Cartesian Coordinates	13
2.3 Compressible N–S Equations in Spherical Coordinates	16
2.4 Locally Conical Navier–Stokes Equations (LCNSE)	19
2.4.1 definition of conical flow	19
2.4.2 locally conical approximation	20
2.4.3 derivation of LCNSE	20
2.4.4 non–dimensionalization of LCNSE	22
2.5 Conical Euler Equations (CEE)	25
2.6 Initial and Boundary Conditions	27
2.6.1 boundary conditions	27
2.6.2 initial conditions	28

<b>Chapter Three: Numerical Methods</b>	<b>29</b>
3.1 Introduction	29
3.2 Review of Existing Numerical Schemes	30
3.2.1 time marching approach	30
3.2.2 time discretization: explicit or implicit ?	31
3.2.3 spatial discretization: central or upwind ?	33
3.2.4 multigrid acceleration	35
3.3 Implicit Solution of LCNSE	36
3.3.1 MacCormack implicit scheme for LCNSE	36
3.3.2 a simplified Beam– Warming implicit scheme for LCNSE	44
3.3.3 a comparative study of the two implicit schemes	50
3.4 Multigrid Acceleration of the Implicit Schemes	53
3.4.1 Ni– type multigrid acceleration of the MacCormack implicit scheme	53
3.4.2 FAS multigrid acceleration of the simplified Beam– Warming implicit scheme	56
3.5 Sparse Quasi– Newton Method for Fast Steady State Solution	61
3.5.1 motivation	61
3.5.2 general procedure of the sparse quasi– Newton method for steady state solutions	62
3.5.3 formulation for three– point and five– point schemes	66
3.5.4 application to flux splitting and TVD schemes for a nozzle problem	69
3.6 Concluding Remarks	76
 <b>Chapter Four: Hypersonic Flow Simulations</b>	 <b>78</b>
4.1 Introduction	78
4.2 Hypersonic Flow around Cones	80
4.2.1 computational conditions	80
4.2.2 flow field simulation	81

4.3	Hypersonic Flow on the Leaside of Delta Wings	83
4.3.1	computational conditions	83
4.3.2	flow field simulation	86
4.4	Hypersonic Flow beneath/over Cone– Delta– Wing Combinations	88
4.4.1	computational conditions	88
4.4.2	windward side flow field simulation	90
4.4.3	exploration of leeward side interaction	94
4.4.4	Euler solutions	94
4.5	Concluding Remarks	96
 <b>Chapter Five: Conclusions and Future Work</b>		 98
5.1	Numerical Aspects	98
5.2	Physical Aspects	101
5.3	Recommendations and Future Work	103
 <b>Appendices:</b>		 105
A.	Jacobians for LCNSE	105
B.	Diagonalization of $A_I$ and $B_I$	107
C.	Adaptive Artificial Viscosity	109
D.	Some Fourier Stability Analyses	111
D.1	Source Term Influence on Stability	111
D.2	Stability Condition with Explicit Diffusion Term	113
E.	Time Step Dependence of Steady State Solution with MacCormack– Type Schemes	115
F.	Distribution Formula for Equations with Source Term	118
 <b>References</b>		 119
 <b>Figures</b>		

## ACKNOWLEDGMENTS

The author wishes to express his sincere gratitude to Professor Bryan E. Richards, Department of Aeronautics and Fluid Mechanics, for his guidance and support during his supervision of the research.

The author gratefully acknowledges Professor Henry Y. Wong for his help in many aspects to the author during this period. Thanks are also due to Dr. Jiang Dachun for valuable discussion which remains as a source of enlightenment and inspiration during this research, to Mr. Nick Brittain for proofreading the draft of this thesis, to Mrs. Effie Murray-Smith and Miss Margaret Simpson, secretary to the department, for their kind help and to the staff of Glasgow University Computing Centre, especially to Dr. Bert Welsh, for their excellent service.

Among many others, the author is deeply indebted to Professor Cao Qipeng of NAI for his early education, which directed the author to this fascinating area.

Finally, the author would like to express his sincere thanks to his parents for their continuous encouragement.

The author was supported by the Glasgow University Scholarship and an ORS award during this period of research.

DECLARATION

The author declares that the research contained in this thesis was carried out by the author independently during the period from December 1984 to October 1987.

A handwritten signature in blue ink, consisting of two characters: '宁' (Ning) and '琴' (Qin).

QIN Ning

## SUMMARY

This thesis reports research carried out towards numerical simulation of hypersonic flows around space-plane shapes. For high speed flows around conical geometries, a locally conical approximation was introduced, which resulted in locally conical Navier-Stokes equations.

In order to achieve accuracy and efficiency for steady state solutions, various methods were investigated. Based on the MacCormack implicit scheme and the Beam-Warming implicit scheme, two implicit procedures were developed to solve the locally conical Navier-Stokes equations (LCNSE). A new implicit boundary treatment was introduced in the MacCormack implicit scheme. The source term in the governing equations was treated explicitly. A simplified Beam-Warming implicit scheme was developed for its application to the LCNSE. Accuracy of the two schemes was investigated. The time step dependence of steady state solution with MacCormack-type schemes was analyzed and a procedure to reduce the error was proposed.

To further accelerate the convergence to the steady state, two multigrid methods were applied to the two implicit schemes respectively. An extension of Ni-type multigrid method was developed to accelerate the MacCormack implicit scheme, and the FAS multigrid method was employed to accelerate the simplified Beam-Warming implicit scheme.

In parallel, a new approach for fast steady state solution — sparse quasi-Newton method — was proposed to avoid difficulties in linearization associated with implicit schemes for general CFD problems. Formulation was given for three-point and five-point spatial discretization schemes. Preliminary results of a nozzle problem with van Leer's flux splitting and Harten's TVD high shock-resolution schemes illustrated significantly faster convergence to steady state with the sparse quasi-Newton approach than those with corresponding implicit operators of van Leer and Harten.

Numerical simulations by solving LCNSE with the two implicit schemes developed in this study were carried out on hypersonic flows around a cone, on the leeward side of a delta wing and beneath/over a cone-delta-wing combination. Detailed structures of the complex flow interaction were well predicted including the existence of embedded shock waves and secondary vortices. Comparison with available experimental data was made. Euler solutions were also carried out to compare with the N-S solutions.

In the present hypersonic delta wing flow simulation, different phenomena were found than would have been expected from the Miller and Wood classification in the lower speed range.

The numerical simulation of hypersonic viscous flows around a cone-delta-wing combination was the first flow field simulation around such a shape representing wing-body interference. It was found that the complexity of the flow field results from the shock-shock, shock-boundary layer and shock-vortex interactions in the flow field. High local heating and its cause were revealed near the corner on both the windward side and the leeward side surfaces of the geometry.

## NOMENCLATURE

$A^k$	Jacobian approximation in sparse quasi-Newton method
$A_I$	inviscid Jacobian, $\partial F_I/\partial U$
$ A $	matrix defined in (3-4)
$B_I$	inviscid Jacobian, $\partial G_I/\partial U$
$ B $	matrix defined in (3-4)
$c$	speed of sound
$C_I$	inviscid Jacobian, $\partial H/\partial U$
$C_p$	surface pressure coefficient, $(p_w - p_\infty)/(1/2)\rho_\infty  V _\infty^2$ , at $r$
$c_p$	specific heat at constant pressure
$D_A, D_B$	matrices defined in (3-5)
$e$	total internal energy
$E$	$x$ or $r$ direction flux vector
$F$	$y$ or $\theta$ direction flux vector
$F_I$	inviscid flux vector
$G$	$z$ or $\varphi$ direction flux vector
$G_I$	inviscid flux vector
$H$	source term vector
$H_I$	inviscid source term
$J(U)$	Jacobian, $\partial R(U)/\partial U$
$k$	thermal conductivity
$M$	Mach number
$n$	normal direction
$Pr$	Prandtl number, $c_p\mu/k$
$P_z(M)$	matrix projection defined in (3-80)
$p$	pressure
$q$	heat transfer rate
$R$	vector space

R	viscous Jacobian defined in (3-37) or the gas constant
R(U)	nonlinear operator resulting from spatial discretization
Re <sub>∞,r</sub>	characteristic Reynolds number, $\rho_\infty  V _\infty r / \mu_\infty$
r	radial coordinate, measured from the vertex of the shapes
r <sub>i</sub>	i-th component of R(U)
S	vector projection defined in (3-81)
S	solution vector in (3-82) or viscous Jacobian defined in (3-37)
S <sub>θ</sub> , S <sub>φ</sub>	matrices defined in (B-2) and (B-4)
St	Stanton number, $ q_w  / \rho_\infty  V _\infty c_p (T_a - T_w)$
T	temperature
t	time
U	conservative vector
u <sub>x</sub> , u <sub>y</sub> , u <sub>z</sub>	velocity components in Cartesian coordinates
u <sub>r</sub> , u <sub>θ</sub> , u <sub>φ</sub>	velocity components in spherical coordinates
V	total velocity vector
x	Cartesian coordinate
y	Cartesian coordinate
z	Cartesian coordinate
α	angle of attack or $\frac{1}{2}  V ^2$
β	$\gamma - 1$
γ	ratio of specific heats
Δ, δ	increment
Δ <sub>+</sub> , Δ <sub>-</sub>	forward and backward finite differencing operator, respectively
θ	spherical coordinate, conical angle
Λ	delta wing leading edge sweep angle
Λ <sub>A</sub> , Λ <sub>B</sub>	diagonal matrices defined in (3-2), (3-3)
μ	viscosity
ρ	density

$\tau_{ij}$  stress tensor  
 $\varphi$  spherical coordinate, circumferential angle, measured from  
windward symmetry surface

#### Subscripts

a adiabatic value  
c cone surface  
i,j value at  $(r, \theta_i, \varphi_j)$   
r coordinate component  
t derivative with respect to time  
w wall value  
x,y,z coordinate components  
o stagnation value  
 $\infty$  free-stream value  
 $\theta, \varphi$  coordinate components or derivative to  $\theta, \varphi$ , respectively

#### Superscripts

n time level  
T transpose

## CHAPTER ONE

### INTRODUCTION

#### 1.1 Hypersonic Interest and Projected Spacecraft

During the past few years a strong international interest has been renewed in all aspects of hypersonic flight, driven by new spacecraft concepts such as the British HOTOL (HORIZONTAL Take-Off and Landing), the French Hermes, the West German Sanger and the American NASP (National Aero-Space Plane) [1,2]. These hypersonic flight vehicles are primarily planned to operate as more economic space satellite launch vehicles to satisfy the increasing demand for development of space for communications, scientific experiments and material manufacture. Among them the HOTOL and the NASP are aimed at a historical goal for launch vehicles, i.e. full reusability. This HOTOL-class spacecraft reduces drastically the cost of present day launchers, i.e. the rocket system or the US space shuttle, mainly by taking advantage of a horizontal take-off from a conventional runway and by economies achieved through air-breathing in the lower level of the atmosphere. Furthermore, due to their airplane-like operation within the atmosphere, the design of HOTOL-class spacecraft is directly relevant to a new generation of sub-orbital hypersonic transport vehicle for fast and economic trans-global operation.

For the design of such hypersonic vehicles, in addition to the importance of the prediction of aerodynamic forces due to their airplane-like operation, one of the most demanding factors is the prediction of the aerodynamic heating rate. As pointed out in [3, 4], high heating is not only limited to the stagnation line on the windward surface. Flow interactions can introduce locally very high heating rates. Accurate knowledge of skin temperature and heating rate is essential in deciding what materials are used to build the structure and what insulation is required.

## 1.2 Classification and Modelling of Hypersonic Flow

The term *hypersonic flow* usually refers to flows with Mach number  $M > 6$ . A major complexity associated with hypersonic aerodynamics is that the hypersonic regime covers the whole flow range from the continuum flow to molecular flow. Hypersonic flow can be classified according to the value of the ratio of the mean free path of the molecules and the characteristic length of the considered problem, denoted by the Knudsen number,  $Kn$ . In the continuum flow range at very small  $Kn$ , i.e.  $Kn < 0.1$ , the Navier–Stokes equations can generally be used to describe the flow processes. This is true for atmospheric flight in altitudes up to around 100 km. In the other limiting case, at very large  $Kn$ , the mean free path of the molecules becomes of sufficient magnitude relative to the vehicle dimensions that the continuum model breaks down and the full Boltzmann equation must be used. Here molecular flow simulations should be employed, wherein the motion of a large number of molecules is computed, such as in the direct simulation Monte–Carlo method.

Because of the wide range of the hypersonic regime, in addition to the well–known difficulties in compressible flows associated with the determination of transition from laminar flow to turbulence and the modelling of turbulence, hypersonic flows often involve such new problems as real gas effects, equilibrium or non–equilibrium chemical reactions and the flow behaviour in the transitional range between continuum and molecular ranges.

In the hypersonic regime a major design driver is the prediction of peak aerodynamic forces and peak aerodynamic heating rates, which usually occur at lower altitudes within the continuum range. However hypersonic flows around flight vehicle in this flow range often involve strong flow interactions such as shock–shock, shock–boundary layer, shock–vortex and other viscous/inviscid interactions.

Solutions of Euler equations or even simpler inviscid modelling can sometimes

provide useful data on aerodynamic forces and can be coupled with proper boundary layer codes to generate such important parameters as skin friction and heat transfer rates. However this approach is not applicable when strong viscous/inviscid interaction occurs. The boundary layer approximation is no longer valid in such regions as on the lee-side of the vehicle at high angles of attack, near the nose of the body and around the leading edge of the wing at high Mach number. Therefore, for strong interactive flows, a Navier-Stokes solution is required to predict accurately hypersonic aerodynamic characteristics.

### 1.3 Wind Tunnel Experimentation and Hypersonic CFD

With the continuous development of more powerful computers as well as more sophisticated and efficient numerical algorithms, computational fluid dynamics(CFD) has emerged as a viable tool in understanding complicated fluid dynamic phenomena in subsonic, transonic and supersonic regimes. CFD is now routinely applied to practical problems, in complementary ways, with wind tunnel experimentation in the aircraft design and verification process.

Although CFD is playing an increasingly important role, wind tunnel experimentation has been the major design tool for modern aircraft. It is also well-known that the development of the US Space Shuttle took place mainly in wind tunnels or by other means of experimental investigation.

Unfortunately, difficulties with wind tunnel experimentation in the hypersonic regime become much more severe than in the lower flow speed regimes. For the flow conditions which existing hypersonic wind tunnels can achieve, high energy consumption makes this approach very expensive. On the other hand, the accuracy of such crucial parameters as the heat transfer rate, is difficult to achieve by conventional measurement techniques due to the usually small dimension of the hypersonic wind tunnels, which limits the size of the models to be tested. Furthermore, experimental simulation of a hypersonic flow field in which non-equilibrium reaction chemistry is important would require the air density, flight velocity and vehicle scale all to be reproduced simultaneously. This is not possible in existing ground-based experimental facilities. A typical example is the situation with the US space shuttle programme. The experience gained in free flight as compared to experimental and theoretical design shows that many flow phenomena lack basic understanding and require further study. Examples include the severe heating rate found on the leeside surface of the Shuttle.

In contrast, CFD capabilities can be extended to the hypersonic regime more easily without the fundamental difficulties apparent in hypersonic experimental investigation. The simulation of the density, velocity and scale is possible in computer flow simulation. The renewed interests in hypersonic flight is in fact partly attributed to the confidence in using CFD solely in design because of the impossibility of simulating the wide range of the actual hypersonic conditions in a wind tunnel. As a result, CFD is anticipated to be the primary tool, or the only tool in some conditions, for providing the extensive flow simulation information required in the design process of new hypersonic vehicles. The hypersonic flow regime will probably be the first to be dominated by CFD. This of course necessitates the development of efficient and robust hypersonic CFD codes which are reliable in predicting important quantities such as aerodynamic loading and heating.

Although today's numerical algorithms are more accurate, efficient and robust than those of a few years ago, they are still unsatisfactory in many aspects. Worthwhile codes have been produced, but further improvements in algorithm technology could multiply their usefulness many times over. Major improvements are needed in spatial accuracy, convergence reliability and convergence rates [5, 6]. CFD methods today can simulate flow about complex geometries with simple physics, or about simple geometries with more complex physics, but they cannot do both. To change this situation, one of the most pressing needs today is the improvement of the convergence rate in Euler and Navier—Stokes solutions. This need is more severe in hypersonic CFD because the complexity of the flow usually involves solution of high order equations.

A wind tunnel must be calibrated after it is built. A numerical code needs to be validated to ascertain its accuracy before or during the computer simulation of the flow. This validation can usually be done by running the code under conditions where well—documented experimental data are available and comparing the numerical results with the experimental data. It should be noted that the existing experimental data in hypersonic regime are rare and the quality of these data are usually low as compared

with the extensive and well-documented data in subsonic, transonic and supersonic regimes. This is clearly attributed to the difficulties with hypersonic experimentations as mentioned earlier. Expensive free-flight tests would be the only way to validate numerical codes in the full hypersonic regime.

#### 1.4 Aim and Approaches of This Study

This practical requirement inspired the present research to simulate continuous hypersonic flow by solving the Navier–Stokes equations in order to provide extensive flow field data for both the basic understanding of complex flows and for actual design purposes.

As a first stage towards this ultimate goal the present study assumed that the gas is perfect. Therefore validation of the codes could be carried out by comparing the numerical results with existing experimental data. Confidence in using the codes, together with the ability of Navier–Stokes CFD to assess real gas effects not generally simulated in experimental facilities, will naturally lead to the exploration of the real gas effects on such parameters as lift–drag ratio, stability and aerodynamic heating.

Laminar flows were investigated in this study because of the lack of reliable determination of transition and turbulence modelling for 3D hypersonic strongly interactive flow and also due to the prevalence of laminar flow in the hypersonic regime.

The final assumption concerns the geometry. Conical shapes were chosen in this study. The reason for this is twofold. First of all they include fundamental or generic shapes that can represent spacecraft geometries. Important examples of such shapes are (1) cones, (2) elliptic cones, (3) delta wings, (4) conical body/delta wing combinations, (5) axial corners, (6) caret wings and other wave riders. Secondly a locally conical approximation can be made for hypersonic flow around such shapes downstream of the apex, which decouples the 3D NS equations in the radial direction. Therefore computation and storage requirements are reduced radically so that a systematic investigation on both the numerical methods and the physical phenomena could be carried out with a medium–sized computer, namely, the ICL 2988 of Glasgow University Computing Centre, which was available during this study.

To sum up, the assumptions made in the research reported in this thesis are:

- (a) the flow is a continuum;
- (b) the gas is perfect;
- (c) the flow is laminar;
- (d) the geometry is conical.

Under these assumptions, a mathematical model – the locally conical Navier–Stokes equations(LCNSE) – can be established for the simulation of the flow.

The presentation is naturally divided into two major steps: (1) numerical aspects; (2) physical aspects, which were in fact closely related to each other in the development of the research.

On the numerical aspects, for an efficient simulation, emphasis was put on the improvement of the convergence rate, which is considered to be one of the most pressing needs in hypersonic CFD with N–S solutions. To achieve fast convergence to the steady state, two implicit time marching schemes were developed to solve the locally conical N–S equations. These two schemes are based on (1) the MacCormack implicit scheme [7]; (2) the Beam–Warming implicit scheme [8]. Major new inputs into the application of these two implicit schemes to the LCNSE are: (1) in the MacCormack implicit scheme an implicit boundary condition treatment according to the explicit boundary condition was adopted; (2) an explicit treatment of the source term in the LCNSE was employed and justified; (3) a simplified version of Beam–Warming implicit scheme was proposed for steady state solution; (4) steady state dependence on time step of MacCormack–type schemes was revealed and the measures to avoid it was investigated; (5) accuracy and efficiency of these two schemes were compared and discussed.

To further accelerate the convergence, two multigrid methods were presented for these two implicit schemes respectively. This original work was motivated by the recent

progress in multigrid theories [9] and some successful applications of the multigrid procedures to accelerate explicit time marching schemes in CFD [10–12]. The Ni-type multigrid procedure [10] was applied to accelerate the MacCormack implicit scheme [13] while the full approximation scheme(FAS) [14, 15] was used to speed up the convergence of the simplified Beam–Warming implicit scheme. This was done according to the basic structures of the two different implicit schemes. Different strategies in the multigrid procedures were studied.

In parallel to this, a more basic numerical investigation was carried out on a sparse quasi–Newton method [16–22] for a fast steady state solution. This was a result of an analysis on the inherent shortcomings of the existing implicit schemes for steady state solutions. A general procedure of the method was proposed and formulation was demonstrated for three and five point spatial discretization schemes. Preliminary results were obtained for a nozzle problem modelled by 1D Euler equations with high shock–resolution schemes, i.e. van Leer's flux vector splitting scheme [23, 24] and Harten's total variation diminishing(TVD) scheme [25, 26]. Compared with the corresponding implicit operators, the sparse quasi–Newton approach showed a much faster convergence to steady state.

This thesis presents numerical flow field simulations for three simple while representative geometries of hypersonic flight interest. Cones, delta wings and cone–and–delta–wing combinations were studied. Comparisons are made with the experimental data of Tracy [27], Cross [28] and Meyer and Vail [29] respectively. The flows around cones and delta wings in low speed regimes were well understood. But their behaviour in hypersonic regime needs to be further investigated. The present codes provided this possibility. Unlike the situation with cones and delta wings, the hypersonic flow around a cone–and–delta–wing combination is more complicated due to the more complex flow interactions. The only information available about this flow was some surface measurement data [29–31]. The flowfield data did not exist and the surface measurements near the junction was not certain. A first flowfield simulation of

such flow by the codes developed in the present research [32] provided further insight into the complex structure of the flow and revealed high local aerodynamic heating regions and their causes. The leeward flow above the combination was also explored with the present computer simulation [33].

## 1.5 Arrangement of the Thesis

As mentioned in the previous sections, the major contribution can naturally be divided into (1) numerical method development; (2) hypersonic flow simulations. As a consequence, after the mathematical model is established in Chap. 2, the thesis develops in the two following chapters on these two aspects respectively. Chap. 3 presents research efforts towards faster convergence after detailed presentation of the basic numerical schemes. Accuracy studies will also be reported in this chapter. In Chap. 4, some simulations are presented. Interesting physical phenomena revealed by the simulation will be discussed. General conclusions drawn from this study and future work are addressed in Chap. 5.

## CHAPTER TWO

### GOVERNING EQUATIONS

#### 2.1 Introduction

In this chapter, the governing equations are described under the assumptions mentioned in Chap. 1. As a starting point, the unsteady three dimensional compressible N-S equations in Cartesian coordinates are presented in Sec. 2.2. They are then transformed into spherical coordinates in Sec. 2.3. In Sec. 2.4 the locally conical approximation is introduced to the N-S equations in spherical coordinates and the locally conical N-S equations result. Conical Euler equations are derived in Sec. 2.5 by simply deleting viscous terms in the locally conical N-S equations. Sec. 2.6 describes the initial and boundary conditions.

## 2.2 Compressible N-S Equations in Cartesian Coordinates

The unsteady, three dimensional, compressible Navier-Stokes equations in Cartesian coordinates  $(x,y,z)$  without body forces and external heat addition can be written in conservation form as

$$\frac{\partial U}{\partial t} + \frac{\partial E}{\partial x} + \frac{\partial F}{\partial y} + \frac{\partial G}{\partial z} = 0 \quad (2-1)$$

where the dependent variable vector  $U$  is given by

$$U = \begin{bmatrix} \rho \\ \rho u_x \\ \rho u_y \\ \rho u_z \\ \rho e \end{bmatrix} \quad (2-2)$$

and the flux vectors  $E, F, G$  are given by

$$E = \begin{bmatrix} \rho u_x \\ \rho u_x^2 + p - \tau_{xx} \\ \rho u_y u_x - \tau_{yx} \\ \rho u_z u_x - \tau_{zx} \\ (\rho e + p)u_x + q_x - u_x \tau_{xx} - u_y \tau_{yx} - u_z \tau_{zx} \end{bmatrix} \quad (2-3)$$

$$F = \begin{bmatrix} \rho u_y \\ \rho u_x u_y - \tau_{xy} \\ \rho u_y^2 + p - \tau_{yy} \\ \rho u_z u_y - \tau_{zy} \\ (\rho e + p)u_y + q_y - u_x \tau_{xy} - u_y \tau_{yy} - u_z \tau_{zy} \end{bmatrix} \quad (2-4)$$

$$G = \begin{bmatrix} \rho u_z \\ \rho u_x u_z - \tau_{xz} \\ \rho u_y u_z - \tau_{yz} \\ \rho u_z^2 + p - \tau_{zz} \\ (\rho e + p)u_z + q_z - u_x \tau_{xz} - u_y \tau_{yz} - u_z \tau_{zz} \end{bmatrix} \quad (2-5)$$

and the components of the stress tensor are

$$\begin{aligned}
 \tau_{xx} &= \frac{2}{3} \mu \left( 2 \frac{\partial u_x}{\partial x} - \frac{\partial u_y}{\partial y} - \frac{\partial u_z}{\partial z} \right) \\
 \tau_{yy} &= \frac{2}{3} \mu \left( 2 \frac{\partial u_y}{\partial y} - \frac{\partial u_x}{\partial x} - \frac{\partial u_z}{\partial z} \right) \\
 \tau_{zz} &= \frac{2}{3} \mu \left( 2 \frac{\partial u_z}{\partial z} - \frac{\partial u_x}{\partial x} - \frac{\partial u_y}{\partial y} \right) \\
 \tau_{xy} &= \mu \left( \frac{\partial u_x}{\partial y} + \frac{\partial u_y}{\partial x} \right) = \tau_{yx} \\
 \tau_{xz} &= \mu \left( \frac{\partial u_x}{\partial z} + \frac{\partial u_z}{\partial x} \right) = \tau_{zx} \\
 \tau_{yz} &= \mu \left( \frac{\partial u_y}{\partial z} + \frac{\partial u_z}{\partial y} \right) = \tau_{zy}
 \end{aligned} \tag{2-6}$$

Fourier's law for heat transfer by conduction will be assumed so that the components of the heat flux  $q$  can be expressed as

$$\begin{aligned}
 q_x &= -k \frac{\partial T}{\partial x} \\
 q_y &= -k \frac{\partial T}{\partial y} \\
 q_z &= -k \frac{\partial T}{\partial z}
 \end{aligned} \tag{2-7}$$

Because a perfect gas is assumed, the equations of states are

$$p = \rho RT \tag{2-8}$$

$$T = (\gamma - 1) [ e - |V|^2/2 ] / R \tag{2-9}$$

where  $R = 287 \text{ m}^2/\text{sec}^2 \cdot \text{K}$  is the gas constant and  $\gamma = 1.4$  is the ratio of specific heats.

The coefficient of viscosity is given by the Sutherland's formula

$$\mu = C_1 \frac{T^{3/2}}{T + C_2} \tag{2-10}$$

where  $C_1$  and  $C_2$  are constants given as  $1.458 \times 10^{-6} \text{ kg/m} \cdot \text{sec} \cdot \text{K}^{1/2}$  and  $110.4 \text{ K}$  respectively.

The coefficient of thermal conductivity is related to the coefficient of viscosity by the Prandtl number

$$\text{Pr} = \frac{c_p \mu}{k} \quad (2-11)$$

So far nine equations in Eqs. (2-1), (2-8)–(2-11) are obtained for nine unknowns, the density  $\rho$ , the three velocity components  $u_x$ ,  $u_y$ ,  $u_z$ , the internal energy  $e$ , the pressure  $p$ , the temperature  $T$ , the coefficient of viscosity  $\mu$  and the coefficient of thermal conductivity  $k$ . The description of the problem will be completed with the specification of appropriate initial and boundary conditions, which will be discussed later.

As pointed out by Peyret and Viviand [34], the system of the above N–S equations is of hybrid parabolic and hyperbolic type. Without the time dependent term in Eq. (2-1) the steady N–S equation system is of hybrid elliptic and hyperbolic type.

With grid generation techniques, a general transformation can be made for general body–fitted coordinates. In spite of this, a specific transformation is introduced in the next section which suits conical shapes.

### 2.3 Compressible N-S Equations in Spherical Coordinates

For the study of the flow around conical shapes, it was found that a spherical coordinate system is much easier for a simple body-fitted mesh generation. For these shapes, therefore, it is not necessary to use a general grid generation technique. Such a technique usually involves solutions of partial differential equations for a body-fitted coordinate system.

Eq. (2-1) can be transformed into the spherical coordinate system  $(r, \theta, \varphi)$  via the following transformation

$$\begin{aligned} x &= x(r, \theta, \varphi) = r \sin\theta \cos\varphi, & r &> 0 \\ y &= y(r, \theta, \varphi) = r \sin\theta \sin\varphi, & 0 &\leq \theta \leq \pi \\ z &= z(r, \theta, \varphi) = r \cos\theta, & 0 &\leq \varphi \leq 2\pi \end{aligned} \quad (2-12)$$

Fig. 2.1 shows the relation between the two coordinate system.

The resulting equations in a spherical coordinate system can be written in weak conservation form as

$$\frac{\partial \bar{U}}{\partial t} + \frac{\partial \bar{E}}{\partial r} + \frac{\partial \bar{F}}{\partial \theta} + \frac{\partial \bar{G}}{\partial \varphi} + \bar{H} = 0 \quad (2-13)$$

where

$$\bar{U} = r^2 \sin\theta \begin{bmatrix} \rho \\ \rho u_r \\ \rho u_\theta \\ \rho u_\varphi \\ \rho e \end{bmatrix} \quad (2-14)$$

$$\bar{E} = r^2 \sin\theta \begin{bmatrix} \rho u_r \\ \rho u_r^2 + p - \tau_{rr} \\ \rho u_\theta u_r - \tau_{\theta r} \\ \rho u_\varphi u_r - \tau_{\varphi r} \\ (\rho e + p)u_r + q_r - u_r \tau_{rr} - u_\theta \tau_{\theta r} - u_\varphi \tau_{\varphi r} \end{bmatrix} \quad (2-15)$$

$$\bar{F} = r \sin\theta \begin{bmatrix} \rho u_\theta \\ \rho u_r u_\theta - \tau_{r\theta} \\ \rho u_\theta^2 + p - \tau_{\theta\theta} \\ \rho u_\varphi u_\theta - \tau_{\varphi\theta} \\ (\rho e + p)u_\theta + q_\theta - u_r \tau_{r\theta} - u_\theta \tau_{\theta\theta} - u_\varphi \tau_{\varphi\theta} \end{bmatrix} \quad (2-16)$$

$$\bar{G} = r \begin{bmatrix} \rho u_\varphi \\ \rho u_r u_\varphi - \tau_{r\varphi} \\ \rho u_\theta u_\varphi - \tau_{\theta\varphi} \\ \rho u_\varphi^2 + p - \tau_{\varphi\varphi} \\ (\rho e + p)u_\varphi + q_\varphi - u_r \tau_{r\varphi} - u_\theta \tau_{\theta\varphi} - u_\varphi \tau_{\varphi\varphi} \end{bmatrix} \quad (2-17)$$

and the source term vector is

$$\bar{H} = r \sin\theta \begin{bmatrix} 0 \\ -(\rho u_\theta^2 + p - \tau_{\theta\theta}) - (\rho u_\varphi^2 + p - \tau_{\varphi\varphi}) \\ -\text{ctg}\theta (\rho u_\varphi^2 + p - \tau_{\varphi\varphi}) + \rho u_r u_\theta - \tau_{r\theta} \\ \text{ctg}\theta (\rho u_\theta u_\varphi - \tau_{\theta\varphi}) + \rho u_r u_\theta - \tau_{r\varphi} \\ 0 \end{bmatrix} \quad (2-18)$$

The components for the shear stress tensor are

$$\begin{aligned} \tau_{rr} &= 2\mu \frac{\partial u_r}{\partial r} - \frac{2}{3}\mu \text{div } V \\ \tau_{\theta\theta} &= 2\mu \left( \frac{1}{r} \frac{\partial u_\theta}{\partial \theta} + \frac{u_r}{r} \right) - \frac{2}{3}\mu \text{div } V \\ \tau_{\varphi\varphi} &= 2\mu \left( \frac{1}{r \sin\theta} \frac{\partial u_\varphi}{\partial \varphi} + \frac{u_r}{r} + \frac{u_\theta \text{ctg}\theta}{r} \right) - \frac{2}{3}\mu \text{div } V \\ \tau_{r\theta} &= \tau_{\theta r} = \mu \left[ r \frac{\partial}{\partial r} \left( \frac{u_\theta}{r} \right) + \frac{1}{r} \frac{\partial u_r}{\partial \theta} \right] \\ \tau_{\theta\varphi} &= \tau_{\varphi\theta} = \mu \left[ \frac{\sin\theta}{r} \frac{\partial}{\partial \theta} \left( \frac{u_\varphi}{\sin\theta} \right) + \frac{1}{r \sin\theta} \frac{\partial u_\theta}{\partial \varphi} \right] \\ \tau_{r\varphi} &= \tau_{\varphi r} = \mu \left[ \frac{1}{r \sin\theta} \frac{\partial u_r}{\partial \varphi} + r \frac{\partial}{\partial r} \left( \frac{u_\varphi}{r} \right) \right] \\ \text{div } V &= \frac{1}{r^2 \sin\theta} \left[ \frac{\partial}{\partial r} (r^2 \sin\theta u_r) + \frac{\partial}{\partial \theta} (r \sin\theta u_\theta) + \frac{\partial}{\partial \varphi} (r u_\varphi) \right] \end{aligned} \quad (2-19)$$

and the components of the heat flux are

$$\begin{aligned} q_r &= -k \frac{\partial T}{\partial r} \\ q_\theta &= -k \frac{1}{r} \frac{\partial T}{\partial \theta} \\ q_\varphi &= -k \frac{1}{r \sin\theta} \frac{\partial T}{\partial \varphi} \end{aligned} \quad (2-20)$$

In spherical coordinates, conical shapes are usually easily defined. Especially interesting is that the spherical coordinate surfaces compose a variety of practical conical shapes without further transformation. These shapes include cones (Fig. 2.2), delta wings (Fig. 2.3), cone/delta wing combinations with or without the wing dihedral (Fig. 2.4), and some waveriders such as caret wings (Fig. 2.5). As shown in the figures a cone with a half-cone angle  $\theta_c$  is composed of a  $\theta = \theta_c$  ( $0 \leq \varphi \leq 2\pi$ ) coordinate surface. A delta wing with leading edge sweep back angle  $\Lambda$  is composed of  $\theta = \pi/2$  ( $-\pi/2 + \Lambda \leq \varphi \leq \pi/2 - \Lambda$ ). A cone/delta wing combination is composed of  $\theta = \theta_c$  ( $0 \leq \varphi \leq 2\pi$ ),  $\varphi = \pi/2$  ( $\theta_c \leq \theta \leq \pi/2 - \Lambda$ ) and  $\varphi = -\pi/2$  ( $\theta_c \leq \theta \leq \pi/2 - \Lambda$ ).

## 2.4 Locally Conical Navier–Stokes Equations (LCNSE)

Numerical solution of the 3D N–S equations described in Sec. 2.2 or 2.3 requires both a huge computer storage and a very large amount of computing time even for simple aerodynamic configurations. This has led researchers in the past to simplify the equations through neglect of the stress terms ( therefore, inviscid flow) and/or by reduction of the number of dimensions to be considered in the problem. This section introduces the local conicity concept after description of the global conical flow. The locally conical approximation decouples the 3D N–S equations in the radial direction and leads to the locally conical N–S equations.

### 2.4.1 Definition of Conical Flow

Generally speaking, a *conical flow* can be defined as a flow in which all flow quantities are constant along rays passing through a common vertex. If a conical shape is defined as a shape generated by rays passing through a common vertex, a truly conical flow can only be an inviscid supersonic or hypersonic flow around a conical shape with a bow shock wave attached to the vertex of the shape. The exclusion of a significant length scale has the effect of reducing the number of independent variables in the problem by one.

If a body–fitted spherical coordinate system centred at the vertex of the conical shape is used to describe the flow, then all the spherical surfaces must have the same vector and scalar values of the flow quantities for a given  $(\theta, \varphi)$  point. Therefore all the derivatives of the flow quantities with respect to the spherical radius ( $r$ ) of these spherical surfaces from the origin must be zero.

### 2.4.2 Locally Conical Approximation

As noted in Sec. 2.4.1, the concept of conical flow is strictly valid only for inviscid flow. Conicity disappears when viscosity is involved. However examination of many experimental studies [27–31] of supersonic or hypersonic flows around conical shapes revealed that these flows exhibit a locally conical behaviour downstream from the nose region even though relatively large viscous regions exist. If the flow is described in a spherical coordinate system, this locally conical behaviour indicates that, for a given  $r$ , the gradient in the radial direction is much smaller than those in the crossflow spherical surface.

Based on this examination, MacRae [35] introduced an approximation to the 3D N–S equations for supersonic or hypersonic flows around cones. Unlike MacRae's presentation a local point of view is stressed here in this approximation to avoid confusion with the global inviscid conical flow.

For a given spherical surface, i.e., a given  $r$ , a locally conical approximation is done by neglecting the derivatives of the flow quantities  $\rho$ ,  $u_r$ ,  $u_\theta$ ,  $u_\varphi$ ,  $e$ ,  $p$ ,  $T$ ,  $\mu$  and  $k$  with respect to  $r$  in the 3D N–S equations (2–13).

### 2.4.3 Derivation of Locally Conical Navier–Stokes Equations

Under the locally conical approximation, the changes made in the expressions (2–19) for the shear stress tensor are

$$\begin{aligned}\tau_{rr} &= -\frac{2}{3}\mu \operatorname{div} \mathbf{V} \\ \tau_{r\theta} = \tau_{\theta r} &= \frac{\mu}{r} \left( -u_\theta + \frac{\partial u_r}{\partial \theta} \right) \\ \tau_{r\varphi} = \tau_{\varphi r} &= \frac{\mu}{r} \left( \frac{1}{\sin\theta} \frac{\partial u_r}{\partial \varphi} - u_\varphi \right)\end{aligned}\tag{2-21}$$

$$\begin{aligned} \operatorname{div} V &= \frac{1}{r \sin \theta} \left( 2u_r \sin \theta + \frac{\partial}{\partial \theta} (u_r \sin \theta) + \frac{\partial u_\theta}{\partial \varphi} \right) \\ q_r &= 0 \end{aligned} \quad (2-22)$$

Therefore from the expressions in (2-15) and (2-21) the derivative of the r direction flux vector with respect to r becomes

$$\begin{aligned} \frac{\partial \bar{E}}{\partial r} &= \frac{2}{r} \bar{E} - r^2 \sin \theta \frac{\partial}{\partial r} \begin{bmatrix} 0 \\ \tau_{rr} \\ \tau_{\theta r} \\ \tau_{\varphi r} \\ u_r \tau_{rr} + u_\theta \tau_{\theta r} + u_\varphi \tau_{\varphi r} \end{bmatrix} \\ &= \frac{2}{r} \bar{E} + r \sin \theta \begin{bmatrix} 0 \\ \tau_{rr} \\ \tau_{\theta r} \\ \tau_{\varphi r} \\ u_r \tau_{rr} + u_\theta \tau_{\theta r} + u_\varphi \tau_{\varphi r} \end{bmatrix} \end{aligned} \quad (2-23)$$

By substituting expression (2-23) into Eq.(2-13), the equations become

$$\frac{\partial \bar{U}}{\partial t} + \frac{\partial \bar{F}}{\partial \theta} + \frac{\partial \bar{G}}{\partial \varphi} + \bar{H}' = 0 \quad (2-24)$$

where

$$\begin{aligned} \bar{H}' &= \bar{H} + \frac{2}{r} \bar{E} + r \sin \theta \begin{bmatrix} 0 \\ \tau_{rr} \\ \tau_{\theta r} \\ \tau_{\varphi r} \\ u_r \tau_{rr} + u_\theta \tau_{\theta r} + u_\varphi \tau_{\varphi r} \end{bmatrix} \\ &= r \sin \theta \begin{bmatrix} 2\rho u_r \\ 2\rho u_r^2 - \rho u_\theta^2 - \rho u_\varphi^2 - \tau_{rr} + \tau_{\theta\theta} + \tau_{\varphi\varphi} \\ 3\rho u_r u_\theta - \operatorname{ctg} \theta (\rho u_\varphi^2 + p) + \operatorname{ctg} \theta \tau_{\varphi\varphi} - 2\tau_{r\theta} \\ 3\rho u_r u_\varphi + \operatorname{ctg} \theta \rho u_\theta u_\varphi - \operatorname{ctg} \theta \tau_{\theta\varphi} - 2\tau_{r\varphi} \\ 2u_r (\rho e + p) - u_r \tau_{rr} - u_\theta \tau_{r\theta} - u_\varphi \tau_{r\varphi} \end{bmatrix} \end{aligned} \quad (2-25)$$

#### 2.4.4 Non-dimensionalisation of LCNSE

The locally conical N-S equations are nondimensionalised by

$$\begin{aligned}
 u_r^* &= \frac{u_r}{|V|_\infty} & u_\theta^* &= \frac{u_\theta}{|V|_\infty} & u_\varphi^* &= \frac{u_\varphi}{|V|_\infty} \\
 \rho^* &= \frac{\rho}{\rho_\infty} & p^* &= \frac{p}{\rho_\infty |V|_\infty^2} & \mu^* &= \frac{\mu}{\mu_\infty} \\
 e^* &= \frac{e}{|V|_\infty^2} & T^* &= \frac{T}{T_0 - T_\infty} & t^* &= \frac{t}{r/|V|_\infty}
 \end{aligned} \tag{2-26}$$

where the nondimensionalised variables are denoted by an asterisk. The free stream conditions, denoted by  $\infty$ , are used for the non-dimensionalisation and  $r$  is the location of the spherical surface where the locally conical approximation is made.

As a result, the nondimensionalised LCNSE can be written as

$$\frac{\partial U}{\partial t} + \frac{\partial F}{\partial \theta} + \frac{\partial G}{\partial \varphi} + H = 0 \tag{2-27}$$

where

$$U = \sin\theta \begin{bmatrix} \rho \\ \rho u_r \\ \rho u_\theta \\ \rho u_\varphi \\ \rho e \end{bmatrix} \tag{2-28}$$

$$F = \sin\theta \begin{bmatrix} \rho u_\theta \\ \rho u_r u_\theta - \tau_{r\theta} \\ \rho u_\theta^2 + p - \tau_{\theta\theta} \\ \rho u_\varphi u_\theta - \tau_{\varphi\theta} \\ (\rho e + p)u_\theta + q_\theta - u_r \tau_{r\theta} - u_\theta \tau_{\theta\theta} - u_\varphi \tau_{\varphi\theta} \end{bmatrix} \tag{2-29}$$

$$G = \begin{bmatrix} \rho u_\varphi \\ \rho u_r u_\varphi - \tau_{r\varphi} \\ \rho u_\theta u_\varphi - \tau_{\theta\varphi} \\ \rho u_\varphi^2 + p - \tau_{\varphi\varphi} \\ (\rho e + p)u_\varphi + q_\varphi - u_r \tau_{r\varphi} - u_\theta \tau_{\theta\varphi} - u_\varphi \tau_{\varphi\varphi} \end{bmatrix} \tag{2-30}$$

$$H = \sin\theta \begin{bmatrix} 2\rho u_r \\ 2\rho u_r^2 - \rho u_\theta^2 - \rho u_\varphi^2 - \tau_{rr} + \tau_{\theta\theta} + \tau_{\varphi\varphi} \\ 3\rho u_r u_\theta - \text{ctg}\theta(\rho u_\varphi^2 + p) + \text{ctg}\theta \tau_{\varphi\varphi} - 2\tau_{r\theta} \\ 3\rho u_r u_\varphi + \text{ctg}\theta \rho u_\theta u_\varphi - \text{ctg}\theta \tau_{\theta\varphi} - 2\tau_{r\varphi} \\ 2u_r(\rho e + p) - u_r \tau_{rr} - u_\theta \tau_{r\theta} - u_\varphi \tau_{r\varphi} \end{bmatrix} \quad (2-31)$$

where the components of the shear stress tensor are

$$\begin{aligned} \tau_{rr} &= -\frac{2}{3} \frac{\mu}{\text{Re}_{\infty,r}} \left( 2u_r + \frac{\partial u_\theta}{\partial \theta} + \text{ctg}\theta u_\theta + \frac{1}{\sin\theta} \frac{\partial u_\varphi}{\partial \varphi} \right) \\ \tau_{\theta\theta} &= \frac{2\mu}{\text{Re}_{\infty,r}} \left( \frac{\partial u_\theta}{\partial \theta} + u_r \right) + \tau_{rr} \\ \tau_{\varphi\varphi} &= \frac{2\mu}{\text{Re}_{\infty,r}} \left( \frac{1}{\sin\theta} \frac{\partial u_\varphi}{\partial \varphi} + u_r + u_\theta \text{ctg}\theta \right) + \tau_{rr} \\ \tau_{r\theta} = \tau_{\theta r} &= \frac{\mu}{\text{Re}_{\infty,r}} \left( -u_\theta + \frac{\partial u_r}{\partial \theta} \right) \\ \tau_{\theta\varphi} = \tau_{\varphi\theta} &= \frac{\mu}{\text{Re}_{\infty,r}} \left( \frac{\partial u_\varphi}{\partial \theta} - \text{ctg}\theta u_\varphi + \frac{1}{\sin\theta} \frac{\partial u_\theta}{\partial \varphi} \right) \\ \tau_{r\varphi} = \tau_{\varphi r} &= \frac{\mu}{\text{Re}_{\infty,r}} \left( \frac{1}{\sin\theta} \frac{\partial u_r}{\partial \varphi} - u_\varphi \right) \end{aligned} \quad (2-32)$$

and the components of the heat flux in (2-29) and (2-30) are given by

$$\begin{aligned} q_\theta &= -\frac{\mu}{2\text{Re}_{\infty,r}\text{Pr}} \frac{\partial T}{\partial \theta} \\ q_\varphi &= -\frac{\mu}{2\sin\theta\text{Re}_{\infty,r}\text{Pr}} \frac{\partial T}{\partial \varphi} \end{aligned} \quad (2-33)$$

With non-dimensionalisation (2-26), the equations of state, (2-8) and (2-9) become

$$p = \frac{\gamma-1}{2\gamma} \rho T \quad (2-34)$$

$$T = 2\gamma(e - |V|^2/2) \quad (2-35)$$

For simplicity of the layout of the above governing equations, which are used in the following computation, the asterisk for all the nondimensionized variables are omitted.

Note that the length scale  $r$  still appears in the governing equations through the characteristic Reynolds number

$$\text{Re}_{\infty,r} = \frac{\rho_\infty |V|_\infty r}{\mu_\infty} \quad (2-36)$$

in the expressions for shear stress (2-32) and heat flux (2-33). As a consequence, solution of the locally conical N-S equations depends directly on the position  $r$  where the computation is carried out. And it is also evident that the non-conicity, i.e. the difference in the solutions for different values of  $r$ , is totally attributed to the viscous effects.

With the help of the LCNSE (2-27), the claim that a conical flow has to be inviscid flow can be proved. Suppose the flow is conical and described by 3D N-S equations (2-13). Then  $(\partial/\partial r)$  should be zero with respect to all flow quantities. This results in the LCNSE (2-27). Because the flow is conical, the solution should be independent of  $r$ . But  $r$  appears in (2-27) through (2-32) and (2-33). Therefore the coefficient of viscosity  $\mu$  should be zero. In other words, inviscid flow is a necessary condition for conical flows. The conical boundary condition requires that a conical flow should be supersonic or hypersonic.

## 2.5 Conical Euler Equations

As discussed in the last section, conical flows are inviscid and, therefore, solutions of Euler equations. Conical Euler equations can be derived by neglecting viscous terms in the locally conical N-S equations. Therefore the conical Euler equations may be written in the following form.

$$\frac{\partial U}{\partial t} + \frac{\partial F}{\partial \theta} + \frac{\partial G}{\partial \varphi} + H = 0 \quad (2-37)$$

where

$$U = \sin\theta \begin{bmatrix} \rho \\ \rho u_r \\ \rho u_\theta \\ \rho u_\varphi \\ \rho e \end{bmatrix} \quad (2-38)$$

$$F = \sin\theta \begin{bmatrix} \rho u_\theta \\ \rho u_r u_\theta \\ \rho u_\theta^2 + p \\ \rho u_\varphi u_\theta \\ (\rho e + p) u_\theta \end{bmatrix} \quad (2-39)$$

$$G = \begin{bmatrix} \rho u_\varphi \\ \rho u_r u_\varphi \\ \rho u_\theta u_\varphi \\ \rho u_\varphi^2 + p \\ (\rho e + p) u_\varphi \end{bmatrix} \quad (2-40)$$

$$H = \sin\theta \begin{bmatrix} 2\rho u_r \\ 2\rho u_r^2 - \rho u_\theta^2 - \rho u_\varphi^2 \\ 3\rho u_r u_\theta - \text{ctg}\theta(\rho u_\varphi^2 + p) \\ 3\rho u_r u_\varphi + \text{ctg}\theta \rho u_\theta u_\varphi \\ 2u_r(\rho e + p) \end{bmatrix} \quad (2-41)$$

Examination of the above equations reveals that the significant length,  $r$ , is missing in the unsteady Euler equations.

The conical Euler solutions will be presented for comparison with the locally conical N-S solutions. Of course, they can be used to provide useful force data if the viscous/inviscid interaction is not very strong. The conical Euler code can also be used as a tool for the basic study of conical flows.

It should be noted that conical flow is only defined for steady state flow. The unsteady form is used for the steady state solution, while for the study of the initial transient phenomenon of high speed flows around conical geometries a full three dimensional unsteady solution is necessary.

## 2.6 Initial and Boundary Conditions

The description of a differential system of equations is not complete without the specification of appropriate initial and boundary conditions. This section describes the general initial and boundary conditions for the locally conical N-S equations and the conical Euler equations presented in the previous sections. The boundary conditions determine the shapes simulated. More specific conditions for different geometries will be given in detail in Chap. 4, where flow simulations are presented.

### 2.6.1 Boundary conditions

The three typical boundary conditions in the present problem are:

(a) On the wall of the conical shapes. As the flow is assumed to be continuum throughout the flowfield, no-slip condition is applied on the solid wall for viscous solutions. Either temperature or its normal derivative (corresponding to the heat transfer) is prescribed on the wall to be a given constant. That is,

$$u_r = u_\theta = u_\varphi = 0; \quad T_w \text{ or } \left(\frac{\partial T}{\partial n}\right)_w \text{ given} \quad (2-42)$$

For the inviscid solution of the Euler equations, a tangential velocity condition is applied on the wall.

(b) The outer boundary. Because shock-capturing schemes are used in the numerical solution of the governing equations, all shock waves in the flowfield are captured automatically with the numerical solutions. As a consequence of this, the flow properties on the outer boundary are set to the properties of the free stream as long as the outer boundary is sufficiently far away from the conical wall to include all the shock waves.

(c) The symmetry boundary. If the flowfield is symmetric, the computational domain can be halved by the symmetry boundary. On this boundary, all the normal derivatives of the flow properties are identically zero except for that of the normal velocity component. The normal velocity component is set to zero on the symmetry boundary. This boundary condition is commonly referred to as the *reflection condition*.

### 2.6.2 Initial Conditions

Although the major interest of this research is steady state solutions, a time marching numerical procedure is followed by solving the unsteady governing equations to achieve a steady state. In all the following computations, the flowfield is initialized to free stream values of the flow quantities at all points except for the points on the wall, where the appropriate wall boundary condition is applied.

## CHAPTER THREE

### NUMERICAL METHODS

#### 3.1 Introduction

Flows governed by the equations presented in Chap. 2 can be simulated numerically by finite-difference solution of these partial differential equations subject to appropriate initial and boundary conditions. In this chapter, methods and numerical considerations related to the finite-difference solutions of these equations will be presented. As stated in Chap. 1, one of the most pressing needs in the algorithm technology in CFD is to improve the convergence rate of Euler or N-S solutions. As steady state solutions are of major concern in this research, the emphasis will be on the achievement of fast steady state solutions.

## 3.2 Review of Existing Numerical Schemes

Before detailed presentation of the numerical approaches taken in this research, a brief review of existing schemes along with some discussion are given in the present section with concentration on steady state solutions of N-S equations. This review also justifies the approach taken in the research. More general reviews can be found in [5, 6, 34, 36]

### 3.2.1 Time Marching Approach

A time marching approach is generally followed in solving the compressible N-S equations although in many cases only a steady state is of interest. There are three reasons for this. As mentioned previously in Chap. 2, the steady compressible N-S equations are a mixed set of hyperbolic and elliptic equations which are difficult to solve because of differences in numerical techniques required for hyperbolic and elliptic equations. However, with the unsteady term, the compressible N-S equations become a set of mixed hyperbolic and parabolic equations, which can usually be solved more easily with a time marching approach due to the similarity of the numerical techniques for these two types of equations. Furthermore, following a physical time process assures robustness of the solution procedure and prevents non-physical states such as negative density, which may occur in non-physical iterative schemes to terminate the computation. Another obvious advantage of a time marching approach is the versatility of the code, which, if the time accuracy is retained in the scheme, can be used for both steady and unsteady problems. Due to these features, nearly all successful solutions of the compressible N-S equations have employed the unsteady form. The steady state solution is obtained by marching the solution in time until convergence is achieved.

On the other hand, if the physical time process is followed strictly, a time marching approach may be excruciatingly slow when one is interested solely in steady

state solutions. If one is willing to give up some versatility and interest is concentrated on the steady state problem then a faster method can be expected. Emphasis of the present research on the numerical aspect is focussed on the achievement of fast steady state solutions.

### 3.2.2 Time Discretization — Explicit or Implicit ?

If the unsteady form of the compressible N-S equations is employed, there exist essentially, as far as time discretization is concerned, two classes of methods: *explicit* or *implicit* methods.

Explicit methods such as the famous MacCormack two-step explicit method [37] have been widely used in solving compressible N-S equations since the algorithm is relatively simple. Another advantage of explicit methods appearing recently with the development of vector computers is that a full vectorization of the codes is usually straightforward. For example, Shang et al [38] vectorized the MacCormack explicit code on a Cray machine. Another more recent tendency is to use an explicit multi-stage Runge-Kutta method for Euler [39] or N-S [40] solutions. The major advantage of this approach over conventional explicit methods is that the severe stability restriction is relaxed to a certain extent due to the enlarged stability region.

As is well-known, a major difficulty with an explicit method is that the stability condition is often so restrictive that a huge number of time steps have to be taken before reaching a steady state. This situation is especially severe for N-S solutions at a high Reynolds number, where highly stretched meshes are generally involved for accurate resolution of the viscous effects. The reason behind this is that most of the explicit methods follow automatically a true physical process.

A radical development in compressible N-S solutions is the non-iterative implicit methods proposed by Briley & MacDonald [41] and Beam & Warming [8]. The *non-iterative* feature is achieved by linearization and the nonlinear problem is solved linearly at each time step. This approach is loosely referred as the implicit method in the literature and it will be used in the following text.

Recently MacCormack [7] extended his well-known explicit scheme to a implicit version. A saving in computing time by a factor of 17.5 was found compared to his former explicit scheme. It was also applied by Shang and MacCormack [42] to axisymmetric biconic configurations and computer time reduction by a factor of 13 was achieved against its fully explicit predecessor. This scheme has been applied to PNS solutions [43], viscous shock layer solutions [44] and to multiequation turbulence modelling [45].

The Beam-Warming implicit scheme and the MacCormack implicit scheme are now two of the most widely used schemes for compressible N-S solutions for the understanding of complicated flow phenomena. Generally, as compared with explicit methods the penalty that the implicit methods take more computation per time step and more coding work is amply offset by the great improvement in convergence to steady state by taking much larger time steps.

If only the steady state is of interest, the implicit time marching can be considered as a special iterative method. Because the time accuracy is not important, simplification can be introduced in the linearization of the flux vectors. In fact, exact linearization is generally impractical for N-S solutions. Hence many implicit steady state solutions of the compressible N-S equations were achieved with some kind of simplification in the linearization of the flux vectors.

Any kind of simplification in the implicit procedure can degrade convergence rate and blocks the way to accelerating the convergence further to steady state by taking

larger time steps. As a result, for an efficient time marching scheme for steady state solutions, there is a tradeoff between the simplification of the procedure, therefore, the amount of computation per time step and the convergence rate of the procedure. The two extremes are the explicit time marching, which is the simplest while usually the slowest, and the fully implicit scheme with exact linearization, which, as  $\Delta t \rightarrow \infty$ , reduces to a Newton iteration method with quadratic convergence while it is inevitably the most complicated. It is believed that the most efficient scheme should lie somewhere in between. It may be useless to produce an algorithm simple enough but with a very slow convergence rate. It is equally useless to develop a scheme with a fast convergence rate but a huge computation per iteration.

Furthermore for a practical multidimensional application, approximate factorization of the implicit operator is also introduced in the implicit time marching procedure. The error introduced by the approximate factorization is another reason in limiting time steps in implicit schemes with factorization. Recently, as the pressure on computer storage is released due to the appearance of modern supercomputers, some relaxation schemes have been proposed to avoid the factorization of the implicit operators [46–49].

### 3.2.3 Spatial Discretization — Central or Upwind ?

The above mentioned MacCormack-type schemes [37, 7], Beam-Warming implicit scheme [8] and the explicit Runge-Kutta schemes [39, 40] have all one thing in common: the use of central differencing for discretization of the spatial derivatives and the addition of some form of artificial dissipation for capturing the shock waves.

In contrast, for Euler equations, there are a variety of schemes which produce sufficient dissipation by non-centred discretization in space. These schemes (monotone, total variation diminishing, flux splitting, flux difference, lambda) employ some form of

upwind differencing under the assumption of characteristic theory and wave propagation. The work of Steger & Warming [50], van Leer[23, 24], Osher and Chakravarthy[51], Roe [52] and Harten [25] all fall in this category. This approach is attractive because it closely relates the inviscid physical features of the problem to the spatial discretization schemes. High resolution of shock waves is achieved. The drawback of such an approach is its complexity, chiefly in multidimensional problems. Moreover all of these schemes were originated from Euler solutions and the high resolution feature for shock waves does not always exist for shear layers with these schemes as has recently been discovered in [53]. These are supposed to be the two major obstacles for their application to multidimensional N-S solutions.

As pointed out by Pulliam [54], an upwind scheme is equivalent to a central differencing scheme plus a certain form of dissipation. He illustrated the upwind connection to artificial dissipation using the plus-minus flux splitting method of Steger and Warming [50]. Yee and Harten [55] also demonstrated that a TVD scheme is equivalent to a central differencing scheme plus a more sophisticated dissipation term.

As mentioned previously, one recent trend is to use relaxation methods with unfactored implicit operators. An upwind scheme usually yields an implicit operator with a better matrix property, which is a desirable feature for a successful use of relaxation methods. Chakravarthy [46] related the diagonal dominance of the coefficient matrix with the TVD property of the discretization scheme. This important advantage possessed by some upwind schemes would be able to make them superior to central difference schemes for fast steady state solution because this property allows efficient relaxation procedures to be used. Mulder [48], Chakravarthy [46], Thomas and Walters [49] have recently presented some preliminary while interesting investigations along this line.

In conclusion, since the central differencing schemes are comparatively simple and more flexible, they are preferable at the present time for compressible N-S solutions provided the artificial dissipation is added properly. In fact, upwind schemes can be

used to guide the development of nonoscillatory, robust and efficient artificial dissipation schemes. On the other hand, upwind schemes usually provide better resolution of discontinuities, especially shock waves, and can become competitive in the near future to central differencing for steady state solutions in efficiency by using appropriate relaxation methods to solve the resulting large sparse linear system.

#### 3.2.4 Multigrid Acceleration

While the available theorems in the mathematical theory of multigrid methods generally assume ellipticity [9], the multigrid idea and schemes have been applied to accelerate time marching methods in CFD with great success. Ni [10] was the first to propose a multiple-grid scheme to accelerate time marching Euler solutions with a Lax-Wendroff type explicit method. The motivation was to propagate waves more efficiently on coarser grids whilst maintaining the fine grid accuracy. This acceleration procedure was then applied by Johnson [11] to the time marching N-S solution with the MacCormack explicit method as the fine grid scheme.

A more direct application of the mathematical multigrid method is the application of the full approximation scheme (FAS) [14, 15] to accelerate time marching schemes. Jameson [12] used the FAS multigrid scheme to accelerate his explicit Runge-Kutta calculations. This FAS multigrid scheme, a nonlinear multigrid scheme, is based on the fact that iterative methods usually work well in reducing high frequency errors while low frequency errors can be reduced more efficiently on coarser grids.

Although these two types of time stepping multigrid methods are now becoming popular for acceleration of steady state Euler or N-S solutions, the success of their application is problem dependent. Also there are so many factors in the multigrid procedures, i.e. the cycling strategy, the level number, the iteration number on each grid, which can influence the convergence that extensive numerical experiments are necessary if an optimum is to be found.

### 3.3 Implicit Solution of LCNSE

For rapid achievement of steady state, implicit schemes were preferred to explicit schemes in this research. Two implicit schemes were applied to the locally conical N–S equations. Their formulation and special considerations required for this particular application are discussed in this section. Special features of these two schemes and a comparison of their accuracy and efficiency are also addressed.

#### 3.3.1 MacCormack Implicit Scheme for LCNSE

Since the details of the numerical integration method has been contained in MacCormack's original paper [7], the scheme outlined here will provide details more specific to the problem being analyzed, i.e. the problems governed by the locally conical N–S equations. The solution procedures are included to describe clearly the scheme, especially the implicit boundary treatment.

##### 3.3.1.1 Formulation

Eq. (2.27) may be integrated in time by the following implicit predictor–corrector set of finite difference equations:

Predictor:

$$\begin{aligned}\Delta U_{i,j}^n &= -\Delta t (\Delta_+ F_{i,j}^n / \Delta \theta + \Delta_+ G_{i,j}^n / \Delta \varphi + H_{i,j}^n) \\ [ I - (\Delta t / \Delta \theta) \Delta_+ |A^n| \cdot ] [ I - (\Delta t / \Delta \varphi) \Delta_+ |B^n| \cdot ] \overline{\delta U_{i,j}^{n+1}} &= \Delta U_{i,j}^n \quad (3-1a) \\ \overline{U_{i,j}^{n+1}} &= U_{i,j}^n + \overline{\delta U_{i,j}^{n+1}}\end{aligned}$$

Corrector:

$$\begin{aligned} \Delta \overline{U_{i,j}^{n+1}} &= -\Delta t (\Delta_- \overline{F_{i,j}^{n+1}} / \Delta \theta + \Delta_- \overline{G_{i,j}^{n+1}} / \Delta \varphi + \overline{H_{i,j}^{n+1}}) \\ [I + (\Delta t / \Delta \theta) \Delta_- |A^{n+1}| \cdot] [I + (\Delta t / \Delta \varphi) \Delta_- |B^{n+1}| \cdot] \delta U_{i,j}^{n+1} &= \Delta \overline{U_{i,j}^{n+1}} \quad (3-1b) \\ U_{i,j}^{n+1} &= (1/2) (U_{i,j}^n + \overline{U_{i,j}^{n+1}} + \delta U_{i,j}^{n+1}) \end{aligned}$$

In these equations,  $(\Delta_+ / \Delta \varphi)$  and  $(\Delta_- / \Delta \theta)$  are one-sided forward and backward differences, respectively.  $|A|$  and  $|B|$  are matrices with positive eigenvalues and are related to the Jacobians  $A_I = (\partial F_I / \partial U)$  and  $B_I = (\partial G_I / \partial U)$ , and  $I$  is the unit matrix. The dots in the equations indicate that the differences operate on all the factors to the right. The inviscid Jacobians  $A_I$  and  $B_I$  can be diagonalized by  $S_\theta$  and  $S_\varphi$ , that is,

$$A_I = S_\theta^{-1} \Lambda_A S_\theta \quad B_I = S_\varphi^{-1} \Lambda_B S_\varphi \quad (3-2)$$

where

$$\Lambda_A = \begin{bmatrix} u_\theta & 0 & 0 & 0 & 0 \\ 0 & u_\theta & 0 & 0 & 0 \\ 0 & 0 & u_\theta + c & 0 & 0 \\ 0 & 0 & 0 & u_\theta & 0 \\ 0 & 0 & 0 & 0 & u_\theta - c \end{bmatrix}, \quad \Lambda_B = \begin{bmatrix} u_\varphi & 0 & 0 & 0 & 0 \\ 0 & u_\varphi & 0 & 0 & 0 \\ 0 & 0 & u_\varphi & 0 & 0 \\ 0 & 0 & 0 & u_\varphi + c & 0 \\ 0 & 0 & 0 & 0 & u_\varphi - c \end{bmatrix} \quad (3-3)$$

and  $A_I$ ,  $B_I$ , are given in Appendix A and  $S_\theta$ ,  $S_\theta^{-1}$ ,  $S_\varphi$  and  $S_\varphi^{-1}$  are given in Appendix B. The matrices  $|A|$  and  $|B|$  in Eqs. (3-1a) and (3-1b) are formed by replacing the diagonal matrices  $\Lambda_A$  and  $\Lambda_B$  with positive valued diagonal matrices  $D_A$  and  $D_B$ . The matrices  $|A|$  and  $|B|$  are thus defined by

$$|A| = S_\theta^{-1} D_A S_\theta \quad |B| = S_\varphi^{-1} D_B S_\varphi \quad (3-4)$$

where  $D_A$  and  $D_B$  are diagonal matrices defined by

$$D_A = \max ( |\Lambda_A| + \bar{\lambda}_A I, 0.0 ), \quad D_B = \max ( |\Lambda_B| + \bar{\lambda}_B I, 0.0 ) \quad (3-5)$$

In the above expressions,  $|\Lambda_A|$  and  $|\Lambda_B|$  are diagonal matrices with absolute value elements of  $\Lambda_A$  and  $\Lambda_B$  and

$$\bar{\lambda}_A = \frac{2\nu}{\rho\Delta\theta Re_{\infty,r}} - \frac{1}{2} \frac{\Delta\theta}{\Delta t}, \quad \bar{\lambda}_B = \frac{2\nu}{\rho\sin\theta\Delta\varphi Re_{\infty,r}} - \frac{1}{2} \frac{\sin\theta\Delta\varphi}{\Delta t} \quad (3-6)$$

with

$$\nu = \max \left( \frac{4}{3}\mu, \frac{\gamma}{Pr}\mu \right).$$

Viscous effects are included in the implicit operator through the coefficient  $\nu$ .

For regions of the flow in which  $\Delta t$  satisfies the following explicit stability conditions

$$\begin{aligned} \Delta t &\leq \frac{1}{2} \frac{1}{(|u_\theta|+c)/\Delta\theta + 2\nu/\rho\Delta\theta^2 Re_{\infty,r}}, \\ \Delta t &\leq \frac{1}{2} \frac{1}{(|u_\varphi|+c)/\Delta\varphi\sin\theta + 2\nu/\rho(\sin\theta\Delta\varphi)^2 Re_{\infty,r}}, \end{aligned} \quad (3-7)$$

$D_A$  and  $D_B$  vanish and the set of difference equations (3-1) reduces to the well-known MacCormack explicit method. In that case,

$$\overline{\delta U_{i,j}^{n+1}} = \Delta U_{i,j}^n, \quad \delta U_{i,j}^{n+1} = \overline{\Delta U_{i,j}^{n+1}}$$

### 3.3.1.2 Solution procedure and numerical boundary conditions

Supposing  $\theta_I$  is the outer flow boundary,  $\theta_1$  is the wall boundary, and  $\varphi_{1+\frac{1}{2}}$ ,  $\varphi_{J-\frac{1}{2}}$  are the symmetry boundaries, the solution procedure and the explicit and implicit boundary condition treatment is given below.

Predictor:

- 1) Calculate the explicit increment  $\Delta U_{i,j}^n$  from (3-1a)
- 2) For  $j=2,3, \dots, J-1$

$$i=I-1, I-2, \dots, 2,$$

calculate  $\delta u_{i,j}^*$  from

$$\left(I + \frac{\Delta t}{\Delta \theta_i} |A|_{i,j}^n\right) \delta U_{i,j}^* = \Delta U_{i,j}^n + \frac{\Delta t}{\Delta \theta_i} |A|_{i+1,j}^n \delta U_{i+1,j}^* \quad (3-8)$$

As boundary condition at  $i = I$  is fixed to the flow properties at infinity, i.e.  $u_r = u_{r\infty}$ ,  $u_\theta = u_{\theta\infty}$ ,  $u_\varphi = u_{\varphi\infty}$ ,  $T = T_\infty$  and  $p = p_\infty$ , the corresponding implicit boundary condition is  $\delta U_{i,j}^* = 0$ , which starts the above block bidiagonal solution process.

3) For  $i = 2, 3, \dots, I-1$

$$j = J-1, J-2, \dots, 2$$

calculate  $\delta U_{i,j}^{\overline{n+1}}$  from

$$\left(I + \frac{\Delta t}{\Delta \varphi_j} |B|_{i,j}^n\right) \delta U_{i,j}^{\overline{n+1}} = \delta U_{i,j}^* + \frac{\Delta t}{\Delta \varphi_j} |B|_{i,j+1}^n \delta U_{i,j+1}^{\overline{n+1}} \quad (3-9)$$

To start the above procedure, the value

$$|B|_{i,J}^n \delta U_{i,J}^{\overline{n+1}}$$

has to be known.

#### Implicit symmetry boundary condition

As boundary condition at  $j = J - 1/2$  is a symmetry boundary condition, i.e.

$$\begin{aligned} u_{r,i,J} &= u_{r,i,J-1}, \quad u_{\theta,i,J} = u_{\theta,i,J-1}, \quad u_{\varphi,i,J} = -u_{\varphi,i,J-1}, \\ e_{i,J} &= e_{i,J-1}, \quad \rho_{i,J} = \rho_{i,J-1}. \end{aligned} \quad (3-10)$$

The implicit boundary condition is treated correspondingly as:

a) If  $\Delta t$  and  $\Delta \varphi_J$  is so chosen that the scheme reduces to an explicit version at the boundary, then  $|B|_{i,J}^n = 0$ .

b) If a very fine mesh is necessary near the symmetry boundary, an implicit treatment on this boundary corresponding to the explicit boundary condition is

$$\delta U_{i,J}^{\overline{n+1}} = E \delta U_{i,J-1}^{\overline{n+1}}, \quad |B|_{i,J}^n E = E |B|_{i,J-1}^n \quad (3-11)$$

where

$$E = \begin{bmatrix} 1 & 0 & 0 & 0 & 0 \\ 0 & 1 & 0 & 0 & 0 \\ 0 & 0 & 1 & 0 & 0 \\ 0 & 0 & 0 & -1 & 0 \\ 0 & 0 & 0 & 0 & 1 \end{bmatrix} \quad (3-12)$$

Therefore, by substituting (3-11) into (3-9), the following equation is solved for

$$j = J-1$$

$$\left[ I + \frac{\Delta t}{\Delta \varphi} (I-E) |B|_{i,J-1}^n \right] \overline{\delta U_{i,J-1}^{n+1}} = \delta U_{i,J-1}^* \quad (3-13)$$

The matrix on the left hand side can be inverted easily and the solution of the block bidiagonal system (3-9) starts with

$$\overline{\delta U_{i,J-1}^{n+1}} = \begin{bmatrix} 1 & 0 & 0 & 0 & 0 \\ 0 & 1 & 0 & 0 & 0 \\ 0 & 0 & 1 & 0 & 0 \\ \frac{-a_1}{1+a_4} & \frac{-a_2}{1+a_4} & \frac{-a_3}{1+a_4} & \frac{1}{1+a_4} & \frac{-a_5}{1+a_4} \\ 0 & 0 & 0 & 0 & 1 \end{bmatrix} \delta U_{i,J-1}^* \quad (3-14)$$

where

$$a_k = \frac{2\Delta t}{\Delta \varphi_{J-1}} ( |B|_{i,J-1}^n )_{4,k}, \quad k=1,2, \dots, 5$$

c) This boundary condition can also be treated more approximately by taking

$$\overline{\delta U_{i,J-1}^{n+1}} = \delta U_{i,J-1}^n \quad (3-15)$$

Thus

$$|B|_{i,J}^n \delta U_{i,J}^{n+1} = |B|_{i,J}^n E \overline{\delta U_{i,J-1}^{n+1}} = E |B|_{i,J-1}^n \delta U_{i,J-1}^n \quad (3-16)$$

4) Update the solution

$$U_{i,j}^{n+1} = U_{i,j}^n + \overline{\delta U_{i,j}^{n+1}} \quad (3-17)$$

Corrector:

1) Calculate the explicit increment

$$\overline{\Delta U_{i,j}^{n+1}}$$

from Eq.(3-1b).

2) For  $j=2,3, \dots, J-1$

$i=2,3, \dots, I-1,$

calculate  $\delta U_{i,j}^{**}$  from

$$\left( I + \frac{\Delta t}{\Delta \theta_i} |A|_{i,j}^{\overline{n+1}} \right) \delta U_{i,j}^{**} = \overline{\Delta U_{i,j}^{n+1}} + \frac{\Delta t}{\Delta \theta_i} |A|_{i-1,j}^{\overline{n+1}} \delta U_{i-1,j}^{**} \quad (3-18)$$

This procedure necessitates the specification of an implicit boundary condition on the wall.

Implicit wall boundary condition:

a) On the wall, the boundary condition is  $u_r = u_\theta = u_\varphi = 0, T = T_w,$   
 $(\partial p / \partial \theta)_w = 0$  thus the flow state on the wall can be expressed as a function of the  
state away from the wall. Supposing  $p_{1,j} = p_{2,j}$  is used to approximate  $(\partial p / \partial \theta)_w =$   
0, then

$$U_{1,j}^{**} = \sin \theta_1 \begin{bmatrix} \rho_{1,j}^{**} \\ 0 \\ 0 \\ 0 \\ \rho_{1,j}^{**} e_{1,j}^{**} \end{bmatrix} = Q(U_{2,j}^{**}), \quad \delta U_{1,j}^{**} = \frac{\partial Q}{\partial U_{2,j}^{**}} \delta U_{2,j}^{**} \quad (3-19)$$

where

$$\frac{\partial Q}{\partial U_{2,j}^{**}} = \begin{bmatrix} \frac{2\gamma}{T_w} |V| & -\frac{2\gamma}{T_w} u_{r2,j} & -\frac{2\gamma}{T_w} u_{\theta 2,j} & -\frac{2\gamma}{T_w} u_{\varphi 2,j} & \frac{2\gamma}{T_w} \\ 0 & 0 & 0 & 0 & 0 \\ 0 & 0 & 0 & 0 & 0 \\ 0 & 0 & 0 & 0 & 0 \\ |V| & -u_{r2,j} & -u_{\theta 2,j} & -u_{\varphi 2,j} & 1 \end{bmatrix} \quad (3-20)$$

Therefore, the block diagonal solution procedure (3-18) can start with solving

$$\left[ I + \frac{\Delta t}{\Delta \theta_2} \left( |A|_{2,j} - |A|_{1,j} \frac{\partial Q}{\partial U_{2,j}^{**}} \right) \right] \delta U_{2,j}^{**} = \overline{\Delta U_{2,j}^{n+1}} \quad (3-21)$$

b) This boundary condition can also be treated more approximately by taking

$$\delta U_{1,j}^{**} = \frac{\partial Q}{\partial U_{2,j}^{**}} \delta U_{2,j}^{**} = \frac{\partial Q}{\partial U_{2,j}^{**}} \delta U_{2,j}^* \quad (3-22)$$

3) For  $i = 2, 3, \dots, I-1$

$$j = 2, 3, \dots, J-1$$

calculate  $\delta U_{i,j}^{n+1}$  from

$$\left( I + \frac{\Delta t}{\Delta \varphi_j} |B|_{i,j}^{\overline{n+1}} \right) \delta U_{i,j}^{n+1} = \delta U_{i,j}^{**} + \frac{\Delta t}{\Delta \varphi_j} |B|_{i,j-1}^{\overline{n+1}} \delta U_{i,j-1}^{n+1} \quad (3-23)$$

On the symmetry boundary,  $j = 1 + \frac{1}{2}$ , the implicit boundary treatment is similar to that on  $j = J - \frac{1}{2}$ , which will not be repeated here.

In the above procedure, the solution of the block bidiagonal system is carried out making use of the known decomposition of  $|A|$  and  $|B|$ , which reduces the computation in the inversion of the block matrices. For example, to solve Eq. (3-8) in the predictor, the equation is rewritten as

$$S_{\theta i,j}^{-1} \left[ I + \frac{\Delta t}{\Delta \theta_i} (D_A)_{i,j}^n \right] S_{\theta i,j} \delta U_{i,j}^* = \Delta U_{i,j}^n + \frac{\Delta t}{\Delta \theta_i} |A|_{i+1,j}^n \delta U_{i+1,j}^*$$

and can be easily solved as

$$\delta U_{i,j} = S_{\theta i,j}^{-1} \left[ I + \frac{\Delta t}{\Delta \theta_i} (D_A)_{i,j}^n \right]^{-1} S_{\theta i,j} \left[ \Delta U_{i,j}^n + \frac{\Delta t}{\Delta \theta_i} |A|_{i+1,j}^n \delta U_{i+1,j}^* \right].$$

Note that the block matrix inversion is trivial because  $S_{\theta i,j}^{-1}$  and  $S_{\theta i,j}$  are known and  $\left[ I + \frac{\Delta t}{\Delta \theta_i} (D_A)_{i,j}^n \right]$  is diagonal. This in fact means that a block bidiagonal matrix inversion is reduced to a scalar bidiagonal matrix inversion.

It is important to note that all the boundary conditions are treated corresponding to the explicit boundary conditions, which is an approximation of the physical boundary conditions. This treatment was found to be more stable than MacCormack's "zero" or "reflection" treatment of the implicit boundary conditions[7].

It should be noted that explicit adaptive second order artificial viscosity is added in (3.1) to overcome oscillations near the shock waves. This artificial viscosity should be controlled to its minimum to assure the accuracy of viscous parameters on the wall. Details are given in Appendix C.

Compared to the flux vector derivative terms, the source term in Eq. (2-27) has a lower order influence on the stability property of the difference scheme. In fact, the von Neumann stability condition is independent of the source term if the Jacobian of the source term is bounded, as proved in Appendix D-1.

### 3.3.1.3 Features of the scheme

The above method is unconditionally stable, and is second order accurate in both space and time under the condition that  $\nu\Delta t/\rho\Delta\theta^2$  and  $\nu\Delta t/\rho(\Delta\varphi\sin\theta)^2$  remain bounded as  $\Delta t$ ,  $\Delta\theta$  and  $\Delta\varphi$  approach zero.

In addition to this, the following features of this scheme should be pointed out.

a) For regions of the flow satisfying explicit stability criteria, the implicit method reduces to the corresponding explicit method and therefore no more computing time than the explicit scheme is needed in these regions. Due to this feature, the implicit MacCormack scheme is also called *explicit-implicit* or *hybrid* in some literature.

b) Viscous effects are included in the implicit operator in an approximate and very simple way to enhance the stability for viscous flows. Therefore the computation of the implicit operator and its inversion can be done with the help of the knowledge of the inviscid Jacobians. Two block bidiagonal matrix inversions are reduced to two scalar bidiagonal matrix inversions, a fact which greatly reduces the computation.

c) Although the scheme is unconditionally stable in von Neumann's sense,  $\Delta t$  is still limited in practical computation, which is considered to be mainly due to the error created by approximate factorization taken in the procedure and the approximate linearization.

d) An intrinsic property of the two-step MacCormack type schemes, explicit or implicit, is the time step dependence of the steady state solution, as analyzed in Appendix E. Thus, convergent steady state solutions may only be reliable with sufficiently small  $\Delta t$ . Therefore one measure to achieve spatial accuracy is to reduce time step towards the end of the marching until variation of the solution with this reduction diminishes. This is obviously a disadvantage of the scheme for steady state solutions.

### 3.3.2 A Simplified Beam-Warming Implicit Scheme for LCNSE

#### 3.3.2.1 Beam-Warming implicit scheme

If the inviscid and the viscous parts in the flux vectors and the source term are split, the LCNS equations can be written as

$$\frac{\partial U}{\partial t} + \frac{\partial F_I}{\partial \theta} + \frac{\partial G_I}{\partial \varphi} + H_I = \frac{\partial F_V}{\partial \theta} + \frac{\partial G_V}{\partial \varphi} + H_V. \quad (3-24)$$

By using backward Euler implicit time discretization, the equation can be discretized in time as follows,

$$\frac{U^{n+1} - U^n}{\Delta t} + \frac{\partial F_I^{n+1}}{\partial \theta} + \frac{\partial G_I^{n+1}}{\partial \varphi} + H_I^{n+1} = \frac{\partial F_V^{n+1}}{\partial \theta} + \frac{\partial G_V^{n+1}}{\partial \varphi} + H_V^{n+1}. \quad (3-25)$$

Linearization of the nonlinear flux vectors and the source term gives

$$F_I^{n+1} = F_I^n + \frac{\partial F_I^n}{\partial U} (U^{n+1} - U^n) + O(\Delta t^2), \quad (3-26)$$

$$G_I^{n+1} = G_I^n + \frac{\partial G_I^n}{\partial U} (U^{n+1} - U^n) + O(\Delta t^2), \quad (3-27)$$

$$H_I^{n+1} = H_I^n + \frac{\partial H_I^n}{\partial U} (U^{n+1} - U^n) + O(\Delta t^2). \quad (3-28)$$

If the viscous flux vectors are further split into two parts as

$$F_V = F_{V_1}(U, U_\theta) + F_{V_2}(U, U_\varphi), \quad (3-29)$$

$$G_V = G_{V_1}(U, U_\theta) + G_{V_2}(U, U_\varphi), \quad (3-30)$$

where  $U_\theta = \partial U / \partial \theta$ ,  $U_\varphi = \partial U / \partial \varphi$ , the linearization is

$$F_{V_1}^{n+1} = F_{V_1}^n + \frac{\partial F_{V_1}^n}{\partial U} (U^{n+1} - U^n) + \frac{\partial F_{V_1}^n}{\partial U_\theta} (U_\theta^{n+1} - U_\theta^n) + O(\Delta t^2), \quad (3-31)$$

$$F_{V_2}^{n+1} = F_{V_2}^n + \frac{\partial F_{V_2}^n}{\partial U} (U^{n+1} - U^n) + \frac{\partial F_{V_2}^n}{\partial U_\varphi} (U_\varphi^{n+1} - U_\varphi^n) + O(\Delta t^2), \quad (3-32)$$

$$G_{V_1}^{n+1} = G_{V_1}^n + \frac{\partial G_{V_1}^n}{\partial U} (U^{n+1} - U^n) + \frac{\partial G_{V_1}^n}{\partial U_\theta} (U_\theta^{n+1} - U_\theta^n) + O(\Delta t^2), \quad (3-33)$$

$$G_{V_2}^{n+1} = G_{V_2}^n + \frac{\partial G_{V_2}^n}{\partial U} (U^{n+1} - U^n) + \frac{\partial G_{V_2}^n}{\partial U_\varphi} (U_\varphi^{n+1} - U_\varphi^n) + O(\Delta t^2), \quad (3-34)$$

$$\begin{aligned} H_V^{n+1} = & H_V^n + \frac{\partial H_V^n}{\partial U} (U^{n+1} - U^n) + \frac{\partial H_V^n}{\partial U_\theta} (U_\theta^{n+1} - U_\theta^n) \\ & + \frac{\partial H_V^n}{\partial U_\varphi} (U_\varphi^{n+1} - U_\varphi^n) + O(\Delta t^2). \end{aligned} \quad (3-35)$$

After the above linearization, the equation can be written in the following delta form as

$$\begin{aligned} & \left[ \frac{1}{\Delta t} I + \frac{\partial}{\partial \theta} (A_I - P + R_\theta - M - X + Y_\varphi)^n - \frac{\partial^2}{\partial \theta^2} R^n \right. \\ & \quad + \frac{\partial}{\partial \varphi} (B_I - Q + S_\varphi - N - W + Z_\theta)^n - \frac{\partial^2}{\partial \varphi^2} S^n \\ & \quad \left. - \frac{\partial^2}{\partial \theta \partial \varphi} (Y + Z)^n + (C_I - L + M_\theta + N_\varphi)^n \right] \Delta U^n \\ & = - \left( \frac{\partial F_I}{\partial \theta} + \frac{\partial G_I}{\partial \varphi} + H_I \right)^n + \left( \frac{\partial F_V}{\partial \theta} + \frac{\partial G_V}{\partial \varphi} + H_V \right)^n + O(\Delta t), \end{aligned} \quad (3-36)$$

$$U^{n+1} = U^n + \Delta U^n.$$

The Jacobians in the above equations are

$$\begin{aligned}
 A_I &= \frac{\partial F_I}{\partial U} & P &= \frac{\partial F_{V1}}{\partial U} & R &= \frac{\partial F_{V1}}{\partial U_\theta} & X &= \frac{\partial F_{V2}}{\partial U} & Y &= \frac{\partial F_{V2}}{\partial U_\varphi} \\
 B_I &= \frac{\partial G_I}{\partial U} & Q &= \frac{\partial G_{V2}}{\partial U} & S &= \frac{\partial G_{V2}}{\partial U_\varphi} & W &= \frac{\partial G_{V1}}{\partial U} & Z &= \frac{\partial G_{V1}}{\partial U_\theta} \\
 C_I &= \frac{\partial H_I}{\partial U} & L &= \frac{\partial H_V}{\partial U} & M &= \frac{\partial H_V}{\partial U_\theta} & N &= \frac{\partial H_V}{\partial U_\varphi} .
 \end{aligned} \tag{3-37}$$

Beam and Warming [8] used approximate factorization for a direct solution of the equation by solving two block tridiagonal systems. For that purpose, cross derivatives should be avoided by lagging the following two terms in time,

$$\Delta F_{V2}^n = \Delta F_{V2}^{n-1} + O(\Delta t^2), \quad \Delta G_{V1}^n = \Delta G_{V1}^{n-1} + O(\Delta t^2). \tag{3-38}$$

In this case the Jacobians X, Y, W and Z in (3-36) vanish and three time levels are involved.

### 3.3.2.2 Simplification of the implicit procedure

It is difficult to derive analytically all the Jacobians listed in Eq. (3-37). Fortunately, for steady state solution, only the spatial accuracy is the major concern. From the delta form of Eq. (3-36), the spatial accuracy of the steady state solution is determined by the right hand side, RHS, in Eq. (3-36). The implicit operator can only influence the convergence to the steady state. A simplified implicit operator is presented here, which includes the inviscid Jacobians and representative viscous Jacobians to enhance stability. The factorized simplified form is expressed as

$$\begin{aligned}
 [ I + \Delta t ( \frac{\partial}{\partial \theta} A_I \cdot - \frac{\partial^2}{\partial \theta^2} R \cdot ) ] [ I + \Delta t ( \frac{\partial}{\partial \varphi} B_I \cdot - \frac{\partial^2}{\partial \varphi^2} S \cdot ) ] \Delta U^n &= RHS^n \Delta t, \\
 U^{n+1} &= U^n + \Delta U^n,
 \end{aligned} \tag{3-39}$$

where  $A_I$ ,  $B_I$ ,  $R$ , and  $S$  are given in Appendix A. As has been analyzed previously in the MacCormack implicit scheme, the source term is treated explicitly.

### 3.3.2.3 Solution procedure and numerical boundary conditions

Supposing  $\theta_I$  is the outer boundary,  $\theta_1$  is the wall boundary, and  $\varphi_{1+\frac{1}{2}}$ , and  $\varphi_{J-\frac{1}{2}}$  are the symmetry boundaries.

1) Calculate the right hand side of (3-36) or the residuals

$$\text{RHS}^n = -\left( \frac{\Delta F}{\Delta \theta} + \frac{\Delta G}{\Delta \varphi} + H \right)_{i,j}^n. \quad (3-40)$$

2) Solve the block tridiagonal system

$$\left[ I + \Delta t \left( \frac{\Delta}{\Delta \theta} A_I^n - \frac{\Delta^2}{\Delta \theta^2} R^n \right) \right] \Delta U^* = \Delta t \text{ RHS}^n, \quad (3-41)$$

i.e.

$$B_{i,j} \Delta U_{i-1,j}^* + D_{i,j} \Delta U_{i,j}^* + C_{i,j} \Delta U_{i+1,j}^* = \Delta t \text{ RHS}^n, \quad (3-42)$$

$$\begin{aligned} i &= 3, 4, \dots, I-2, \\ j &= 2, 3, \dots, J-1, \end{aligned}$$

where

$$\begin{aligned} B_{i,j} &= -\frac{\Delta t}{\theta_{i+1} - \theta_{i-1}} A_{i-1,j} - \frac{\Delta t}{\Delta \theta_i^2} R_{i-1,j}, \\ D_{i,j} &= I + \frac{2}{\Delta \theta_i^2} R_{i,j}, \\ C_{i,j} &= \frac{\Delta t}{\theta_{i+1} - \theta_{i-1}} A_{i+1,j} - \frac{\Delta t}{\Delta \theta_i^2} R_{i+1,j}. \end{aligned} \quad (3-43)$$

a) For  $i=I-1$ , the boundary condition at  $i=I$  has to be embedded in the implicit operator,

$$\Delta U_{I,j}^* = 0, \quad B_{I-1,j} \Delta U_{I-2,j}^* + D_{I-1,j} \Delta U_{I-1,j}^* = \Delta t \text{ RHS}_{I-1,j}^*. \quad (3-44)$$

b) For  $i=2$ , implicit wall boundary condition is applied to evaluate  $\Delta U_{1,j}^*$ .

$$B_{2,j} \Delta U_{1,j}^* = \left[ -\frac{\Delta t}{\theta_3 - \theta_1} A_{1,j} - \frac{\Delta t}{\Delta \theta_2^2} R_{1,j} \right] \Delta U_{1,j}^*. \quad (3-45)$$

It is easy to verify that on the wall  $R_{1,j} \Delta U_{1,j}^* = 0$  and

$$A_{I_1, j} \Delta U_{1, j}^* = \begin{bmatrix} 0 & 0 & 0 & 0 & 0 \\ 0 & 0 & 0 & 0 & 0 \\ \alpha^* & -u_r^* & -u_\theta^* & -u_\varphi^* & 1 \\ 0 & 0 & 0 & 0 & 0 \\ 0 & 0 & 0 & 0 & 0 \end{bmatrix} \Delta U_{2, j}^* \frac{\beta \sin \theta_1}{\sin \theta_2}. \quad (3-46)$$

Therefore

$$B_{2, j} \Delta U_{1, j}^* = \bar{B}_{2, j} \Delta U_{2, j}^* \quad (3-47)$$

and the equation to be solved on the wall boundary is

$$(D_{2, j} + \bar{B}_{2, j}) \Delta U_{2, j}^* + C_{2, j} \Delta U_{3, j}^* = \Delta t \text{RHS}_{2, j}. \quad (3-48)$$

3) Solve the block tridiagonal system

$$[I + \Delta t (\frac{\Delta}{\Delta \varphi} B_I \cdot - \frac{\Delta^2}{\Delta \varphi^2} S^n \cdot)] \Delta U = \Delta U^*, \quad (3-49)$$

i.e.

$$E_{i, j} \Delta U_{i, j-1} + G_{i, j} \Delta U_{i, j} + F_{i, j} \Delta U_{i, j+1} = \Delta U_{i, j}^*, \quad (3-50)$$

$$j = 3, 4, \dots, J-2, \\ i = 2, 3, \dots, I-1,$$

where

$$E_{i, j} = - \frac{\Delta t}{\varphi_{i+1} - \varphi_{i-1}} B_{I i, j-1}^n - \frac{\Delta t}{\Delta \varphi_j^2} S_{i, j-1}^n, \\ G_{i, j} = I + \frac{2}{\Delta \varphi_j^2} S_{i, j}^n, \quad (3-51) \\ F_{i, j} = \frac{\Delta t}{\varphi_{j+1} - \varphi_{j-1}} B_{I i, j+1}^n - \frac{\Delta t}{\Delta \varphi_j^2} S_{i, j+1}^n.$$

On the symmetry boundaries

$$\Delta U_{i, 1} = E \Delta U_{i, 2}, \quad \Delta U_{i, J} = E \Delta U_{i, J-1}. \quad (3-52)$$

The equations on the symmetry boundaries are

$$(G_{i, 2} + E_{i, 2} I_1) \Delta U_{i, 2} + F_{i, 2} \Delta U_{i, 3} = \Delta U_{i, 2}^*, \quad (3-53)$$

$$E_{i, J-1} \Delta U_{i, J-2} + (G_{i, J-1} + F_{i, J-1} I_1) \Delta U_{i, J-1} = \Delta U_{i, J-1}^*. \quad (3-54)$$

4) Update the solution

$$U^{n+1} = U^n + \Delta U^n. \quad (3-55)$$

It should be noted that in the shock-capturing hypersonic simulation of this research (presented in Chap.4) a second order adaptive artificial viscosity was added to the right hand side of (3-39) and a corresponding second order implicit term was added to the left hand side for stability. The fourth order artificial dissipation term, usually used in Euler solutions, was found unnecessary for the present N-S solutions and it degraded the accuracy of viscous parameters on the wall. Details of the adaptive artificial viscosity is given in Appendix C.

#### 3.3.2.4 Features of the scheme

The simplified Beam-Warming scheme presented above is second order accurate as far as the spatial accuracy is concerned. The implicit time marching is unconditionally stable in von Neumann stability analysis.

It is obvious from the above procedure that the implicit scheme needs to solve two general block tridiagonal systems. Because  $A_I$  and  $R$ , and  $B_I$  and  $S$  cannot be diagonalized simultaneously, this block tridiagonal system cannot be reduced to a scalar tridiagonal system as has been done in the inviscid case by Pulliam and Chaussee [56] or in the implicit MacCormack scheme for the LCNSE presented previously.

Some authors suggest omitting completely the viscous effects in the implicit operator to simplify the implicit procedure. This, of course, will not influence the accuracy of the steady state solution. However the purpose of implicitization is to relieve the severe stability condition for high Reynolds number N-S solution. Therefore the influence of explicit viscous treatment on stability needs to be analyzed. This is investigated in Appendix D with a scalar convection-diffusion equation modelling. It is

found that if only the inviscid term is treated implicitly while the viscous term is ignored in the implicit operator, the time step is limited by the viscous effects, which can be severe in the viscous region where the mesh is very fine. Therefore the advantage of the implicit scheme is lost for viscous solutions, if viscous effects are not taken into account in the implicit operator.

On the other hand, because of the generality of the block tridiagonal solution, the implicit boundary conditions are evidently easier to be embedded in the solution procedure.

In contrast to the implicit MacCormack scheme presented in Sec. 3.3.1, an important advantage of the simplified Beam-Warming scheme is that accurate steady state solutions can be achieved with large time steps because the formulation separates the time discretization from spatial discretization and, therefore, indicates a time step independence of a steady state solution. This point is analyzed in Appendix E.

Again, as in the MacCormack implicit scheme, the time step in practical computation is still limited due to the errors introduced by (1) the approximate factorization; (2) the imperfect linearization. Therefore in practical computation, an optimum time step needs to be found by numerical testing for best convergence to the steady state.

### 3.3.3 A Comparative Study of the Two Implicit Schemes

To compare the two implicit schemes, some statistical data from the numerical simulation of this research is shown in Table 3.1. The total computation time shown in the table is the time for convergence. Because the convergence criteria are different — maximum relative error  $\max |U^{n+1} - U^n| / \Delta t$  is used in the MacCormack implicit scheme and the root mean square of the residuals is used in the simplified

Beam-Warming scheme — a strict comparison of convergence is not convenient. However, a same physical non-dimensional time of about 2 is found for all the cases to reach a converged flowfield with the pressure distribution and all the shock waves reaching their steady state. From (2-26), this means the time for flowfield convergence is roughly the time for the incoming flow to sweep twice from the vertex to the computation station. This convergence criterion is used for the comparison of the two implicit schemes in the following table. It should be noted that viscous parameters such as heat transfer needed longer time to settle down to their steady state.

Table 3.1 Computation time comparison, LCNSE solution, mesh 65x65

Algorithm	time step $\Delta t$	ICL 2988 computing time, cpu	
		per time step per grid point (second)	total to convergence (hour)
MacCormack explicit	0.0001	$0.269 \times 10^{-2}$	63.14 *
MacCormack implicit	0.005	$0.343 \times 10^{-2}$	1.61
Simplified B-W implicit	0.02	$0.302 \times 10^{-1}$	3.54

\* Estimated

From Table 3.1, it is clear that both of the implicit schemes are marginally more efficient than the explicit scheme for steady state solutions. Due to the very fine mesh near the wall, the time step used in the explicit scheme was severely limited by the stability condition (3-7) while the implicit procedure could march in time with much larger steps. Steady state solution of the problem with an explicit scheme is prohibitive on the computer available.

It is interesting to note the small difference in CPU time per time step between

the MacCormack explicit and implicit schemes. This is partly due to the low cost of the implicit procedure. It is also attributed to the useful capability of the implicit scheme which can switch automatically to the explicit scheme in regions where implicitization is not necessary.

Also shown in the table is the difference between the two implicit schemes. The computing time of the simplified Beam-Warming scheme per time step is much longer than that of the MacCormack implicit scheme. The reason for this is clear by analyzing the formulation of the two different schemes. The difference is due to the difference in the inversion of two block tridiagonal matrices and that of four scalar bidiagonal systems per time step. On the other hand, it was found that the simplified Beam-Warming scheme can use larger time steps for faster convergence.

Furthermore it should be noted that the accuracy of the steady state solution with the MacCormack implicit scheme may be degraded by large time steps, as analyzed in Appendix E. From numerical experience, whether this  $\Delta t$  dependence is severe is problem dependent. Therefore as a safeguard for the accuracy of the steady state solution in the MacCormack implicit scheme, the time step,  $\Delta t$ , should be reduced at the end of the time marching until no more change appears in the solution with this  $\Delta t$  reduction. However, with the simplified Beam-Warming scheme, the steady state solution only depends on the spatial discretization and, therefore, large time steps will not influence the accuracy of the steady state solution.

Fig. 3.1 shows the heat transfer for the cone-delta-wing combination at  $\alpha = 0^\circ$ . Time step dependence of the MacCormack implicit scheme is clearly revealed by the marginal difference between the solutions of the MacCormack implicit scheme with  $\Delta t_{\text{final}} = 0.005$  and  $\Delta t_{\text{final}} = 0.001$ . However after the final time step was reduced to 0.001, this dependence was overcome and the solution did not change with further reduction of the time step. This converged result agrees with the simplified Beam-Warming solution and the experimental data quite well.

### 3.4 Multigrid Acceleration of the Implicit Schemes

As mentioned in Sec. 3.2, multigrid acceleration schemes are becoming a more widely used tool in CFD. For the Euler and N-S solutions some time stepping multigrid schemes have been proposed to accelerate the convergence of explicit time marching solutions to the steady state. But the multigrid acceleration idea is not confined to explicit schemes. In this section two multigrid schemes are presented for the implicit schemes formulated in the previous sections.

#### 3.4.1 Ni-type Multigrid Acceleration of the MacCormack Implicit Scheme

##### 3.4.1.1 Ni's multigrid idea

In Ni's scheme [10], the Lax-Wendroff finite difference method, which is derived from the Taylor series expansion, is formulated in such a way that the corrections ( $\delta U = U^{n+1} - U^n$ ) at each grid point are related to the changes ( $\Delta U$ ) taking place in the neighbouring control volumes. This formula is called *distribution formula*. After the corrections,  $\delta U^h$ , are calculated on the finest grid using this one-step Lax-Wendroff type method, the corrections are restricted to the next coarser grid and replace the changes,  $\Delta U^{2h}$ , occurring in the control volume of the coarse grid. The distribution formula is then used to obtain corrections,  $\delta U^{2h}$ , on the coarse grid. By bilinear interpolations the corrections at the intermediate fine grid points is filled in and the solution can be updated. It is important to note the difference between the fine grid scheme and the coarse grid one. Instead of using the Lax-Wendroff scheme on the coarse grid, the changes on the coarse grid are restricted from the fine grid corrections. Therefore the coarse grid scheme is in fact a procedure of redistributing the corrections from the fine grid solution through the distribution formula. It is clear that the fine grid spatial accuracy is not influenced by this correction redistribution. The basic idea behind Ni's multigrid scheme is the use of coarse grids to propagate the

fine grid corrections properly and efficiently throughout the field, thus improving convergence rate to the steady state while maintaining low truncation errors.

Based on the above analysis, various methods other than the one-step Lax-Wendroff method can be used for the purpose of generating fine grid corrections. In fact, the MacCormack explicit scheme has been used with Ni's distribution formula for multigrid acceleration [11].

Due to the advantage of implicit methods over explicit methods, especially for N-S solutions where a highly stretched mesh is necessary, it is the author's belief that more efficient procedures can be derived for steady state solutions by combining the advantages of implicit methods and multigrid schemes. It is possible because the implicit corrections can also represent changes on the coarse grid as explicit corrections. The physical meaning of the distribution formula is maintained.

#### 3.4.1.2 Application to the MacCormack implicit scheme

The Ni-type multigrid procedure is used with the implicit MacCormack method presented in the last section as follows.

Define successively coarse grids by successive deletion of every other line in each coordinate direction. This necessitates the definition of the mesh number as  $m \cdot 2^p + 1$ .

1) The implicit corrections on the finest grid are defined as

$$\delta U_{i,j}^h = U_{i,j}^{n+1} - U_{i,j}^n = \frac{1}{2} ( \delta \overline{U_{i,j}^{n+1}} + \delta U_{i,j}^{n+1} ) \quad (3-56)$$

from (3-1).

2) These fine grid corrections are restricted to the changes occurring in the coarse grid control volumes, i.e.

$$\Delta U^{2h} = I_{2h}^h \delta U^h. \quad (3-57)$$

3) The distribution formula is used to calculate corrections on the coarse grid points. Ni's distribution formula was derived without a source term. From the same idea of Taylor expansion, distribution formula with a source term is derived as follows,

$$\begin{aligned} \delta U_{i,j}^{2h} = & \frac{1}{4} [ \Delta U - \Delta t ( \frac{\Delta F}{\Delta \theta} + \frac{\Delta G}{\Delta \varphi} + \frac{1}{2} \Delta H ) ]_{i+1,j+1} \\ & + \frac{1}{4} [ \Delta U - \Delta t ( \frac{\Delta F}{\Delta \theta} - \frac{\Delta G}{\Delta \varphi} + \frac{1}{2} \Delta H ) ]_{i+1,j-1} \\ & + \frac{1}{4} [ \Delta U - \Delta t ( -\frac{\Delta F}{\Delta \theta} + \frac{\Delta G}{\Delta \varphi} + \frac{1}{2} \Delta H ) ]_{i-1,j+1} \\ & + \frac{1}{4} [ \Delta U - \Delta t ( -\frac{\Delta F}{\Delta \theta} - \frac{\Delta G}{\Delta \varphi} + \frac{1}{2} \Delta H ) ]_{i-1,j-1}, \end{aligned} \quad (3-58)$$

where  $(i+1,j+1)$ ,  $(i+1,j-1)$ ,  $(i-1,j+1)$  and  $(i-1,j-1)$  represent the four coarse grid control volumes surrounding the coarse grid point  $(i,j)$ , as shown in Fig. 3.2(a). Derivation of the above distribution formula for one dimensional case is illustrated in Appendix F.

4) Interpolate the coarse grid corrections calculated from the distribution formula (3-58) back to the fine grid and update the solution, i.e.

$$\delta U_{\text{new}}^h = I_{2h}^h \delta U^{2h}, \quad (3-59)$$

$$U_{\text{new}} = U + \delta U_{\text{new}}^h. \quad (3-60)$$

The procedure is illustrated in Fig. 3.2.

Because the coarse grid scheme (3-58) is a wave propagation procedure, it implies a convection mechanism as pointed out by Johnson [11]. Therefore in the present N-S solutions the coarse grid scheme only involves inviscid Jacobians, which makes the multigrid scheme more efficient. That is in the distribution formula

$$\Delta F = \frac{\partial F}{\partial U} I \Delta U, \quad \Delta G = \frac{\partial G}{\partial U} I \Delta U, \quad \Delta H = \frac{\partial H}{\partial U} I \Delta U. \quad (3-61)$$

For stability a local time step, which is determined by the local inviscid stability condition, is used in the coarse grid scheme,

$$\Delta t = \text{CFL} \min \left[ \frac{\Delta \theta}{|u_\theta| + c}, \frac{\sin \theta \Delta \varphi}{|u_\varphi| + c} \right], \quad \text{CFL} \leq 1. \quad (3-62)$$

The above procedure is repeated on successively coarser grids until the coarsest grid is reached. The strategy used in the present multigrid cycling is the sawtooth cycling.

### 3.4.1.3 Numerical test

In Fig. 3.3 convergence histories are shown against a work unit, which is defined as the unit CPU time for one time step using the MacCormack explicit method. The case taken for this test is the cone case with  $M_\infty = 7.95$  and  $\alpha = 0^\circ$  (computation details can be found in Chap. 4).

The Ni-type multigrid scheme has evidently accelerated both the explicit and the implicit schemes. A marginal difference in the convergence is shown again between the explicit and the implicit schemes. The figure shows that the implicit scheme with a two level multigrid is the most efficient approach.

By monitoring the shock position during the time marching, it was observed that the multigrid scheme particularly speeded up the movement of the shock wave from the wall to its steady position. This corresponds to the physical meaning of Ni-type multigrid method and the inviscid nature of the present coarse grid scheme.

## 3.4.2 FAS Multigrid Acceleration of the Simplified Beam-Warming Implicit Scheme

### 3.4.2.1 Full approximation scheme (FAS)

The original idea behind the multigrid method is that on a given grid relaxation

methods generally work well in reducing high frequency components of the error but poorly reducing low frequency components. A multigrid approach uses a relaxation scheme to smooth the high frequency error on the fine grid and then use successively coarse grids to reduce the low frequency error [14, 15].

Consider the discrete nonlinear problem arising from the discretization of PDE,

$$R_h(U_h) = f_h, \quad (\Omega_h). \quad (3-63)$$

The FAS nonlinear multigrid scheme can be presented as follows.

Let  $U_h^*$  be an approximation of the solution  $U_h$  of (3-63), which is obtained after  $\nu_1$  relaxations. Denote the error of  $U_h^*$  by

$$v_h = U_h - U_h^* \quad (3-64)$$

and the defect of  $U_h^*$  by

$$d_h = f_h - R_h(U_h^*) \quad (3-65)$$

Trivially, the  $\Omega_h$ -defect equation

$$R_h(U_h^* + v_h) - R_h(U_h^*) = d_h \quad (3-66)$$

is equivalent to the original Eq. (3-63), yielding

$$U_h = U_h^* + v_h. \quad (3-67)$$

Eq.(3-66) is approximated on  $\Omega_H$  by

$$R_H(U_H^* + v_H) - R_H(U_H^*) = d_H \quad (3-68)$$

or equivalently by

$$R_H(W_H) = d_H + R_H(U_H^*) = f_H, \quad v_H = W_H - U_H^*. \quad (3-69)$$

After the solution on the coarse grid  $\Omega_H$  is obtained, the error  $v_H$  can then be interpolated to  $v_h$  on the fine grid  $\Omega_h$  and the solution on the fine grid can be updated by (3-67). After  $\nu_2$  relaxation on the fine grid a new solution  $U_h^{**}$  is obtained.

The procedure for solving (3-63) can be used to solve (3-69) and a multigrid cycling results.

It is important to note that transferred back to the fine grid  $\Omega_h$  is not  $W_H$  but the correction  $v_H$  since only the correction and the defect quantities are smoothed by the relaxation process and can, therefore, be approximated well on the coarse grid.

### 3.4.2.2 Application to the simplified Beam-Warming scheme

The implicit time marching schemes presented in Sec. 3.3, when used for steady state solutions, can be considered as a relaxation scheme for the steady state problem. After certain time steps ( or iterations ) the high frequency components are reduced and the correction from one time step to the next becomes smooth. Thus a multigrid acceleration can be applied.

Using the simplified Beam-Warming implicit scheme presented in the last section as a relaxation scheme in the FAS multigrid method, the following solution procedure is derived, which is also illustrated in Fig. 3.4.

- 1) Solve Eq.(3-63) by the implicit time marching approach, assuming the initial value  $U_h^n$ .

$$U_h^{n+1} = U_h^n + \Delta U_h. \quad (3-70)$$

After  $\nu_1$  relaxation an approximate solution  $U_h^*$  is obtained.

- 2) Calculate  $R_h(U_h^*)$  and the defect

$$d_h = f_h - R_h(U_h^*). \quad (3-71)$$

- 3) Restrict the fine grid solution to the coarse grid

$$U_{2h}^* = I_{2h}^h U_h^*.$$

4) Restrict the defect to the coarse grid

$$d_{2h} = \tau_{2h}^h d_h. \quad (3-72)$$

5) Solve the coarse grid equation

$$R_{2h}(W_{2h}) = d_{2h} + R_{2h}(U_{2h}^*) = f_{2h} \quad (3-73)$$

using again implicit time marching with  $U_{2h}^*$  as initial value,

$$W_{2h}^{n+1} = W_{2h}^n + \Delta W_{2h} \quad (3-74)$$

and a approximate solution  $W_{2h}^*$  is obtained after  $\nu_1$  time steps.

6) Compute the correction

$$v_{2h} = W_{2h}^* - U_{2h}^*. \quad (3-75)$$

7) Interpolate the correction to fine grid

$$v_h = I_{2h}^h v_{2h}. \quad (3-76)$$

8) Compute the corrected approximation

$$U_h^{**} = U_h^* + v_h. \quad (3-77)$$

9) Solve again

$$R_h(U_h) = f_h \quad (3-78)$$

with time marching of  $\nu_2$  steps using  $U_h^{**}$  as initial value and  $U_h^{***}$  is obtained.

Several time steps can be advanced in each grid level, but a simple procedure was preferred by taking  $\nu_1 = 1$  and  $\nu_2 = 0$ . This means immediately after one step time marching, the solution is updated and restricted to the next coarse grid with the defect. This forms a nonlinear problem on the coarse grid. Using the restricted solution as an initial value, another time step is marched on the coarse grid. This procedure continues until the coarsest grid is reached. After one iteration on the coarsest grid the correction is interpolated back to the successively coarse grids without time marching. The solution on the finest grid is then updated. This sawtooth cycling scheme adds no more storage to the implicit method because  $U_h^* = U_h^{n+1}$  and  $W_{2h}^* = W_{2h}^{n+1}$ .

### 3.4.2.3 Numerical test

Fig. 3.5 shows the convergence histories of the simplified Beam-Warming scheme with and without multigrid acceleration. The test case was the cone case with  $M_\infty = 7.95$  and  $\alpha = 4^\circ$  (Details can be found in Chap.4). A mesh of  $65 \times 17$  was used.

The multigrid acceleration is evident. However, as the FAS multigrid procedure needs to solve LCNSE on the coarse grid, the overall computation saving is not much in the present case. The multigrid was only with one level of coarse grid. A higher level of coarse grid exhibited no more benefit in this case. The FAS multigrid efficiency needs to be further investigated with more numerical testing.

### 3.5 Sparse Quasi-Newton Method for Fast Steady State Solution

#### 3.5.1 Motivation

As discussed previously most of the implicit methods used in CFD, though based on time dependent formulation, are only used to determine the steady state solutions. The time dependent term is, therefore, used merely as a parameter for generating an iterative scheme. The requirement on time accuracy is quite often relaxed in various ways.

If the linearization is *exact*, the implicit scheme will, as  $\Delta t \rightarrow \infty$ , reduce to a Newton iteration method for the nonlinear system derived from the discretization of the steady state equations. The procedure of exact linearization is in fact the procedure of evaluating the Jacobian of the nonlinear system.

Using the exact linearization, Mulder and van Leer [57] found a quadratic convergence to the steady state in the first order flux splitting solution for a nozzle problem. This fast convergence can only be obtained if an applicable procedure exists for the exact linearization (i.e. the evaluation of the Jacobian).

Unfortunately this is seldom the case in practice. The differential equations can be discretized by various methods in space. Some sophisticated schemes have been developed for high resolution of crucial fluid phenomena. The flux vector splitting and TVD schemes, for example, were recently proposed by van Leer[23, 24] and Harten [25] respectively for high resolution of shock waves in gasdynamics. On the other hand, viscous effects may be a dominant factor in the problem and turbulence modelling has often to be involved.

In all these cases, the evaluation of the Jacobian is often too difficult to apply so that different simplifications in constructing the implicit operator are made for a specific discretization scheme or for a specific problem. This process brings about an irretrievable loss of information that exhibits itself in the degradation of the convergence rate. The designer of such an implicit scheme finds himself in the position where he has to compromise convergence rate and generality to achieve a *workable* method. Furthermore the programming effort and computational cost spent in constructing the implicit operator usually still occupy a large portion in each time step, though the incorrect Jacobian already prevents the implicit method from quadratic convergence.

Noting the difficulties in linearization in implicit schemes for most problems in CFD, the author proposed a new strategy, which updates the Jacobian by a sparse quasi-Newton method for the solution of nonlinear system [21, 22]. The sparse quasi-Newton method was first presented by Schubert [16] and Broyden [17]. Superlinear convergence was proved in [18, 19]. To form a successful nonlinear algorithm, this fast local convergence is combined with the robustness of some time dependent approach to form a globally convergent procedure.

### 3.5.2 General Procedure of the Sparse Quasi-Newton Method for Steady State Solutions

In this section a general procedure of the sparse quasi-Newton method is given. Those who are interested in the theoretical aspects can refer to [16–19].

#### 3.5.2.1 Properties of the nonlinear system arising from CFD

Consider the nonlinear system,

$$R(U) = 0, \quad (3-79)$$

which may arise from the discretization of the differential equations governing some physical process in CFD.

The Jacobian  $J(U) = \partial R / \partial U$  has a sparse structure. In other words, each single equation depends on relatively few of the unknowns. Taking advantage of the zero or the sparse structure of  $J$  is crucial in order to solve the problem by a Newton or quasi-Newton method, where the Jacobian or its approximation is needed. The saving in both storage and arithmetic operation by taking advantage of the sparsity is very significant. Furthermore if the discretization scheme is finite differencing, the resulting nonlinear system usually has a regular banded sparsity pattern, e.g. block tridiagonal, block pentadiagonal, and so on.

In spite of this sparsity, the system is usually large. And each single equation can be very complicated. Therefore the analytic expression of the Jacobian is generally unavailable and furthermore the function evaluation is usually very expensive.

Since the Jacobian is usually unavailable, strategies other than the Newton method need to be sought. By making use of the sparse structure, a sparse finite difference Newton method [20] can be devised and the usual  $n$  additional function evaluations can be reduced significantly. This reduction can be seen from the formulation for block tridiagonal and pentadiagonal structured Jacobians in the following section. Although the reduction is remarkable, many function evaluations per iteration may still be too time consuming. To avoid these extra function evaluations, a quasi-Newton approach can be taken, which is one of the most fruitful and successful theories in the field of the numerical solution of nonlinear systems [19].

The basic idea of the quasi-Newton method is to approximate the Jacobian of the nonlinear system using only function values already calculated. However, when solving sparse systems, the advantage of the well-known Broyden method, using an approximation to the inverse of the Jacobian, cannot readily be retained since the

inverse of a sparse matrix is in general not sparse, and the consequent benefit would then be destroyed. Neither is it possible to use equivalent Broyden update on the Jacobian since this consists of adding a single-rank matrix to the old approximate Jacobian to form the new one. This single rank correction is generally not sparse so that again the advantage conferred by sparseness would be lost.

### 3.5.2.2 Sparse quasi-Newton method

To make a full use of sparsity in the quasi-Newton updating of the Jacobian, Schubert [16] and Broyden [17] proposed the sparse quasi-Newton method, which is introduced here to solve problems in CFD.

Define the matrix projection operator  $P_J : \mathbb{R}^{n \times n} \rightarrow \mathbb{R}^{n \times n}$  by

$$(P_J(M))_{ij} = \begin{cases} 0, & \text{if } J(U)_{i,j} = 0 \text{ for all } U \in \mathbb{R}^n \\ M_{i,j}, & \text{otherwise} \end{cases} \quad (3-80)$$

That is  $P_J$  zeros out the elements of  $M$  corresponding to zero position of the sparsity pattern of  $J(U)$ , while otherwise leaving it unchanged. Similarly define  $S_i \in \mathbb{R}^n$  by

$$(S_i)_j = \begin{cases} 0, & \text{if } J(U)_{i,j} = 0 \text{ for all } U \in \mathbb{R}^n \\ S_j, & \text{otherwise} \end{cases} \quad (3-81)$$

That is,  $S_i$  is the result of imposing on  $S$  the sparsity pattern of the  $i$ th row of  $J(U)$ .

The procedure of the sparse quasi-Newton method may be written as following:

Given  $R: \mathbb{R}^n \rightarrow \mathbb{R}^n$ ,  $U^0 \in \mathbb{R}^n$ ,  $A^0 \in \mathbb{R}^{n \times n}$

DO for  $k = 0, 1, 2, \dots$

Solve  $A^k S^k = -R(U^k)$  for  $S^k$

$U^{k+1} = U^k + S^k$

$\Upsilon^k = R(U^{k+1}) - R(U^k)$  (3-82)

$A^{k+1} = A^k + P_J[D^+( \Upsilon^k - A^k S^k )(S^k)^T]$

Here  $D^+ \in \mathbb{R}^{n \times n}$  is a diagonal matrix with

$$(D^+)_{ii} = \begin{cases} 1/(\mathbf{S}_i)^T(\mathbf{S}_i), & \text{if } (\mathbf{S}_i)^T(\mathbf{S}_i) \neq 0 \\ 0, & \text{otherwise.} \end{cases} \quad (3-83)$$

Although constructing the above sequence imposes no analytical assumption on  $R$  and no requirement on the initial value  $U^0$  and  $A^0$ , care has to be exercised to enable a successful application. The above update scheme has been proved to be locally  $q$ -superlinearly convergent under standard assumptions on  $R$  [18, 19] including: (1)  $R$  is continuously differentiable; (2) the existence of the solution  $U^*$ ,  $R(U^*) = 0$ ; (3)  $J(U^*)^{-1}$  exists with  $\|J^{-1}(U^*)\| \leq \beta$ ; (4)  $J$  is Lipschitz continuous.

Since the  $R$  in question is generally complicated, little analytical information about it is known. Thus it is usually impossible to check all the analytical properties of  $R$  before using the method so that numerical experiments are needed. However it is important to note that the fast convergence is a local property and the initial values for the procedure might be needed to be close to the final solution to exhibit this high performance. The basic idea in forming a successful nonlinear algorithm is to combine a fast local convergence strategy with a global convergence strategy in a way that derives benefit from both.

### 3.5.2.3 Initialization and global convergence

#### a) Initial value $U^0$ - Time dependent approaches

There are several ways to make the convergence of a Newton procedure global. One dimensional searching of a corresponding optimization problem, for example, is proposed by Dennis and Schnabel [19] for this purpose. However for problems in fluid dynamics, a natural and robust way to get the initial approximation is the time-dependent approach, although as an iterative method it may be extremely slow. Following the true

physical process prevents the solution from non-physical states which may cause the procedure to stop, e.g., when the density becomes negative. The time-dependent marching is switched to the sparse quasi-Newton iteration as soon as the solution goes into a convergent region. Because the theory appropriate to the convergent region for the sparse quasi-Newton method is unavailable, this switching point has to be determined by experimentation to achieve the fastest convergence rate.

b) Initial approximation  $A^0$  to the Jacobian – Sparse finite difference Newton method

If in the above initialization procedure, an explicit time differencing is used, the initial approximation  $A^0$  to the Jacobian  $J(U^0)$  is evaluated by a sparse finite difference Newton method to start the sparse quasi-Newton procedure. While if an implicit time differencing is used in the initialization, the implicit operator can be used for the initial  $A^0$ . The latter approach is simpler, but, if the implicit operator is far removed from  $J(U^0)$ , the convergence may be greatly degraded. Since implicit methods are used in the following calculations for initialization, both approaches are tested for comparison.

### 3.5.3 Formulation for Three-Point and Five-Point Schemes

In the last section, the general formulation and application procedure are discussed. Here it is formulated for three-point and five-point schemes not only for their practical importance but also to provide a clear presentation of the application of the sparse quasi-Newton method and the sparse finite difference Newton method.

Suppose the steady state problem has been discretized by a three-point or five-point finite difference scheme in space. Introduce the notation

$$U = \begin{bmatrix} u_1 \\ u_2 \\ \cdot \\ \cdot \\ \cdot \\ u_I \end{bmatrix}, \quad R = \begin{bmatrix} r_1 \\ r_2 \\ \cdot \\ \cdot \\ \cdot \\ r_I \end{bmatrix}, \quad S = \begin{bmatrix} s_1 \\ s_2 \\ \cdot \\ \cdot \\ \cdot \\ s_I \end{bmatrix}, \quad (3-84)$$



for three-point scheme

$$d_{ii} = [ (s_{i-1})^T(s_{i-1}) + (s_i)^T(s_i) + (s_{i+1})^T(s_{i+1}) ]$$

for five-point scheme

$$d_{ii} = [(s_{i-2})^T(s_{i-2}) + (s_{i-1})^T(s_{i-1}) + (s_i)^T(s_i) + (s_{i+1})^T(s_{i+1}) + (s_{i+2})^T(s_{i+2})]$$

where  $s_{-1}, s_0, s_{I+1}$  and  $s_{I+2}$  are equal to zero.

2) Update  $A^k$  to  $A^{k+1}$  by

$$\begin{aligned} D^{k+1}_i &= D^k_i - d_{ii} r^{k+1}_i (s^k_i)^T & i=1, \dots, I, \\ B^{k+1}_i &= B^k_i - d_{ii} r^{k+1}_i (s^k_{i-1})^T & i=2, \dots, I, \\ C^{k+1}_i &= C^k_i - d_{ii} r^{k+1}_i (s^k_{i+1})^T & i=1, \dots, I-1, \end{aligned} \quad (3-86)$$

and for five-point scheme add

$$\begin{aligned} B^{k+1}_i &= B^k_i - d_{ii} r^{k+1}_i (s^k_{i-2})^T & i=3, \dots, I, \\ C^{k+1}_i &= C^k_i - d_{ii} r^{k+1}_i (s^k_{i+2})^T & i=1, \dots, I-2. \end{aligned}$$

### 3.5.3.2 Block tridiagonal and pentadiagonal FD Newton method

In the sparse finite difference Newton method, one only needs  $3 \times m$  or  $5 \times m$  additional evaluations of  $R(U)$  for a finite difference approximation of  $J(U)$  for block tridiagonal or pentadiagonal sparsity patterns respectively.

For the block tridiagonal case, this approximation can be evaluated by

$$\begin{aligned} (D_i) \cdot_n &= [r_i(u_{i-1}, u_i + h^n e^n, u_{i+1}) - r_i(u_{i-1}, u_i, u_{i+1})] / h^n_i, \\ (B_i) \cdot_n &= [r_i(u_{i-1} + h^n e^n, u_i, u_{i+1}) - r_i(u_{i-1}, u_i, u_{i+1})] / h^n_{i-1}, \\ (C_i) \cdot_n &= [r_i(u_{i-1}, u_i, u_{i+1} + h^n e^n) - r_i(u_{i-1}, u_i, u_{i+1})] / h^n_{i+1}, \end{aligned} \quad (3-87)$$

where  $e^n \in \mathbb{R}^m$  is a vector whose  $n$ th element is 1 and all the other elements are zero.  $h$  is chosen according to the machine zero.

It is clear that the calculation of  $r_i(u_{i-1}, u_i + h^n e^n, u_{i+1})$ ,  $r_i(u_{i-1} + h^n e^n, u_i, u_{i+1})$ ,  $r_i(u_{i-1}, u_i, u_{i+1} + h^n e^n)$  only needs  $3 \times m$  evaluations of  $R(U)$ . Similarly one can derive formulas for a block pentadiagonal structure, which needs  $5 \times m$  evaluations of  $R(U)$ .

In computations, boundary conditions should be embedded into the above formulation according to  $R(U)$ .

### 3.5.4 Application to Flux-Splitting and TVD Schemes for a Nozzle Problem

In this section a nozzle problem is chosen and two high shock-resolution finite difference discretization schemes are used to demonstrate the detailed procedure to apply the present method to existing robust discretization schemes. A comparison of the sparse quasi-Newton method with the original implicit procedures is given. The sparse quasi-Newton method is also compared with the sparse finite difference Newton method. The influence on convergence by using different initial Jacobians for the sparse quasi-Newton procedure is studied.

#### 3.5.4.1 The test problem

The governing equation for the nozzle problem [26] can be written as

$$\frac{\partial F(u)}{\partial x} + H(u) = 0 \quad (3-88)$$

with

$$u = \begin{bmatrix} \rho \kappa \\ m \kappa \\ e \kappa \end{bmatrix}, \quad F = \begin{bmatrix} m \kappa \\ (m^2 / \rho + p) \kappa \\ (e + p) m \kappa / p \end{bmatrix}, \quad H = \begin{bmatrix} 0 \\ -p(\partial \kappa / \partial x) \\ 0 \end{bmatrix}, \quad (3-89)$$

with  $\kappa$ , the area of the nozzle, a function of  $x$

$$\kappa(x) = 1.398 + 0.374 \tanh(0.8x - 4). \quad (3-90)$$

Here  $u$  is the vector of conservative variables,  $F$  is the flux vector, and  $m = \rho v$ . The primitive variables are the density  $\rho$ , the velocity  $v$  and the pressure  $p$ . The pressure  $p$  for a perfect gas is defined as

$$p = (\gamma - 1)(e - m^2/2\rho) \quad (3-91)$$

where  $\gamma$  is the ratio of specific heats.

In all the calculations the computational domain was  $0 \leq x \leq 10$ . The spacing of  $\Delta x = 0.5$  is used. The initial and boundary conditions are treated as in Yee et al [26].

#### 3.5.4.2 Time dependent approach – backward Euler implicit operator

Use a backward Euler differencing in time, the implicit scheme can be written as

$$[ (I/\Delta t) - M^k ] (U^{k+1} - U^k) = R(U^k), \quad (3-92)$$

which can reduce to the Newton method as  $\Delta t \rightarrow 0$  if the linearization is exact, i.e. if  $M = J = \partial R/\partial U$ . Therefore it provides a possibility for quadratic convergence.

The convergence is monitored by the maximum residuals

$$RES = \max ( |r_i^l| / |u_i^l| ) \quad (3-93)$$

and the time step with the implicit operator is

$$\Delta t^k = \epsilon / RES^k, \quad (3-94)$$

where  $\epsilon$  is a positive number to control the initial transient. The implicit operators used below are of this evolution/relaxation type with  $\Delta t \rightarrow \infty$  as  $RES \rightarrow 0$ .

### 3.5.4.3 Van Leer's flux vector splitting

a) First order accuracy

A flux vector splitting spatial differencing method [23, 24] is used to solve Eq. (3-88). The resulting nonlinear system can be written as

$$r_i = r_i(u_{i-1}, u_i, u_{i+1}) = -(F_i^+ - F_{i-1}^+ + F_{i+1}^- - F_i^-)/\Delta x - H_i = 0, \quad (3-95)$$

where  $F^+$ ,  $F^-$  are defined in the same way as in [23]. This flux-splitting scheme has the advantage that the split fluxes  $F^+$ ,  $F^-$  are continuously differentiable and an analytic expression of the Jacobian for this problem can easily be derived.

*Implicit operator.* After the exact linearization of the implicit backward Euler time differencing the implicit operator can be written as

$$\begin{aligned} D_i &= I/\Delta t + (E_i^+ - E_i^-)/\Delta x - G_i, \\ B_i &= -E_{i-1}^+/\Delta x, \\ C_i &= -E_{i+1}^-/\Delta x. \end{aligned} \quad (3-96)$$

where  $E^+$  and  $E^-$  represent  $\partial F^+/\partial u$  and  $\partial F^-/\partial u$ . Corresponding to the explicit boundary conditions, the implicit boundary treatment is

$$\begin{aligned} \bar{D}_{I-1} &= D_{I-1} + (2/\Delta x)E_{I-1}^- I_1, \\ \bar{B}_{I-1} &= B_{I-1} - (1/\Delta x)E_{I-1}^- I_1, \end{aligned} \quad (3-97)$$

where

$$I_1 = \begin{bmatrix} 0 & & \\ & 1 & \\ & & 1 \end{bmatrix}.$$

This correspondence on the boundary is important for the implicit operator. Otherwise the implicit operator will not reduce to the Jacobian as  $\Delta t \rightarrow \infty$ .

*Sparse quasi-Newton method.* In the sparse quasi-Newton method, formulas in (3-86) are used to update approximations  $D^k$ ,  $B^k$ ,  $C^k$  to  $D^{k+1}$ ,  $B^{k+1}$ ,  $C^{k+1}$ . Note that no special treatment on the boundary is needed.

Fig. 3.6 shows the convergence histories against the iteration number and the work unit respectively. Here one work unit is defined as the CPU time per iteration needed for the corresponding implicit method. As shown in Figs. 3.6(b) and 3.6(c) the sparse quasi-Newton approach has almost the same efficiency as a Newton approach. The FD Newton method can achieve the same convergence as achieved by a Newton method if the increments are properly chosen according to the machine zero and  $R(U)$ .

b) Second order accuracy - MUSCL approach

The MUSCL approach is used for a second order flux vector splitting scheme

$$r_i = r_i(u_{i-2}, u_{i-1}, u_i, u_{i+1}, u_{i+2}) \\ = -[F^+(u_{i+1/2}^-) - F^+(u_{i-1/2}^-) + F^-(u_{i+1/2}^+) - F^-(u_{i-1/2}^+)] / \Delta x - H(u_i) \quad (3-98)$$

where  $u^-$  and  $u^+$  are defined similarly as in [49].

*Implicit operator.* The implicit operator is the same as the first order case, which does not affect the accuracy of the right hand side but prevents the method from reducing to a Newton method as in the first order case.

*Sparse quasi-Newton method.* Since the scheme is a five-point scheme, the block pentadiagonal quasi-Newton update is used.

Fig. 3.7 shows the result for the second order case. As expected the convergence by the implicit operator is heavily degraded compared to the first order case, while the sparse quasi-Newton approach still exhibits a high convergence rate as compared to the FD Newton method. Although the FD Newton method has a slightly higher convergence rate (shown in Fig. 3.7(b)), the sparse quasi-Newton with the FD Newton

method evaluating the initial Jacobian is the most efficient (shown in Fig. 3.7(c)) as far as CPU time is concerned.

#### 3.5.4.4 Harten's TVD scheme

If a first or second order accurate (in space) TVD scheme [25, 26] is used in the discretization, the resulting non-linear system may be written as

$$r_i = - (1/\Delta x)(\tilde{F}_{i+1/2} - \tilde{F}_{i-1/2}) - H_i = 0, \quad (3-99)$$

where

$$\tilde{F}_{i+1/2} = \frac{1}{2} (F_i + F_{i+1}) + \frac{1}{2} \Sigma [g_i^1 + g_{i+1/2}^1 - Q(a_{i+1/2}^1 + \gamma_{i+1/2}^1) \alpha_{i+1/2}^1] P_{i+1/2}^1$$

and

$$g_i^1 = S \max [0, \min(\sigma_{i+1/2}^1 |\alpha_{i+1/2}^1|, S \sigma_{i-1/2}^1 \alpha_{i-1/2}^1)],$$

$$S = \text{sign} (\alpha_{i+1/2}^1),$$

$$\gamma_{i+1/2}^1 = \begin{cases} (g_{i+1}^1 - g_i^1) / \alpha_{i+1/2}^1, & \alpha_{i+1/2}^1 \neq 0, \\ 0, & \alpha_{i+1/2}^1 = 0, \end{cases}$$

$$\sigma_{i+1/2}^1 = \sigma(a_{i+1/2}^1),$$

$$\sigma(z) = \frac{1}{2} Q(z) \text{ and}$$

$$Q(z) = \begin{cases} \frac{1}{2} \left( \frac{z^2}{\delta} + \delta \right), & |z| < \delta, \\ |z|, & |z| \geq \delta. \end{cases}$$

*Implicit operator.* To accelerate convergence to steady state, Harten [25] extended his explicit TVD scheme to an implicit method by a so-called TVD linearization. The resulting implicit operator can be written as

$$\begin{aligned} D_i &= (1/\Delta t)I + (1/\Delta x)(\tilde{E}_{i+1/2}^- + \tilde{E}_{i-1/2}^+) - G_i, \\ B_i &= (1/\Delta x) \tilde{E}_{i-1/2}^+, \\ C_i &= -(1/\Delta x) \tilde{E}_{i-1/2}^-, \end{aligned} \quad (3-100)$$

where

$$E_{i+1/2}^{\pm} = P_{i+1/2} \text{diag} [C^{\pm}(a^{1+\gamma})_{i+1/2}] (P^{-1})_{i+1/2},$$

$$C^{\pm}(z) = (1/2) [ Q(z) \pm z ]$$

and  $P$  is the matrix which consists of the right eigenvectors of  $\partial F/\partial U$ , i.e.,  $P = (P^1, P^2, P^3)$ . At the downstream boundary  $B_I$  and  $D_I$  are modified as in (3-97).

This "TVD linearization" is clearly not an exact linearization of  $R(U)$ . Hence the implicit operator will not reduce to a Newton iteration method as  $\Delta t \rightarrow \infty$ .

*Sparse quasi-Newton approach.* The above scheme is a five-point second order accurate (in space) scheme. Therefore the five point sparse quasi-Newton method formulated Sec. 3.5.3 is used.

To get the three-point first order accurate TVD scheme, simply set  $g = \gamma = 0$  in the above second order form.

Figs. 3.8 and 3.9 show the results for first and second order TVD scheme respectively. The convergent rate is improved greatly and the CPU time is reduced marginally by the sparse quasi-Newton approach.

#### 3.5.4.5 Analysis of convergence and efficiency

A detailed analysis of the CPU time has revealed that:

a) In the first order cases the implicit operator needs more CPU time per iteration than the sparse quasi-Newton method;

b) In the second order cases the sparse quasi-Newton method spends almost the same CPU time as the implicit method per iteration though the block pentadiagonal matrix is more expensive to invert than the block tridiagonal matrix;

c) The sparse FD Newton method has the fastest convergence rate but spends much more time per iteration due to many times of functional evaluation, so its efficiency is outperformed by the sparse quasi-Newton method;

d) Using sparse FD Newton method for the initial Jacobian approximation gives better results than directly using the implicit operator for this purpose.

### 3.6 Concluding Remarks

In this chapter, two implicit schemes were developed for steady state solutions of the locally conical Navier–Stokes equations. In the implicit schemes the source term was treated explicitly based on Fourier stability analysis. For the MacCormack implicit scheme, the implicit boundary conditions were treated according to the explicit boundary conditions, which was found to be more robust in the computation than the implicit boundary treatment proposed in MacCormack's original paper.

Both of the implicit schemes showed much higher convergence rate than the MacCormack explicit method for the steady state N–S solution. While comparison of the two implicit schemes revealed that the simplified Beam–Warming implicit scheme spends substantially more time per time step than that of the MacCormack implicit scheme. On the other hand, it was found that the simplified Beam–Warming scheme can generally use larger time steps.

Analysis of both a model problem and numerical results indicated that the accuracy of steady state solutions using MacCormack–type schemes will be influenced by time step size. However, it was found that accuracy of steady state solution using the MacCormack implicit scheme can be achieved by reducing the time step successively towards the end of convergence until the variation of the solution with the time step size disappears. A similar analysis of the Beam–Warming schemes revealed a time step independence of steady state solutions due to the spatial discretization is separated from the time discretization in the formulation. Nearly identical results of such crucial parameters as heat transfer rates with the two implicit schemes were obtained.

Two multigrid schemes were found to be able to accelerate the convergence of the two implicit schemes further to the steady state, as achieved previously in acceleration of explicit schemes.

A sparse quasi-Newton scheme was proposed in order to avoid the difficulties in the linearization needed in implicit schemes and to achieve fast convergence to steady states. The rapid local convergence of the scheme was combined with the robustness of the time marching scheme to obtain a globally convergent procedure. The simplicity and generality of this procedure suggests its use as an efficient tool for fast steady state solutions in CFD.

Preliminary results were presented for high resolution schemes to solve a one dimensional nozzle problem. Due to the sophistication of high resolution schemes, exact linearization in the implicit procedures is usually very difficult. Therefore simplification was introduced in the corresponding implicit schemes. For example, a first order implicit operator was used in the second order van Leer's flux splitting scheme and a TVD linearization was used in the Harten's implicit TVD scheme. The sparse quasi-Newton method gave significantly faster steady state solutions as compared to the implicit operators of van Leer and Harten.

## CHAPTER FOUR

### HYPERSONIC FLOW SIMULATIONS

#### 4.1 Introduction

A major step towards understanding the flow over general hypersonic vehicle shapes can be made by numerically predicting the flow over simplified yet representative shapes. Cones, delta wings and their combinations are such shapes which exhibit their usefulness in the forebody and wing design for high speed flight vehicles.

Owing to their practical importance, cones and delta wings were extensively studied in the past both experimentally and numerically in supersonic flows. However, due to the complexity of the flowfields, especially on the leeward side at high angles of attack where strong viscous/inviscid interactions take place, the understanding of the flow behaviour is still far from satisfactory. Furthermore, hypersonic flows introduce new flow phenomena and new problems. It was believed that further study of these shapes in the hypersonic regime can contribute to the basic insight of hypersonic flow behaviour for more general hypersonic vehicles.

A cone-and-delta-wing combination provides the simplest case for investigating wing-body interference in hypersonic flows. Some experimental investigations were done in the 60's [29-31]. Unfortunately, the experimental data are not of high accuracy due to the difficulties encountered in hypersonic experimentation. Only surface measurements were made and large scatter appeared in the data near the junction where the interaction is strong. Furthermore, knowledge of just surface data is not sufficient for understanding the flow and misinterpreting of the surface data is not unusual.

In this chapter, numerical simulations carried out on hypersonic flows around such conical shapes as cones, delta wings and cone-and-delta-wing combinations are presented. Validation of the codes was achieved by comparing the numerical results with the limited experimental data available.

For the cone-and-delta-wing combination, the author's first numerical simulation [32] provides details of the flowfield and explains the complex flow behaviour on the vehicle surface. The "possible" pictures given by the experimentalists are justified or modified.

To explore the leeward side of the combination, where neither experimental nor computational investigations had been carried out, numerical simulation by the present codes was implemented to investigate the resultant phenomena [33].

Numerical solution of the conical Euler equations was also made to illustrate, by comparing with LCNS solutions, the importance of including the viscous effects.

## 4.2 Hypersonic Flow around Cones

Experimental data indicate that at high angle of attack, the flow on the leeward side of a cone separates in a circumferential mode and forms counter-rotating longitudinal vortices. In addition to the bow shock around the cone, embedded shocks terminating the supersonic crossflow over the cone were also observed in the experiments under certain conditions. This complex flow structure clearly necessitates a N-S solution for representative simulations.

### 4.2.1 Computational Conditions

A well-documented experimental investigation was carried out by Tracy [27]. The present cone computation was carried out under his experimental conditions to enable validation of the code.

Table 4.1 Conditions for cone flow simulation

cone half angle	$\theta_c$	$10^\circ$
free stream Mach number	$M_\infty$	7.95
free stream temperature	$T_\infty$	55.4 K
wall temperature	$T_w$	309.8 K
total temperature	$T_0$	755.6 K
computation station	$r$	0.1 m ( 4 in )
characteristic Reynolds number	$Re_{\infty, r}$	$4.2 \times 10^5$
Prandtl number	$Pr$	0.72
angle of attack	$\alpha$	$0^\circ, 4^\circ, 8^\circ, 12^\circ, 20^\circ, 24^\circ$

The geometry and the solution surface are illustrated in Fig. 4.1. Fig. 4.2 shows the mesh system, where a mesh from  $65 \times 3$  for  $\alpha = 0^\circ$  to  $65 \times 65$  for  $\alpha = 24^\circ$  is stretched in the  $\theta$  direction so that a very fine grid is achieved near the wall in order to resolve the viscous effects. The mesh in the  $\varphi$  direction is evenly distributed for the cone case. A symmetry boundary condition mentioned in Sec. 2.6 is applied on the two lines at  $\varphi = 0^\circ$  and  $\varphi = 180^\circ$  so that only half of the whole flow field needs to be computed. On the wall the no-slip boundary condition is used. The wall is isothermal and the temperature is set to the given value  $T_w$ .

As has been mentioned in Sec. 2.6, the flow field is computationally initialized by setting it to the flow condition at infinity. If the incoming flow and the spherical coordinates are related in such a way as shown in Fig. 4.1 for the cone case simulation, the initial and the outer boundary conditions can be expressed as

$$\begin{aligned}
 \rho_\infty &= 1, \\
 u_{r\infty} &= \cos\alpha \cos\theta - \sin\alpha \cos\varphi \sin\theta, \\
 u_{\theta\infty} &= -\cos\alpha \sin\theta - \sin\alpha \cos\varphi \cos\theta, \\
 u_{\varphi\infty} &= \sin\alpha \sin\varphi, \\
 e_\infty &= \frac{1}{\gamma(\gamma-1)M_\infty^2} + \frac{1}{2}.
 \end{aligned} \tag{4-1}$$

#### 4.2.2 Flow Field Simulation

Flow field simulations were done for an angle of attack range from  $\alpha = 0^\circ$  to  $\alpha = 24^\circ$ . At lower angles of attack the viscous/inviscid interaction is not strong and the flow field is characterized by a bow shock wave around the cone and a boundary layer fully attached on the cone surface. The case at  $\alpha = 0^\circ$  is a special case where the modelling is reduced to a one dimensional problem because the variation in the  $\varphi$  direction vanishes. The two implicit schemes and their multigrid accelerations were all first tested on this case before going to more complicated situations. This cone case at zero angle of attack provides a simple test model for the N-S codes since both a shear layer and a strong shock wave are involved.

The more interesting and complex cases are at high angles of attack. The unfavourable crossflow pressure gradient on the leeward side of the cone separates the boundary layer and the shear layers rotate into two vortices on both sides of the leeward symmetry plane. Two simulation cases,  $\alpha = 12^\circ$  and  $\alpha = 24^\circ$  are selected to demonstrate the flowfield and the results are shown in Figs. 4.3 to 4.5.

Figs. 4.3(a) and 4.4(a) show the cross flow velocity vectors in which both their direction and magnitude are given. General pictures of the flow field are given by the simulation illustrating such major features as the bow shock waves, the flow separations and the vortices. Also plotted in these figures are the experimental data on the positions of the bow shock waves and the separation points. A closer look at the separation point and the vortex flow is given in Figs 4.3(b) and 4.4(b).

The pressure and density contours in Figs. 4.3(c),(d) and 4.4(c),(d) give a clear picture of the bow shock wave. The embedded shock can also be detected from the contours in the  $\alpha = 24^\circ$  case. This is actually a fairly mild shock and, thus, appears in the computed results only as relatively small changes in pressure and density compared to the strong bow shock.

The computed surface pressure is plotted in Fig. 4.5 compared with experimental measurements. Good agreement is observed, although the computed pressures on the windward side are slightly lower than those measured experimentally. The same tendency has been observed in previous calculations of these cases [35] and is generally attributed to experimental pressure taps that were large in relation to the windward boundary layer thickness.

### 4.3 Hypersonic Flow on the Leaside of Delta Wings

Delta wings are clearly quite common wing shapes for high speed atmospheric flight vehicles. A classification of the flow phenomena was first given by Stanbrook and Squire [58]. They divide the types of flow by means of a boundary defined around the normal Mach number  $M_N = 1$ , which separates the flows with leading edge separated vortices from those with a shock attached at the leading edge.

The classification of the flow was further enriched by Miller and Wood [59] based on experimental investigations at supersonic speeds. From pictures derived from various flow visualization techniques the flow is divided further into seven types representing seven different flow phenomena. This is illustrated on the left half of Fig. 4.13.

Lack of information in the hypersonic regime makes the flow behaviour in this regime unclear, which motivated the present simulation. The numerical codes developed in the last chapter provide this opportunity. With extensive numerical simulations the classification may eventually be extended to the hypersonic regime.

#### 4.3.1 Computational Conditions

The numerical simulation carried out here is under the conditions corresponding to the experimental work carried out by Cross [28], as shown in Table 4.2.

Table 4.2 Delta wing flow simulation conditions

delta wing sweep back angle	$\Lambda$	$75^\circ$
free stream Mach number	$M_\infty$	10.17
free stream temperature	$T_\infty$	45.6 K
wall temperature	$T_w$	699.5 K
total temperature	$T_0$	989 K
computation station	$r$	0.14 m
characteristic Reynolds number	$Re_{\infty, r}$	$2.4 \times 10^6$
Prandtl number	$Pr$	0.72
gas constant	$\gamma$	1.4
angle of attack	$\alpha$	$0^\circ, 5^\circ, 9^\circ, 11^\circ, 15^\circ$

The normal angle of attack, i.e. the angle of attack normal to the leading edge, and the normal Mach number, i.e. the component of Mach number normal to the leading edge are defined by

$$\alpha_N = \operatorname{tg}^{-1} \frac{\operatorname{tg} \alpha}{\cos \Lambda}, \quad M_N = M_\infty (1 - \cos^2 \alpha \sin^2 \Lambda)^{\frac{1}{2}}. \quad (4-2)$$

Under the present conditions the variation of  $\alpha_N$  and  $M_N$  against  $\alpha$  is listed in the Table 4.3.

Table 4.3 Variation of  $\alpha_N$  and  $M_N$  against  $\alpha$  at  $M_\infty = 10.17$  and  $\Lambda = 75^\circ$

$\alpha$	$0^\circ$	$5^\circ$	$9^\circ$	$11^\circ$	$15^\circ$
$\alpha_N$	$0^\circ$	$18.7^\circ$	$31.5^\circ$	$36.9^\circ$	$46.0^\circ$
$M_N$	2.6	2.8	3.0	3.2	3.7

Due to the very high Mach number in the present case, the points ( $\alpha_N$ ,  $M_N$ ) are all outside the classification chart given by Miller and Wood [59], where the maximum  $M_N$  is 2.

The computational surface and the geometry are related as shown in Fig. 4.6. The mesh system is shown in Fig. 4.7. The mesh is stretched in both directions. In the  $\theta$  direction the mesh is stretched to obtain a fine grid near the wall and in the  $\varphi$  direction the mesh is stretched to obtain a fine grid around the leading edge to avoid overexpansion. The symmetry boundary,  $\varphi = 0^\circ$ , halves the computational domain. The wall boundary condition is applied on the wing surface at  $\theta = 90^\circ$  ( $0^\circ \leq \varphi \leq 90^\circ - \Lambda$ ). The outer boundary condition and the initial condition are given as

$$\begin{aligned}
 \rho_\infty &= 1, \\
 u_{r,\infty} &= -\sin\alpha \cos\theta + \cos\alpha \cos\varphi \sin\theta, \\
 u_{\theta,\infty} &= \sin\alpha \sin\theta + \cos\alpha \cos\varphi \cos\theta, \\
 u_{\varphi,\infty} &= -\cos\alpha \sin\varphi, \\
 e_\infty &= \frac{1}{\gamma(\gamma-1)M_\infty^2} + \frac{1}{2}.
 \end{aligned}
 \tag{4-3}$$

### 4.3.2 Flow Field Simulation

Crossflow velocity vectors are plotted in Figs. 4.8(a)–4.12(a). Details near the symmetry plane are shown in Figs. 4.8(b)–4.12(b)

Crossflow Mach number and density contours in Figs. 4.8(c), (d) – 4.12(c), (d) clearly indicate the shock wave attached to the wing leading edge, the shear layer lifting off from the inboard of the wing surface.

At  $\alpha = 0^\circ$  the flow field is characterized by a bow shock wave and the boundary layer remains attached to the wing surface. No embedded shock is observed in both the present numerical simulation and the experimental investigation, while it may occur in the lower Mach number range as indicated in Miller and Wood's classification.

Particularly of note is the embedded shock wave above the shear layer shown in  $\alpha = 5^\circ$ ,  $\alpha = 9^\circ$ ,  $\alpha = 11^\circ$  and  $\alpha = 15^\circ$  cases. This embedded shock wave was clearly observed in the experimental investigation in the latter three cases. It strongly interacts with the wing boundary layer resulting in the separation on the wing surface.

Miller and Wood's classification is illustrated on the left half of Fig. 4.13. Data points from the present simulation are plotted in the  $(\alpha_N, M_N)$  chart and are shown to lie outside the scope of the Miller–Wood classification. The flow phenomena corresponding to different angles of attack for the present simulation are also illustrated. It is clear that the two straight lines in the Miller–Wood classification cannot be extended to the hypersonic regime on the right half of Fig. 4.13 because phenomena such as a leading edge separation bubble combined with a shock wave and an embedded shock along with no separation were not observed in the present hypersonic simulation. This is in agreement with the experimental investigation carried out by Cross [28].

The above observation indicates that hypersonic flow around delta wing exhibits some different features from those in the lower speed range. Extensive numerical simulations could provide a valuable classification of types of delta wing flow in the hypersonic regime.

#### 4.4 Hypersonic Flow beneath/over Cone–Delta–Wing Combinations

In early studies it had been expected that the interference effects on the windward side of a wing–body combination in high speed flows would favour lifting effectiveness. Lack of knowledge of the shock–shock and shock–boundary layer interactions associated with it and difficulties in predicting the resultant separation, vortex flow and reattachment, however, did not allow the full exploitation of this benefit. On the other hand undesirable high local heating peaks were generated as a result of these interactions.

Attempts made two decades ago to understand these complicated flows involved surface measurement in supersonic and hypersonic flow beneath such simple geometries [29–31]. The small scale of experiments and the large scatter in the data, however, was so as to make it difficult to predict accurately, especially near the wing–body junction, the details of the surface pressure signature due to the vortex flows generated by the interactions and the resultant high local wall heating rates.

To understanding the behaviour of this complex flow field, numerical experiments were carried out using the present computer simulation.

##### 4.4.1 Computational Conditions

The cone–delta–wing configuration tested experimentally by Meyer and Vail[29] is chosen. Fig. 4.14 shows the sketch of the geometry and the solution surface. The flow conditions are listed in the following table.

Table 4.4 Flow conditions for cone-delta-wing combination simulation

cone half angle	$\theta_c$	12°
delta wing sweep back angle	$\Lambda$	60°
free stream Mach number	$M_\infty$	12.65
total temperature	$T_0$	1800 K
free stream temperature	$T_\infty$	54.54 K
wall temperature	$T_w$	288 K
computation station	$r$	94 mm
characteristic Reynolds number	$Re_{\infty, r}$	$3.78 \times 10^5$
Prandtl number	$Pr$	0.72
Angle of attack	$\alpha$	-10°*, -5°*, 0°, 5°, 15°

\* The minus degree corresponds to the leeward side flow simulation.  
No experimental data exist for these two cases.

The mesh of 65×65, illustrated in Fig. 4.15, is stretched in both  $\theta$  and  $\varphi$  directions in such a way as to ensure sufficient resolution of the viscous effects. The initial flow field is set to the flow properties at infinity. The expression is the same as in Eq. (4-1) for the cone case.

The boundary conditions supplied are

- a) on the wall:  $u = v = w = 0$ ;  $T = T_w = \text{constant}$  (isothermal wall)
- b) outer boundary: free stream values
- c) symmetric plane: reflection condition

For the conical Euler solutions the wall no-slip boundary condition a) is replaced by tangency condition with  $v = 0$  on the cone surface and  $w = 0$  on the wing surface.

#### 4.4.2 Windward Side Flow Field Simulations

##### 1) Angle of attack $\alpha = 0^\circ$

According to inviscid flow theory, flow at zero angle of attack is quite simple. In this case the free stream is aligned with the surface of the wing so no shock wave is generated by the wing. Part of the wing captures the high positive pressure of the cone shock layer and this so-called "inviscid interference pressure" produces an interference lift on the wing.

Unfortunately this is not the case in practice. Viscous effects complicate the flow field. Figs. 4.16(a)–(f) show the numerical results for this case. Fig. 4.16(a) presents the crossflow velocity vectors at each grid point and Fig. 4.16(b) gives a closer view near the junction. Figs. 4.16(c) and (d) show the crossflow Mach number and pressure contours. Figs. 4.16(e) and (f) compare the surface pressure and heat transfer with the experimental data respectively.

The high pressure field of the cone shock layer interacts with the wing boundary layer, which results in separation on the wing. This is the major feature of the flow interaction, which is clearly shown in Figs. 4.16(a)–(d). The separated flow from the wing forms a very strong vortex, which reattaches first on the cone surface at  $A_1$  and then on the wing surface at  $A_2$ . Flow reattachment creates high local heating rates on the surface as seen in Fig. 4.16(f). A secondary vortex between the wing and the

primary vortex is easily observed with reattachment at  $A_3$ . The thick viscous layer beneath the wing interacts with the oncoming flow and a weak shock wave forms from the wing leading edge. The outer edge of the viscous layer and the weak shock wave are clearly illustrated in Fig. 4.16(c). This weak shock wave again interacts with the cone shock wave and a resulting strong internal shock wave appears clearly outside the primary vortex to decelerate further the high speed flow passing through the weak wing shock and deflecting it into the primary vortex. The internal shock curves inwards because of the influence of the wall as shown in Figs. 4.16(c) and (d). A shear layer resulting from the slip surface is seen lying between the shock-shock interaction point and the reattachment point  $A_1$  in Fig. 4.16(c), which divides the flow processed by the cone shock from that by the wing shock.

With the flow field pictures in mind, the surface pressure distribution and the heat transfer to the wall become understandable. Comparison with the data of Meyer and Vail's surface pressure measurement is made in Fig. 4.16(e). The pressure spike at  $A_1$  predicted by the numerical results aligns qualitatively with measurements at zero angle of attack as reported in [31]. Unfortunately Meyer and Vail[29] failed to give data in this region due to difficulties in measurement near the junction.

As shown in Fig. 4.16(f) the peaks in heat transfer correspond to the reattachment points,  $A_1$ ,  $A_2$  and  $A_3$  while the valleys to the separation points,  $S_1$ ,  $S_2$ . Quite good agreement with the experimental data has been observed in this case. Also observed is the good agreement with the two different codes, which gives the author confidence for the numerical simulation.

## 2) Angle of attack $\alpha = 5^\circ$

Figs. 4.17(a)–(f) illustrate the results of the numerical simulation of the case at an angle of attack of  $5^\circ$  using the same set of illustrations as for the  $\alpha = 0^\circ$  case. At this small angle of attack, a number of its features as described for zero angle of attack are seen, but the effects on the surface parameters on the wing are more accentuated due to the interaction being more directed towards the wing. In the crossflow Mach contour, Fig. 4.17(c), the "three-shock configuration" is well represented and instead of a slip surface the shear layer between the shock-shock interaction point and the reattachment point  $A_1$  is clearly seen. The shock resulting from the shock-shock interaction further interacts with the wing boundary layer and another internal shock emerges close to the junction due to influence of the wall. This internal shock directs the strong crossflow to roll through the junction into a strong primary vortex beneath the wing.

Significant is the appearance of a vortex rolling up from the cone surface, which is not seen in the zero angle of attack case. This vortex is seen more prominently in the  $\alpha = 15^\circ$  case to be described. It is seen from Fig. 4.17(e) that the predictions of the surface pressure distribution agree well with the measurements of Meyer and Vail[29]. In Fig. 4.17(f) the heat transfer distribution agrees reasonably well with the experimental measurements in identifying the peaks and the valleys but the level is lower than the experimental data on the cone surface. At this stage this discrepancy is not understood. Communication of the work at an International meeting [32] did reveal from a colleague of the authors of this 1967 experimental study [29] that measured heat transfer results were higher than empirical results would show at the higher angle of attack cases, but this observation remains unsubstantiated.

### 3) Angle of attack $\alpha = 15^\circ$

Figs. 4.18(a)–(f) have an equivalent sequence as in the  $\alpha = 0^\circ$  and  $5^\circ$  cases. Figs. 4.18(a) and (c) show crossflow features of the flowfield. At this high incidence, the flow structure is clearly different from those at zero and  $5^\circ$  angle of attack cases. From the crossflow velocity vector plot, Figs. 4.18(a) and (b), there is observed a narrow separation region beneath the wing and the high energy flow reattaches on the wing first instead of on the cone as in the previous cases. The main stream of this flow passes through the corner then reattaches on the cone surface. It meets the cone boundary layer and rolls up into a vortex. When the high energy flow passes through the corner, a small part of it divides and forms a small vortex near the junction. A secondary separation on the cone surface beneath the primary one can be identified in Figs. 4.18(b) and (c).

At this angle of attack, the wing shock wave becomes stronger and the difference in strength and intersection angle between the two shock waves is reduced. The two shock waves appear to merge into each other and the interaction only results in weak compression waves and a shear layer. The compression waves interact with the wing boundary, while the shear layer joins into the process of rolling up of the primary vortex.

The comparison of the wall pressure distribution is given in Fig. 4.18(e). The two high pressure peaks near the corner represent the two reattachment points of the high energy stream. Peaks in heat transfer distribution, Fig. 4.18(f), exhibit all the four reattachment points,  $A_1, A_2, A_3, A_4$ , on the wall, two on the wing and two on the cone surface, while the valleys in heat transfer distribution are associated with the separation points,  $S_1, S_2, S_3, S_4$ . These peaks and valleys are clearly results of the flow structure shown in Fig. 4.18(a)–(d). The discrepancy with experimental data appears larger in the level of heat transfer distribution at this higher angle of attack.

#### 4.4.3 Exploration of Leeward Side Interaction

The problem of leeward side heating in hypersonic streams was brought into prominence with the space shuttle programme one-and-a-half decades ago. Experience gained from the wind tunnel and flight tests associated with the NASA Space Shuttle development indicated that there can be significant localised heat transfer rates taking place on the leeward side of the vehicle due to flow reattachment.

With the confidence of the previous numerical simulations it is interesting to extrapolate our knowledge from the windward side to the leeward side around such a simple wing-body geometry. This will allow the leeward side wing-body interaction in hypersonic flow to be assessed. Special attention will be put on the high local heating problem. The leeside flow is simulated with the same code and conditions as the windward side simulation except for a negative input for the angle of attack.

Figs. 4.19(a)–(d) show the leeside flowfield at  $\alpha = 5^\circ$  derived from the computer simulation. It is interesting to compare these pictures with the delta wing case. Due to the existence of the upper cone body, the interaction is stronger at this low angle of attack than as seen in the delta wing leeside flow. The weak wing shock turns the body shock towards the cone surface and peak pressures and high local heating rates can be found at the resulting reattachment point as illustrated in Figs. 4.19(e) and (f). As stated earlier no experimental data exist for this case to compare with the prediction.

#### 4.4.4 Euler solutions

To illustrate the importance of viscous effects it is useful to compare the Navier–Stokes solution with the Euler solution. Figs. 4.20(a)–(d) show solution of the conical Euler

equations for the  $5^\circ$  angle of attack case. It is not surprising to find that no vortex exists in the inviscid solution. The delta wing shock layer is much thinner than that in the viscous solution due to the absence of the thick boundary layer. The three shock configuration is clearly shown with a resulting shock reflected on the wing surface. The totally different flow structures produced by Navier–Stokes solutions and Euler solutions indicate the strong viscous effects associated with this problem, and justifies use of the N–S equations.

#### 4.5 Concluding Remarks

Numerical simulations of hypersonic flow around a cone, above a delta wing and beneath/above a cone-delta-wing combination have been generated by solving the compressible Navier-Stokes equations using a "locally conical" assumption. Illustrations derived from these solutions and comparisons with surface measurements and conical Euler solutions have resulted in the following conclusions.

- 1) Numerical simulations can provide detailed information of the flow field and help understanding of the complex flow processes.
- 2) Various types of vortex flows resulting from the shock-shock, shock-vortex and shock-boundary layer interactions dominate the flow on the leeside of the cone, on the delta wing and both beneath and over the combination. The comparison of the results with those from a conical Euler analysis indicates further that the flow is strongly influenced by viscous effects.
- 3) For all three geometries, embedded or internal shocks were observed from the numerical simulation. For the cone and the delta wing, the embedded shocks seem to be a phenomenon associated with moderate to high angle of attack, while for the combination they are more evident at low incidence.
- 4) For the combination, surface pressure peaks near the junction are features at low angle of attack cases and very high aerodynamic heating rates were observed in all cases around the strong vortex reattachment points. Due to different interaction structures at different angles of attack, the flow behaviour appears quite sensitive to the angle of attack, showing large difference between results at  $0^\circ$  and  $15^\circ$  angles of attack.

5) Reasonable agreement with surface pressure measurements provides validity of the locally conical assumption and the numerical method. For the wing-body combination, computed heat transfer rates agree well with the experimental data at low incidence, while the discrepancy with the measurement in the level of heat transfer distribution at high angles of attack needs to be explained further in the light of difficulties in measurement at those conditions.

6) Almost identical results, even with the most crucial parameter — heat transfer, from the two different codes gives further confidence of the simulations.

7) The results give important guidance to designers of high speed vehicles concerning the complex nature of aerodynamic loading and heating on surfaces.

## CHAPTER FIVE

### CONCLUSIONS AND FUTURE WORK

Recently renewed interest in hypersonics necessitates a reliable, robust and efficient Navier–Stokes code for the understanding of the associated complex flow behaviour.

Research towards the development of numerical methods and flow simulations of hypersonic flow around representative space–plane shapes is reported in this thesis. The research is naturally divided into two parts, numerical and physical. Some conclusions are drawn from this research.

#### 5.1 Numerical Aspects

In the numerical part of the study, two basic implicit schemes were applied to solve the locally conical Navier–Stokes equations. Comparison of the efficiency and the accuracy of these two schemes were made in relation to the popular MacCormack explicit scheme. Further acceleration of these two implicit schemes was achieved by employing multigrid methods. In parallel to these studies, a totally new approach, the sparse quasi–Newton method, was proposed for fast steady state solutions. The following conclusions on numerical aspects are drawn from the research.

1) Compared to the MacCormack explicit scheme, both of the implicit schemes showed a much faster convergence to the steady state by taking much larger time steps. Therefore for Navier–Stokes solutions, where a highly stretched mesh is usually necessary, as in the present simulation, an implicit scheme is preferred to an explicit scheme.

2) For steady state solutions, all the MacCormack-type schemes, both explicit and implicit, have the disadvantage of a dependence of the steady state solution on the time step,  $\Delta t$ , used in the time marching. This is proved both from a model problem analysis and from the results of numerical simulations. On the other hand, the Beam-Warming-type implicit schemes, including the simplified version presented in this thesis, have the advantage that the steady state solution does not depend on the time step used in the time marching. This was also proved from both a model problem analysis and from the numerical results. The key reason behind this difference is that in the MacCormack-type schemes the time differencing and the spatial differencing is mixed while in the Beam-Warming-type schemes the time differencing and the spatial differencing is separated. However, it was found that accuracy of steady state solutions using the MacCormack implicit scheme can be achieved by reducing time step size successively towards the end of convergence until the variation of the solution on time step disappears. In this way, nearly identical results of such crucial parameters as heat transfer rates were obtained using the two different implicit schemes.

3) The simplified Beam-Warming scheme presented in the present thesis was found to need much more computing time per time step than the MacCormack implicit scheme. This is due to the fact that two block tridiagonal matrix inversions need to be done per time step in the simplified Beam-Warming scheme while, in the MacCormack implicit scheme, by making use of the decomposition of the inviscid Jacobians only four scalar bidiagonal systems need to be solved.

4) Multigrid methods can further accelerate implicit schemes. Although the Ni-type multigrid scheme is not originated from mathematical theory, it is efficient in propagating the waves with the help of the coarser grids. Treated as an iterative scheme for the steady state solution, the simplified Beam-Warming scheme can be further accelerated by a FAS multigrid procedure.

5) The proposed sparse quasi-Newton approach provides a new and very promising direction for fast steady state solution. Difficulties in the linearization needed in implicit schemes are avoided and the procedure depends only on the sparsity of the Jacobian and the solution from the previous iteration. Therefore the procedure is independent of the complexity of the right hand side and the system can be treated as a black box. The other important advantages are the superlinear convergence property and the simplicity of the procedure. Results of the sparse quasi-Newton method with van Leer's flux splitting and Harten's TVD spatial discretization schemes applied to an inviscid one dimensional nozzle problem showed a significantly faster convergence than the corresponding implicit schemes.

## 5.2 Physical Aspects

The two implicit schemes with multigrid acceleration have been applied to simulate representative hypersonic vehicle shapes. Conclusions drawn from these simulations are:

- 1) For hypersonic flows around a cone using solutions of the N-S equations, the numerical simulation appears to have captured all the mechanisms of the flow field. Strengthening viscous effects appear at increasingly higher angle of attack. The position of the bow shock and the embedded shock, the separation points and the surface pressure distribution are all in reasonable agreement with experimental data.
  
- 2) The hypersonic flow on the leeside of a delta wing was found to behave differently than in the lower speed range from incompressible to supersonic flows. Miller and Wood's chart was found to be incapable of direct extension to the hypersonic regime. New flow structures appear in the hypersonic regime. In all the cases at positive angles of attack, even at  $\alpha = 5^\circ$ , a crossflow induced separation on the wing surface was detected in the numerical simulation. This observation was not found in the experimental work at  $\alpha = 5^\circ$  possibly due to the small size of this recirculation region. Similar to the behaviour of the viscous layer, this recirculation region grows with increase of the angle of attack. The embedded shock, which lies above the rolled-up vortex also strengthens with angle of attack.
  
- 3) The hypersonic flow around a cone-delta-wing combination is considerably more complicated than that over separated shapes due to the the interference between the wing and the body. The nearly straight wing shock and the curved cone shock intersects, resulting in the formation of another shock. This shock further interacts with the boundary layer on the wing and a strong vortical flow is introduced. Due to the high strength of this vortical flow a secondary vortex was also observed between the primary vortex and the wing surface. An embedded shock was detected on the primary vortex. This gives a typical picture of hypersonic flow around wing-body combinations

at a low angle of attack. In contrast to the single cone or the single delta wing case, stronger interactions occur at lower angles of attack due to stronger resulting shock waves.

Leeside flow is mainly dominated by the phenomenon that the cone shock is turned towards the cone surface by the weak wing shock. This induces high localised aerodynamic heating rates on the cone surface.

4) A totally different picture is given by Euler solutions indicating that the viscous/inviscid interaction dominates the flowfield and Euler inviscid modelling does not apply for these simulations. This justifies the higher order modelling by N-S equations in the present research.

### 5.3 Recommendations and Future Work

The research reported in this thesis prompts some topics for further study.

1) The most important extension concerns the application of the sparse quasi-Newton approach to multidimensional cases. This extension necessitates an efficient way to invert the regular sparse matrix resulting from the discretization of the multidimensional problem. Efficient direct inversion of this matrix usually does not exist and some relaxation methods need to be sought. The combination of a relaxation scheme with the sparse quasi-Newton procedure overcomes the two barriers of conventional implicit schemes for fast steady state solution, that is, (1) the difficulty in linearization, i.e. the evaluation of Jacobian; (2) the factorization error due to the approximate factorization used in multidimensional problems.

2) For simplicity only sawtooth multigrid cycling was studied in the present research. More work needs to be carried out to find an optimum strategy.

3) Reduction of computing time per time step for the simplified Beam-Warming scheme can be achieved by replacing the viscous Jacobians  $R$  and  $S$  with the corresponding maximum eigenvalues  $\lambda_{Rmax}I$  and  $\lambda_{Smax}I$ . Therefore the diagonalization as in the Euler solution can be carried out and the block tridiagonal inversion reduces to a scalar tridiagonal inversion. However, the influence of this further simplification on convergence needs to be studied to determine whether it is worthwhile for an efficient steady state solution.

4) With vector supercomputers available, explicit methods show one advantage over implicit ones because they are usually able to be vectorized directly. Vectorization of the implicit codes is clearly a further direction of research for more efficiency. One interesting work has been reported in [60], where the vectorization of the Beam-Warming implicit scheme is achieved.

5) More flowfield investigations can be done with the present codes. For example, extensive simulation of the hypersonic flow on the leeward side of delta wings may extend Miller and Wood's classification to the hypersonic regime. Other geometries which can be directly simulated with the present codes include a waverider shape composed of a right angle caret wing, a cone with a nose fin, cone-body combined with a dihedral delta wing. Indeed, supersonic and hypersonic flow around any conical shapes composed of spherical coordinate surfaces can be simulated directly by the present codes.

6) For more general conical shapes or even more general 3D geometries, general 2D or 3D grid generation techniques need to be employed. This is clearly an important factor for simulation of more practical 3D problems.

APPENDIX A

JACOBIANS FOR LCNSE

$$A_I = \frac{\partial F_I}{\partial U}$$

$$= \begin{bmatrix} 0 & 0 & 1 & 0 & 0 \\ -u_r u_\theta & u_\theta & u_r & 0 & 0 \\ -u_\theta^2 + \beta\alpha & -\beta u_r & (3-\gamma)u_\theta & -\beta u_\varphi & \beta \\ -u_\theta u_\varphi & 0 & u_\varphi & u_\theta & 0 \\ u_\theta[-\gamma e + 2\beta\alpha] & -\beta u_\theta u_r & \gamma e - \beta(\alpha + u_\theta^2) & -\beta u_\theta u_\varphi & \gamma u_\theta \end{bmatrix} \quad (A-1)$$

$$B_I = \frac{\partial G_I}{\partial U} = \frac{1}{\sin\theta} \times$$

$$\begin{bmatrix} 0 & 0 & 0 & 1 & 0 \\ -u_r u_\varphi & u_\theta & 0 & u_r & 0 \\ -u_\theta u_\varphi & 0 & u_\varphi & u_\theta & 0 \\ -u_\varphi^2 + \beta\alpha & -\beta u_r & -\beta u_\theta & (3-\gamma)u_\varphi & \beta \\ u_\varphi[-\gamma e + 2\beta\alpha] & -\beta u_\varphi u_r & -\beta u_\theta u_\varphi & \gamma e - \beta(\alpha + u_\varphi^2) & \gamma u_\theta \end{bmatrix} \quad (A-2)$$

$$C_I = \frac{\partial H_I}{\partial U}$$

$$= \begin{bmatrix} 0 & 2 & 0 & 0 & 0 \\ -u_r^2 + 2\alpha & 4u_r & -2u_\theta & -2u_\varphi & 0 \\ -3u_r u_\theta - ctg\theta(u_\varphi + \alpha) & 3u_\theta + u_r ctg\theta & 3u_r + u_\theta ctg\theta & -u_\varphi ctg\theta & 1 - ctg\theta \\ 3u_r u_\varphi - ctg\theta u_\theta u_\varphi & 3u_\varphi & u_\varphi ctg\theta & 3u_r + u_\theta ctg\theta & 0 \\ -2u_r[(e+p/\rho) + \alpha\beta] & 2[(e+p/\rho) - u_r^2\beta] & -2\beta u_r u_\theta & -2\beta u_r u_\varphi & 2\gamma u_r \end{bmatrix} \quad (A-3)$$

$$R = \frac{\partial F_{V1}}{\partial U_{\theta}} = \frac{\mu}{Re_{\infty, r\rho}}$$

$$= \begin{bmatrix} 0 & 0 & 0 & 0 & 0 \\ -u_r & 1 & 0 & 0 & 0 \\ - (4/3)u_{\theta} & 0 & 4/3 & 0 & 0 \\ -u_{\varphi} & 0 & 0 & 1 & 0 \\ \frac{\gamma}{Pr}(-e+2\alpha)-2\alpha-\frac{u_{\theta}^2}{3} & (-\frac{\gamma}{Pr}+1)u_r & (-\frac{\gamma}{Pr} + \frac{4}{3})u_{\theta} & (-\frac{\gamma}{Pr}+1)u_{\varphi} & \frac{\gamma}{Pr} \end{bmatrix}$$

(A-4)

$$S = \frac{\partial G_{V2}}{\partial U_{\varphi}} = \frac{\mu}{\sin^2 \theta Re_{\infty, r\rho}} \times$$

$$\begin{bmatrix} 0 & 0 & 0 & 0 & 0 \\ -u_r & 1 & 0 & 0 & 0 \\ -u_{\theta} & 0 & 1 & 0 & 0 \\ - (4/3)u_{\varphi} & 0 & 0 & 4/3 & 0 \\ \frac{\gamma}{Pr}(-e+2\alpha)-2\alpha-\frac{u_{\varphi}^2}{3} & (-\frac{\gamma}{Pr}+1)u_r & (-\frac{\gamma}{Pr}+1)u_{\theta} & (-\frac{\gamma}{Pr} + \frac{4}{3})u_{\varphi} & \frac{\gamma}{Pr} \end{bmatrix}$$

(A-5)

where  $\alpha = \frac{1}{2} (u_r^2 + u_{\theta}^2 + u_{\varphi}^2)$ ,  $\beta = \gamma - 1$ ,  $U_{\theta} = \frac{\partial U}{\partial \theta}$ ,  $U_{\varphi} = \frac{\partial U}{\partial \varphi}$

APPENDIX B

DIAGONIZATION OF  $A_I$  AND  $B_I$

The inviscid Jacobians  $A_I$  and  $B_I$  can be diagonalized by  $S_\theta$  and  $S_\varphi$  respectively, i.e.

$$A_I = S_\theta^{-1} \Lambda_A S_\theta, \quad B_I = S_\varphi^{-1} \Lambda_B S_\varphi, \quad (B-1)$$

where

$$S_\theta = T_\theta P = \begin{bmatrix} 1 & 0 & 0 & 0 & -1/c^2 \\ 0 & 1 & 0 & 0 & 0 \\ 0 & 0 & \rho c & 0 & 1 \\ 0 & 0 & 0 & 1 & 0 \\ 0 & 0 & -\rho c & 0 & 1 \end{bmatrix} \begin{bmatrix} 1 & 0 & 0 & 0 & 0 \\ -u_r/\rho & 1/\rho & 0 & 0 & 0 \\ -u_\theta/\rho & 0 & 1/\rho & 0 & 0 \\ -u_\varphi/\rho & 0 & 0 & 1/\rho & 0 \\ \alpha\beta & -u_r\beta & -u_\theta\beta & -u_\varphi\beta & \beta \end{bmatrix}$$

$$= \begin{bmatrix} 1-\alpha\beta/c^2 & \beta u_r/c^2 & \beta u_\theta/c^2 & \beta u_\varphi/c^2 & -\beta/c^2 \\ -u_r/\rho & 1/\rho & 0 & 0 & 0 \\ -cu_\theta+\alpha\beta & -\beta u_r & c-\beta u_\theta & -\beta u_\varphi & \beta \\ -u_\varphi/\rho & 0 & 0 & 1/\rho & 0 \\ cu_\theta+\alpha\beta & -\beta u_r & -c-\beta u_\theta & -u_\varphi\beta & \beta \end{bmatrix} \quad (B-2)$$

$$S_\theta^{-1} = P^{-1} T_\theta^{-1} = \begin{bmatrix} 1 & 0 & 0 & 0 & 0 \\ u_r & \rho & 0 & 0 & 0 \\ u_\theta & 0 & \rho & 0 & 0 \\ u_\varphi & 0 & 0 & \rho & 0 \\ \alpha & \rho u_r & \rho u_\theta & \rho u_\varphi & 1/\beta \end{bmatrix} \begin{bmatrix} 1 & 0 & 1/2c^2 & 0 & 1/2c^2 \\ 0 & 1 & 0 & 0 & 0 \\ 0 & 0 & 1/2\rho c & 0 & -1/2\rho c \\ 0 & 0 & 0 & 1 & 0 \\ 0 & 0 & 1/2 & 0 & 1/2 \end{bmatrix}$$

$$= \begin{bmatrix} 1 & 0 & 1/2c^2 & 0 & 1/2c^2 \\ u_r & \rho & u_r/2c^2 & 0 & u_r/2c \\ u_\theta & 0 & u_\theta/2c^2 + 1/2c & 0 & u_\theta/2c^2 - 1/2c \\ u_\varphi & 0 & u_\varphi/2c^2 & \rho & u_\varphi/2c^2 \\ \alpha & \rho u_r & \alpha/2c^2 + u/2c + 1/2\beta & \rho u_\varphi & \alpha/2c^2 - u_\theta/2c + 1/2\beta \end{bmatrix} \quad (B-3)$$

$$S_{\varphi} = T_{\varphi}P = \begin{bmatrix} 1 & 0 & 0 & 0 & -1/c^2 \\ 0 & 1 & 0 & 0 & 0 \\ 0 & 0 & 1 & 0 & 0 \\ 0 & 0 & 0 & \rho c & 1 \\ 0 & 0 & 0 & -\rho c & 1 \end{bmatrix} \begin{bmatrix} 1 & 0 & 0 & 0 & 0 \\ -u_r/\rho & 1/\rho & 0 & 0 & 0 \\ -u_{\theta}/\rho & 0 & 1/\rho & 0 & 0 \\ -u_{\varphi}/\rho & 0 & 0 & 1/\rho & 0 \\ \alpha\beta & -u_r\beta & -u_{\theta}\beta & -u_{\varphi}\beta & \beta \end{bmatrix}$$

$$= \begin{bmatrix} 1-\alpha\beta/c^2 & \beta u_r/c^2 & \beta u_{\theta}/c^2 & \beta u_{\varphi}/c^2 & -\beta/c^2 \\ -u_r/\rho & 1/\rho & 0 & 0 & 0 \\ -u_{\theta}/\rho & 0 & 1/\rho & 0 & 0 \\ -c u_{\varphi} + \alpha\beta & -\beta u_r & -\beta u_{\theta} & c - \beta u_{\varphi} & \beta \\ c u_{\varphi} + \alpha\beta & -\beta u_r & -\beta u_{\theta} & -c - \beta u_{\varphi} & \beta \end{bmatrix} \quad (\text{B-4})$$

$$S_{\varphi}^{-1} = P^{-1}T_{\varphi}^{-1} = \begin{bmatrix} 1 & 0 & 0 & 0 & 0 \\ u_r & \rho & 0 & 0 & 0 \\ u_{\theta} & 0 & \rho & 0 & 0 \\ u_{\varphi} & 0 & 0 & \rho & 0 \\ \alpha & \rho u_r & \rho u_{\theta} & \rho u_{\varphi} & 1/\beta \end{bmatrix} \begin{bmatrix} 1 & 0 & 0 & 1/2c^2 & 1/2c^2 \\ 0 & 1 & 0 & 0 & 0 \\ 0 & 0 & 1 & 0 & 0 \\ 0 & 0 & 0 & 1/2\rho c & -1/2\rho c \\ 0 & 0 & 0 & 1/2 & 1/2 \end{bmatrix}$$

$$= \begin{bmatrix} 1 & 0 & 0 & 1/2c^2 & 1/2c^2 \\ u_r & \rho & 0 & u_r/2c^2 & u_r/2c \\ u_{\theta} & 0 & \rho & u_{\theta}/2c^2 & u_{\theta}/2c^2 \\ u_{\varphi} & 0 & 0 & u_{\varphi}/2c^2 + 1/2c & u_{\varphi}/2c^2 - 1/2c \\ \alpha & \rho u_r & \rho u_{\theta} & \alpha/2c^2 + u_{\varphi}/2c + 1/2\beta & \alpha/2c^2 - u_{\varphi}/2c + 1/2\beta \end{bmatrix} \quad (\text{B-5})$$

## APPENDIX C

### ADAPTIVE ARTIFICIAL VISCOSITY

In the present simulation of hypersonic flows all the shock waves are captured from the numerical solution. Although shock fitting is also possible in some cases, the complexity of the interaction and the existence of embedded shock waves make this approach too complicated to apply. However in order to capture shock waves by central differencing numerical schemes some explicit artificial viscosity term needs to be introduced to overcome the oscillation near the shock waves. The artificial viscosity technique used in the present simulation is a modification of the adaptive artificial dissipation proposed by Jameson [61]. From numerical tests the following modifications were made.

1) Jameson used a combined second and fourth order artificial dissipation for his Euler solution. However the fourth order artificial viscosity term was found not necessary in the present hypersonic N-S solution. And its use degraded the accuracy of viscous parameters such as heat transfer. Therefore only the second order term is retained.

2) It was found that the artificial viscosity term needs to be totally switched off near the wall. This is essential for a accurate viscous solution. Also found from the numerical experience was its strong influence on the convergence. If it is not totally switched off near the wall the residuals near the wall cannot go down any further after two or three orders of reduction.

The present artificial viscosity in the  $\theta$  direction has the following form:

$$D_{\theta i, j} = d_{\theta i+\frac{1}{2}, j} - d_{\theta i-\frac{1}{2}, j} \quad (C-1)$$

with

$$d_{\theta i+\frac{1}{2}, j} = C_{\theta i+\frac{1}{2}, j} \epsilon_{i+\frac{1}{2}, j} ( U_{i+1, j} - U_{i, j} ) \quad (C-2)$$

where

$$C_{\theta i+\frac{1}{2},j} = k_0 |u_{\theta+c}| / \Delta \theta_i \quad (C-3)$$

The  $\theta$  direction sensor of a shock wave,  $\nu_{\theta i,j}$ , is defined by

$$\nu_{\theta i,j} = \left| \frac{p_{i+1,j} - 2p_{i,j} + p_{i-1,j}}{p_{i+1,j} + 2p_{i,j} + p_{i-1,j}} \right| \quad (C-4)$$

$$\overline{\nu_{\theta i+\frac{1}{2},j}} = \max ( \nu_{\theta i+2,j}, \nu_{\theta i+1,j}, \nu_{\theta i,j}, \nu_{\theta i-1,j} ) \quad (C-5)$$

$$\epsilon_{\theta i+\frac{1}{2},j} = \min [ k_1, k_2 \max ( 0, \overline{\nu_{\theta i+\frac{1}{2},j}} - k_3 ) ] \quad (C-6)$$

The constants  $k_1$  are chosen in the present simulation as

$$k_0 = 0.1 \quad k_1 = 0.5 \quad k_2 = 1 \quad k_3 = 0.01 \quad (C-7)$$

Note that  $k_3$  is introduced in the present numerical simulation to switch off the artificial viscosity when the pressure gradient is small enough.

The artificial viscosity in the  $\varphi$  direction is similarly defined.

## APPENDIX D

### SOME FOURIER STABILITY ANALYSES

#### D.1 Source Term Influence on Stability

Consider the following problem

$$\frac{\partial u}{\partial t} = -c \frac{\partial u}{\partial x} + \nu \frac{\partial^2 u}{\partial x^2} + s(u) \quad (D-1)$$

Integrate the above equation by backward Euler time differencing and central spatial differencing with the source term treated explicitly

$$\frac{u_j^{n+1} - u_j^n}{\Delta t} = -c \frac{u_{j+1}^{n+1} - u_{j-1}^{n+1}}{2\Delta x} + \nu \frac{u_{j+1}^{n+1} - 2u_j^{n+1} + u_{j-1}^{n+1}}{\Delta x^2} + s(u^n) \quad (D-2)$$

Use Fourier analysis and substitute

$$u_j^n = \xi^n e^{i\sigma x_j} \quad (D-3)$$

into Eq.(D-2) and define the amplification factor  $G$  by

$$\xi^{n+1} = G\xi^n \quad (D-4)$$

Then the magnitude of the amplification factor is

$$|G(\sigma, \Delta t)| = \frac{|1 + (\partial s/\partial u)\Delta t|}{\left\{ (c\Delta t/\Delta x)^2 \sin^2 \sigma \Delta x + [1 + 2(\nu\Delta t/\Delta x^2)(1 - \cos \sigma \Delta x)]^2 \right\}^{1/2}} \quad (D-5)$$

If  $(\partial s/\partial u)$  is bounded, the von Neumann stability condition [62]

$$|G(\sigma, \Delta t)| \leq 1 + O(\Delta t) \quad \text{for all } \sigma \quad (D-6)$$

is always satisfied. Hence the finite difference scheme is unconditionally stable. From this analysis the *normal* source term with explicit treatment has no influence on the stability properties in the von Neumann sense.

However for practical problems  $\Delta t$  has a finite size and the influence of the source term on stability is reflected in Eq.(D-6) through the term  $(\partial s/\partial u)\Delta t$ .

a) If  $-2/\Delta t \leq \partial s/\partial u \leq 0$ , the explicit source term treatment has the effect of stabilizing the method.

b) If  $\partial s/\partial u > 0$  or  $\partial s/\partial u < -2/\Delta t$ , the source term with explicit treatment has the effect of degrading the stability. The limit is the *abnormal* case where  $\partial s/\partial u$  is so large that the stability is totally destroyed.

One may naturally think that the implicit treatment of the source term could make a positive influence on stability from the experience with implicitization of convection and diffusion terms. Examine the implicit treatment of the source term, i.e.

$$\frac{u_j^{n+1} - u_j^n}{\Delta t} = -c \frac{u_{j+1}^{n+1} - u_{j-1}^{n+1}}{2\Delta x} + \nu \frac{u_{j+1}^{n+1} - 2u_j^{n+1} + u_{j-1}^{n+1}}{\Delta x^2} + s(u^{n+1}). \quad (D-7)$$

The magnitude of the amplification factor is

$$|G(\sigma, \Delta t)| = \frac{1}{\{(c\Delta t/\Delta x)^2 \sin^2 \sigma \Delta x + [1 + 2(\nu\Delta t/\Delta x^2)(1 - \cos \sigma \Delta x) - (\partial s/\partial u)\Delta t]^2\}^{\frac{1}{2}}} \quad (D-8)$$

Again the von Neumann stability condition (D-6) is satisfied and the scheme is unconditionally stable.

From Eq.(D-8) it is clear that the implicit source term treatment still cannot always have a positive effect on stability.

a) If  $\partial s/\partial u \leq 0$  or  $\partial s/\partial u \geq 2[1/\Delta t + 2(\nu/\Delta x^2)]$ , the implicit treatment of the source term has the effect of stabilizing the method.

b) If  $4(\nu/\Delta x^2) < \partial s/\partial u < 2/\Delta t$ , the implicit source term treatment has the effect of

degrading the stability. It is noted that in this region the stability can be destroyed if  $\partial s/\partial u$  is abnormally large, which can happen in this region.

The above analysis indicates that the von Neumann stability is not influenced by the source term. In practice, the source term, whether treated explicitly or implicitly, has a lower order influence on stability as compared to the convection and diffusion terms. If the derivative  $\partial s/\partial u$  is abnormally large, the stability can be totally destroyed even through implicit treatment of the source term is employed. Implicit treatment of the source term cannot always stabilize the solution while explicit treatment of it can sometime have a positive effect on stability, which depends on the sign and the magnitude of the derivative  $\partial s/\partial u$ . Unfortunately, for the cases where abnormal source terms may occur, e.g. the source term from turbulence modelling, this information is generally unavailable.

For the problem studied in this thesis, the source term in the LCNSE or CEE results from coordinate transformation (from Cartesian to spherical) and from the locally conical approximation. This source term is thought to be *normal* and, therefore, an explicit treatment of the source term is reasonable from above analysis. This was proved from the computational results. No better stability has been observed in the computation with an implicit treatment of the source term.

## D.2 Stability Condition with Explicit Diffusion Term

It is obvious that, in the Beam-Warming implicit scheme, the main computational effort is caused by the inversion of the block tridiagonal matrix. In the inviscid case, Pulliam and Chaussee [56] reduced the block tridiagonal solution to a scalar tridiagonal solution by taking advantage of the known diagonal form of the Jacobians of the inviscid flux vectors. This procedure substantially reduced the computation. Unfortunately, in the viscous case, this cannot be done because there is no single

transformation matrix which can diagonalize the inviscid and the viscous Jacobians simultaneously. One way to employ a diagonal form for N-S solutions is to omit the viscous effect in the implicit operator allowing the implicit part to be diagonalized as in the Euler solution. The question to be asked about this explicit viscous term treatment is whether the stability of the implicit scheme is severely degraded or whether it is worthwhile to pay in stability for the saving in the matrix inversion.

Consider the model convection diffusion problem (D-1) without a source term. If the problem is integrated by

$$\frac{u_j^{n+1} - u_j^n}{\Delta t} = -c \frac{u_{j+1}^{n+1} - u_{j-1}^{n+1}}{2\Delta x} + \nu \frac{u_{j+1}^n - 2u_j^n + u_{j-1}^n}{\Delta x^2}, \quad (D-9)$$

the magnitude of the amplification factor from Fourier analysis will be

$$|G(\sigma, \Delta t)| = \frac{|1 - 2(\nu\Delta t/\Delta x^2)(1 - \cos\sigma\Delta x)|}{[1 + (c\Delta t/\Delta x)^2 \sin^2\sigma\Delta x]^{\frac{1}{2}}}. \quad (D-10)$$

Therefore the stability condition is

$$\Delta t \leq \frac{\Delta x^2}{2\nu}. \quad (D-11)$$

The above analysis reveals that if the diffusion term is treated explicitly the time step will be limited by condition (D-11). It is clear that the inviscid part has been released from the stability condition due to its implicit treatment. But the effect of using condition (D-11) can be severe because viscous computations usually involve very fine mesh near the wall. Therefore simply omitting the viscous effect in the implicit operator is thought not to be a good practice for implicit computation of viscous flows. It is necessary to account for the viscous effect in the implicit operator for the sake of stability, which is an important feature with implicit schemes.

APPENDIX E

TIME STEP DEPENDENCE OF STEADY STATE SOLUTION  
WITH MACCORMACK-TYPE SCHEMES

Consider the following convection diffusion equation

$$\frac{\partial u}{\partial t} = -c \frac{\partial u}{\partial x} + \nu \frac{\partial^2 u}{\partial x^2}. \quad (E-1)$$

Apply the explicit two-step MacCormack scheme to the above model equation,

Predictor:

$$\Delta u_i^n = -\frac{c\Delta t}{\Delta x} (u_{i+1}^n - u_i^n) + \frac{\nu\Delta t}{\Delta x^2} (u_{i+1}^n - 2u_i^n + u_{i-1}^n) \quad (E-2)$$

$$\overline{u_i^{n+1}} = u_i^n + \Delta u_i^n \quad (E-3)$$

Corrector:

$$\Delta \overline{u_i^{n+1}} = -\frac{c\Delta t}{\Delta x} (\overline{u_{i+1}^{n+1}} - \overline{u_{i-1}^{n+1}}) + \frac{\nu\Delta t}{\Delta x^2} (\overline{u_{i+1}^{n+1}} - 2\overline{u_i^{n+1}} + \overline{u_{i+1}^{n+1}}) \quad (E-4)$$

$$u_i^{n+1} = \frac{1}{2} (u_i^n + \overline{u_i^{n+1}} + \Delta \overline{u_i^{n+1}}) \quad (E-5)$$

The two-step scheme is equivalent to the following one-step scheme,

$$\begin{aligned} u_i^{n+1} = & u_i^n + \frac{1}{2} \left\{ -\frac{c\Delta t}{\Delta x} (u_{i+1}^n - u_i^n) + \frac{\nu\Delta t}{\Delta x^2} (u_{i+1}^n - 2u_i^n + u_{i-1}^n) - \frac{c\Delta t}{\Delta x} \left[ u_i^n - \frac{c\Delta t}{\Delta x^2} (u_{i+1}^n - u_i^n) \right. \right. \\ & + \frac{\nu\Delta t}{\Delta x^2} (u_{i+1}^n - 2u_i^n + u_{i-1}^n) - u_{i-1}^n + \frac{c\Delta t}{\Delta x} (u_i^n - u_{i-1}^n) - \frac{\nu\Delta t}{\Delta x^2} (u_i^n - 2u_{i-1}^n + u_{i-2}^n) \left. \right] \\ & + \frac{\nu\Delta t}{\Delta x^2} [u_{i+1}^n - 2u_i^n + u_{i-1}^n - \frac{c\Delta t}{\Delta x} (u_{i+2}^n - u_{i+1}^n - 2u_{i-1}^n + 2u_{i-2}^n + u_i^n - u_{i-1}^n)] \\ & \left. + \left( \frac{\nu\Delta t}{\Delta x^2} \right)^2 [u_{i+2}^n - 2u_{i+1}^n + u_i^n - 2(u_{i+1}^n - 2u_i^n + u_{i-1}^n) + u_i^n - 2u_{i-1}^n + u_{i-2}^n] \right\} \quad (E-6) \end{aligned}$$

The above equation can also be rewritten as

$$\begin{aligned}
\frac{u_i^{n+1} - u_i^n}{\Delta t} &= -c \frac{u_{i+1}^n - u_{i-1}^n}{2\Delta x} + \nu \frac{u_{i+1}^n - 2u_i^n + u_{i-1}^n}{\Delta x^2} \\
&+ \frac{1}{2} c^2 \Delta t \frac{u_{i+1}^n - 2u_i^n + u_{i-1}^n}{\Delta x^2} \\
&- c\nu \Delta t \left( \frac{u_{i+2}^n - 2u_{i+1}^n + u_i^n}{\Delta x^2} - \frac{u_i^n - 2u_{i-1}^n + u_{i-2}^n}{\Delta x^2} \right) / 2\Delta x \\
&+ \frac{1}{2} \nu^2 \Delta t \frac{u_{i+2}^n - 4u_{i+1}^n + 6u_i^n - 4u_{i-1}^n + u_{i-2}^n}{\Delta x^4} \tag{E-7}
\end{aligned}$$

From the Taylor expansion

$$\frac{u_i^{n+1} - u_i^n}{\Delta t} = \left( \frac{\partial u}{\partial t} \right)_i^n + \frac{\Delta t}{2} \left( \frac{\partial^2 u}{\partial t^2} \right)_i^n + O(\Delta t^2) \tag{E-8}$$

Use Eq.(E-1)

$$\left( \frac{\partial^2 u}{\partial t^2} \right)_i = c^2 \left( \frac{\partial^2 u}{\partial x^2} \right)_i - 2c\nu \frac{\partial^3 u}{\partial x^3} + \nu^2 \frac{\partial^4 u}{\partial x^4} \tag{E-9}$$

These three terms from the second order time derivative are approximated by the last three terms on the right hand side of Eq.(E-7). Therefore the scheme is proved second order accurate in both time and space.

However it is important to note that, if steady state is achieved,  $(u_i^{n+1} - u_i^n)/\Delta t = 0$ , the solution clearly depends on the time step through the last three terms on the right hand side of Eq. (E-7).

It is clear that these terms have stronger influence in the regions where the derivatives are larger and, therefore, stronger time step dependence of the steady state solution will occur in these regions.

In the transient analysis, the MacCormack scheme is a second order finite difference scheme with a truncation error  $O(\Delta t^2, \Delta x^2)$ . However, in the steady-state

analysis, because the term  $(u_i^{n+1} - u_i^n)/\Delta t$  is missing the last three terms on the right hand side of Eq.(E-7) can no longer be balanced by the transient error on the left hand side and remain as implicit artificial viscosity terms. These implicit artificial viscosity terms are results of steady state analysis. Roache [63] pointed out the difference in transient and steady state analysis for some other schemes. When a time marching scheme is used for a steady state problem, a steady state analysis should be considered.

All the MacCormack type two-step schemes, such as the implicit MacCormack scheme presented in this thesis, are based on the two-step explicit scheme so that the steady state solution from these schemes are all actually dependent on time steps used in the time marching. From Eq.(E-7) it is clear that the only way to reduce this  $\Delta t$ -dependence and to achieve a accurate steady state solution with MacCormack-type schemes is to reduce the  $\Delta t$  and therefore reduce these implicit artificial viscosity effects in steady state solution.

To compare with this  $\Delta t$ -dependence, apply the Beam-Warming scheme with backward Euler time differencing, i.e. backward-time centred-space differencing, to the model problem, then

$$\frac{u_i^{n+1} - u_i^n}{\Delta t} = -c \frac{u_{i+1}^{n+1} - u_{i-1}^{n+1}}{2\Delta x} + \nu \frac{u_{i+1}^{n+1} - 2u_i^{n+1} + u_{i-1}^{n+1}}{\Delta x^2} \quad (E-10)$$

It is clear from the above expression that when the finite difference solution of the above equation reaches a steady state the solution will approximate the steady state partial differential equation to the second order without any time step dependence. The steady state independence of  $\Delta t$  is obvious.

The key point is that the MacCormack scheme mixes the time and the spatial discretization while in the Beam-Warming scheme the time discretization and the spatial discretization is independent.

## APPENDIX F

### DISTRIBUTION FORMULA FOR EQUATIONS WITH SOURCE TERM

For simplicity of presentation the following one dimensional problem is considered

$$\frac{\partial U}{\partial t} + \frac{\partial F}{\partial x} + H = 0 \quad (F-1)$$

The Taylor series expansion gives

$$\delta U_i^n = U_i^{n+1} - U_i^n = \left(\frac{\partial U}{\partial t}\right)_i^n \Delta t + \left(\frac{\partial^2 U}{\partial t^2}\right)_i^n \frac{\Delta t^2}{2} + O(\Delta t^2) \quad (F-2)$$

From Eq. (F-1)

$$\left(\frac{\partial U}{\partial t}\right)_i^n = -\left(\frac{\partial F}{\partial x} + H\right)_i^n = -\left(\frac{F_{i+1} - F_{i-1}}{2\Delta x} + H\right)_i^n + O(\Delta x^2) \quad (F-3)$$

$$\begin{aligned} \left(\frac{\partial^2 U}{\partial t^2}\right)_i^n &= \frac{\partial}{\partial x} \left[ \frac{\partial F}{\partial U} \left(\frac{\partial F}{\partial x} + H\right) \right]_i^n + \left[ \frac{\partial H}{\partial U} \left(\frac{\partial F}{\partial x} + H\right) \right]_i^n \\ &= \frac{1}{\Delta x} \left\{ \left(\frac{\partial F}{\partial U}\right)_{i+\frac{1}{2}} \left[ \frac{1}{\Delta x} (F_{i+1} - F_i) + H_{i+\frac{1}{2}} \right] - \left(\frac{\partial F}{\partial U}\right)_{i-\frac{1}{2}} \left[ \frac{1}{\Delta x} (F_i - F_{i-1}) + H_{i-\frac{1}{2}} \right] \right\}^n \\ &\quad + \frac{1}{2} \left\{ \left(\frac{\partial H}{\partial U}\right)_{i+\frac{1}{2}} \left[ \frac{1}{\Delta x} (F_{i+1} - F_i) + H_{i+\frac{1}{2}} \right] + \left(\frac{\partial H}{\partial U}\right)_{i-\frac{1}{2}} \left[ \frac{1}{\Delta x} (F_i - F_{i-1}) + H_{i-\frac{1}{2}} \right] \right\}^n \\ &\quad + O(\Delta x^2) \end{aligned} \quad (F-4)$$

Define

$$\Delta U_{i-\frac{1}{2}} = [-(F_i - F_{i-1})/\Delta x - H_{i-\frac{1}{2}}] \Delta t \quad (F-5)$$

$$\Delta F_{i-\frac{1}{2}} = \left(\frac{\partial F}{\partial U}\right)_{i-\frac{1}{2}} \Delta U_{i-\frac{1}{2}} \quad (F-6)$$

$$\Delta H_{i-\frac{1}{2}} = \left(\frac{\partial H}{\partial U}\right)_{i-\frac{1}{2}} \Delta U_{i-\frac{1}{2}} \quad (F-7)$$

then the distribution formula can be written as

$$\begin{aligned} \delta U_i &= \frac{1}{2} \left[ \Delta U - \Delta t \left( \frac{\Delta F}{\Delta x} + \frac{1}{2} \Delta H \right) \right]_{i+\frac{1}{2}} \\ &\quad + \frac{1}{2} \left[ \Delta U - \Delta t \left( -\frac{\Delta F}{\Delta x} + \frac{1}{2} \Delta H \right) \right]_{i-\frac{1}{2}} \end{aligned} \quad (F-8)$$

The distribution formula with source term for the two dimensional case, which are used in Sec. 3.4.1, can be derived similarly.

## REFERENCES

1. Burns, B. R. A., "HOTOL: A Multi-Role Aerospacecraft for Europe,"  
*Aerospace*, July/August 1987, pp8-15.
2. Williams, R. M., "National Aero-Space Plane: Technology for America's  
Future," *Aerospace America*, November 1986, pp18-22.
3. Richards, B. E., "Kinetic Heating of High Speed Missiles,"  
Missile Aerodynamics, AGARD-LS-98, 1979, Paper 9.
4. Wake, A., "Hypersonic Aerodynamics - Application for HOTOL,"  
Aerodynamics of Hypersonic Lifting Vehicles, AGARD-CP-428,  
1987, Paper 34.
5. Current Capabilities and Future Directions in Computational Fluid  
Dynamics, National Academic Press, Washington D.C., 1986.
6. Kutler, P. "A Perspective of Computational Fluid Dynamics," *Lect  
Notes in Phys*, vol. 264, 1986, pp30-46.
7. MacCormack, R. W., "A Numerical Method for Solving the Equations of  
Compressible Viscous Flow," *AIAA J*, vol. 20, 1982, pp1275-1281.
8. Beam, R. M. and Warming, R. F., "An Implicit Factored Scheme for the  
Compressible Navier-Stokes Equations," *AIAA J*, vol. 16, 1978,  
pp393-402.
9. Hackbusch, W. and Trottenberg, U.(Eds), Multigrid Methods, *Lect Notes  
in Math*, vol. 960, 1982.
10. Ni, R. H., "A Multiple Grid Scheme for Solving the Euler Equations,"  
*AIAA J*, vol. 20, 1982, pp1565-1571.
11. Johnson, G. M., "Multiple-Grid Convergence Acceleration of Viscous and Inviscid  
Flow Computations," *Appl Math Comp*, vol. 13, 1983, pp375-398.
12. Jameson, A., "Solution of the Euler Equations by a Multigrid Method",  
*Applied Math and Comp*, vol. 13, 1983, pp327-356.

13. Qin, Ning and Richards, B. E., "Simulation of Hypersonic Viscous Flows around a Cone-Delta-Wing Combination by an Implicit Method with Multigrid Acceleration," *Lect Notes in Phys*, vol. 287, 1986, pp528-532.
14. Brandt, A., "Multilevel Adaptive Computations in Fluid Dynamics," *AIAA J*, vol. 18, 1980, pp1165-1172.
15. Stuben, K. and Trottenberg, U., "Multigrid Methods: Fundamental Algorithms, Model Problem Analysis and Application," *Lect Notes in Math*, vol. 960, 1982, pp1-176.
16. Schubert, L. K., "Modification of a Quasi-Newton Method for Nonlinear Equations with a Sparse Jacobian," *Math Comp*, vol. 24, 1970, pp27-30.
17. Broyden, C. G., "The Convergence of an Algorithm for Solving Sparse Nonlinear Systems," *Math Comp*, vol. 25, 1971, pp285-294.
18. Marvil, E. S. "Convergence Results for Schubert's Method for Solving Sparse Nonlinear Equations," *SIAM J Numer Anal*, vol. 16, 1979, pp588-604.
19. Dennis, J. E., Jr. and Schnabel, R. B., Numerical Methods for Unconstrained Optimization and Nonlinear Equations, Prentice Hall, Englewood Cliffs, N.Y., 1983, Chapter 11.
20. Curtis, A., Powell, M. J. D. and Reid, J. K., "On the Estimation of Sparse Jacobian Matrices," *JIMA*, vol. 13, 1974, pp117-120.
21. Qin, Ning and Richards, B. E., "Sparse Quasi-Newton Method for High Resolution Schemes," Proceedings of 7th GAMM Conference on Numerical Methods in Fluid Mechanics, Vieweg Verlag, 1987.
22. Qin, Ning and Richards, B. E., "Sparse Quasi-Newton Method for Fast Steady State Solution," University of Glasgow, Department of Aeronautics and Fluid Mechanics, Report 8705, 1987.
23. Van Leer, B., "Flux-Vector Splitting for the Euler Equations," *Lect Notes in Phys*, vol. 170, 1982, pp507-511

24. Van Leer, B., "Towards Ultimate Conservative Difference Scheme V: A Second-Order Sequel to Godunov's Method," *J Comp Phys*, vol. 32, 1979, pp101-136.
25. Harten, A., "On a Class of High Resolution Total-Variation-Stable Finite Difference Schemes," *SIAM J Numer Anal*, vol. 21, 1984, pp1-23.
26. Yee, H. C., Warming, R. E. and Harten, A., "Implicit Total Variation Diminishing (TVD) Schemes for Steady State Calculations," *J Comp Phys*, vol. 57, 1985, pp327-360.
27. Tracy, R. R., "Hypersonic Flow over a Yawed Circular Cone," *California Institute of Technology, Aeronautical Laboratories Memorandum*, Number 69, 1963.
28. Cross, E. T., Jr. and Hankey, W. L., "Investigation of Leeward Side of a Delta Wing at Hypersonic Speeds," *J Spacecraft*, vol. 6, 1969, pp185-190.
29. Meyer, R. F. and Vail, C. F., "An Experimental Study of the Hypersonic Flow about a Particular Half-Cone-and-Delta-Wing Lifting Configuration," *NRC, NAE Aero Report LR-475,1967*.
30. Dunavant, J. C., "Heat Transfer to a Delta Wing-Half-Cone Combination at Mach Number of 7 and 10," *NASA TN D-2199*, 1964.
31. Scheuing, R. A., "Outer Inviscid Hypersonic Flow with Attached Shock Waves," *ARS J*, vol. 31, 1961, pp486-505.
32. Qin, Ning and Richards, B. E., "Numerical Experiments with Hypersonic Flow beneath a Cone-Delta-Wing Combination," *Aerodynamics of Hypersonic Lifting Vehicles*, *AGARD-CP-428*, Paper 20, 1987.
33. Qin, Ning and Richards, B. E., "Prediction of the Hypersonic Flow on the Leaside of a Cone-Delta-Wing Combination," *The Aerodynamics of Spacecraft*, *Euromech 225*, Cranfield, July 1987.
34. Peyret, R. and Viviand, H., "Computation of Viscous Compressible Flows Based on the Navier-Stokes Equations," *AGARD-AG-212*, 1975.

35. MacRae, D. S. and Hussaini, M. Y., "Numerical Simulation of Supersonic Cone Flow at High Angle of Attack," High Angle of Attack Aerodynamics, AGARD-CP-247, 1979, paper 23.
36. Shang, J. S., "An Assessment of Numerical Solution of the Compressible Navier-Stokes Equations," *J Aircraft*, vol. 22, 1985, pp353-370.
37. MacCormack, R. W., "The Effect of Viscosity in Hypervelocity Impact Cratering," *AIAA-69-354*, 1969.
38. Shang, J. S., Buning, P. G., Hankey, W. L., and Wirth, M. C., "Performance of a Vectorized Three-Dimensional Navier-Stokes Code on the CRAY-1 Computer," *AIAA J*, vol. 18, 1980, pp1073-1079.
39. Jameson, A., Schmidt, W. and Turkel, E., "Numerical Solution of the Euler Equations by Finite Volume Methods Using Runge-Kutta Time-Stepping Schemes," *AIAA-81-1259*, 1981.
40. Swanson, R. C. and Turkel, E., "A Multistage Time-Stepping Scheme for the Navier-Stokes Equations," *AIAA-85-35*, 1985.
41. Briley, W. R. and McDonald, H., "Solution of the Multidimensional Compressible Navier-Stokes Equations by a Generalized Implicit Method," *J Comp Phys*, vol. 24, 1977, pp372-397.
42. Shang, J. S. and MacCormack, R. W., "Flow over a Biconic Configuration with an after Body Compression Flap - A Comparative Numerical Study," *AIAA-83-1668*, 1983.
43. Lawrence, S. L., Tannehill, J. C. and Chaussee, D. S., "Application of the Implicit MacCormack Scheme to the Parabolized Navier-Stokes Equations," *AIAA J*, vol. 22, 1984, pp1755-1763.
44. Gupta, R. N., Guoffo, P. A. and MacCormack, R. W., "Viscous Shock-Layer Flowfield Analysis by an Explicit-Implicit Method," *AIAA J*, vol. 23, 1985, pp723-732.
45. Jiang, Dachun, "Prediction of Shock/Turbulent Boundary Layer Separated Flows using the Navier-Stokes Equations," Ph.D. Thesis, Department of Aeronautics and Fluid Mechanics, University of Glasgow, 1986.

46. Chakravarthy, S. R., "Relaxation Methods for Unfactored Implicit Upwind Schemes," *AIAA-84-0165*, 1984.
47. MacCormack, R. W., "Current Status of Numerical Solutions of the Navier-Stokes Equations," *AIAA-85-0032*, 1985.
48. Mulder, W. A., "Multigrid Relaxation for the Euler Equations," *Lect Notes in Phys*, vol. 218, pp417-421.
49. Thomas, J. L. and Walters, R. W., "Upwind Relaxation Algorithms for the Navier-Stokes Equations," *AIAA-85-1501*, 1985.
50. Steger, J. L. and Warming, R. F., "Flux Vector Splitting of the Inviscid Gasdynamic Equations with Application to Finite Difference Methods," *J Comp Phys*, vol. 40, 1981, pp263-293.
51. Osher, S., "Riemann Solvers, the Entropy Condition, and Difference Approximations," *SIAM J Numer Anal*, vol. 21, 1984, pp217-235
52. Roe, P., "Approximate Riemann Solvers, Parameter Vectors, and Difference Schemes," *J Comp Phys*, vol. 43, 1981, pp357-372.
53. Van Leer, B., Thomas, J. L., Roe, P. and Newsome, R. W., "A Comparison of Numerical Flux Formulas for the Euler and Navier-Stokes Equations," *AIAA-87-1104*, 1987.
54. Pulliam, T. H., "Artificial Dissipation Models for the Euler Equations," *AIAA J*, vol. 24, 1986, pp1931-1940.
55. Yee, H. and Harten, A., "Implicit TVD Schemes for Hyperbolic Conservation Laws in Curvilinear Coordinates," *AIAA-85-1531*, 1985.
56. Pulliam, T. H. and Chaussee, D. S., "A Diagonal Form of an Implicit Approximate-Factorization Algorithm," *J Comp Phys*, vol. 39, 1981, pp347-363.
57. Mulder, W. A. and van Leer, B., "Experiments with Implicit Upwind Methods for the Euler Equations," *J Comp Phys*, vol. 59, 1985, pp232-246.
58. Stanbrook, A. and Squire, L. C., "Possible Types of Flow at Swept Leading Edges," *Aeron Quarterly*, vol. XV, 1964, pp72-82.

59. Miller, D. S. and Wood, R. M., "An Investigation of Wing Leading-Edge Vortices at Supersonic Speeds," *J Aircraft*, vol. 21, 1984, pp680-686.
60. Muller, B., "Vectorization of the implicit Beam and Warming Scheme," in: Vectorization of Computer Programs with Application to Computational Fluid Dynamics, (Ed. by Gentzsch, W.) Vieweg Verlag, Braunschweig, 1984, pp172-194.
61. Jameson, A., "Transonic Flow Calculations for Aircraft," *Lect Notes in Math*, vol. 1127, pp156-242.
62. Richtmyer, R. D. and Morton, K. W., Difference Methods for Initial-Value Problems, Second Edition, Interscience Publishers, J. Wiley and Sons, New York, 1967.
63. Roache, P. J., Computational Fluid Dynamics, Hermosa Publishers, Albuquerque, N.M., 1972.

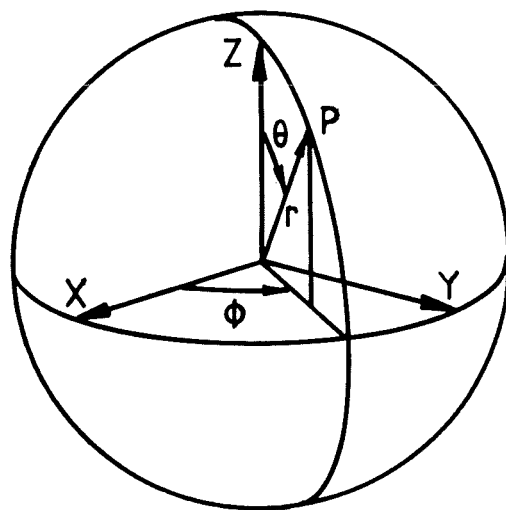


Fig. 2.1 Relation between Cartesian and Spherical Coordinates

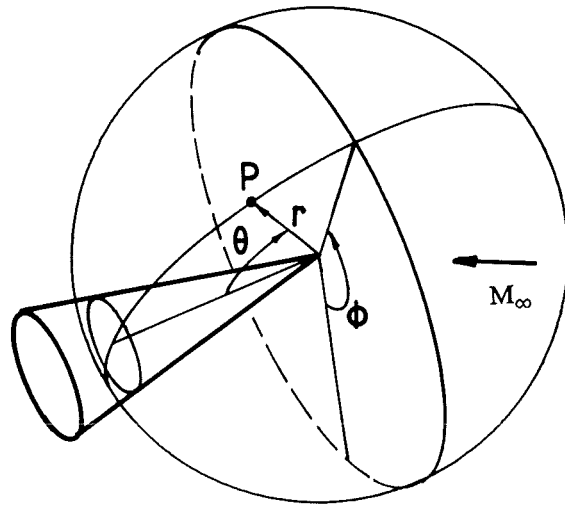


Fig. 2.2 Cone in Spherical Coordinates

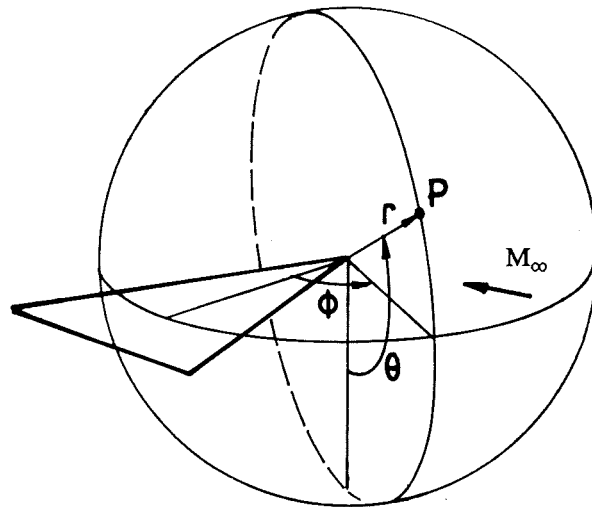


Fig. 2.3 Delta Wing in Spherical Coordinates

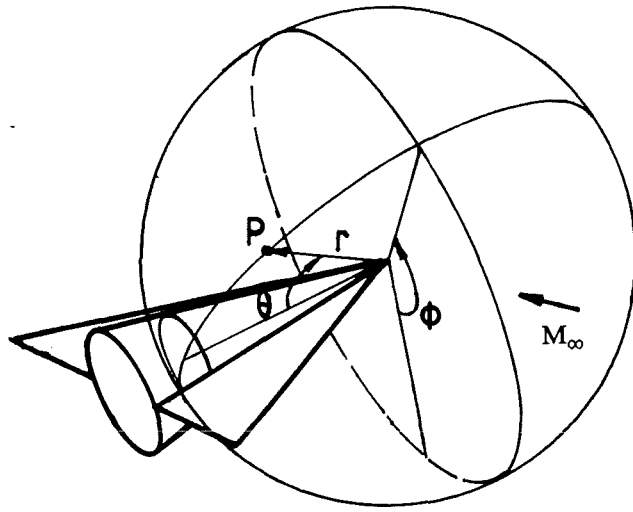


Fig. 2.4 Cone-Delta-Wing Combination in Spherical Coordinates

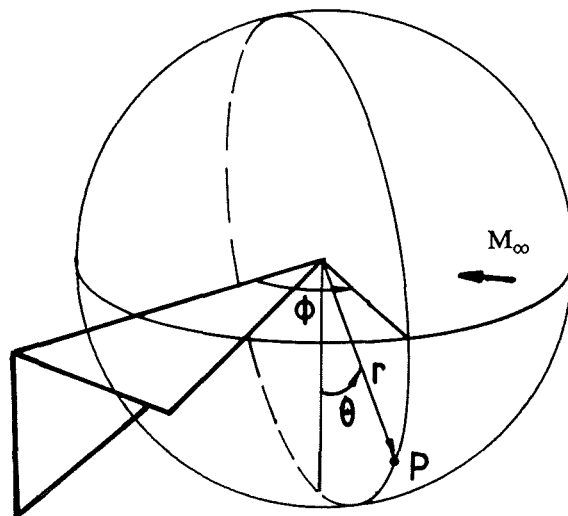


Fig. 2.5 Caret Wing in Spherical Coordinates

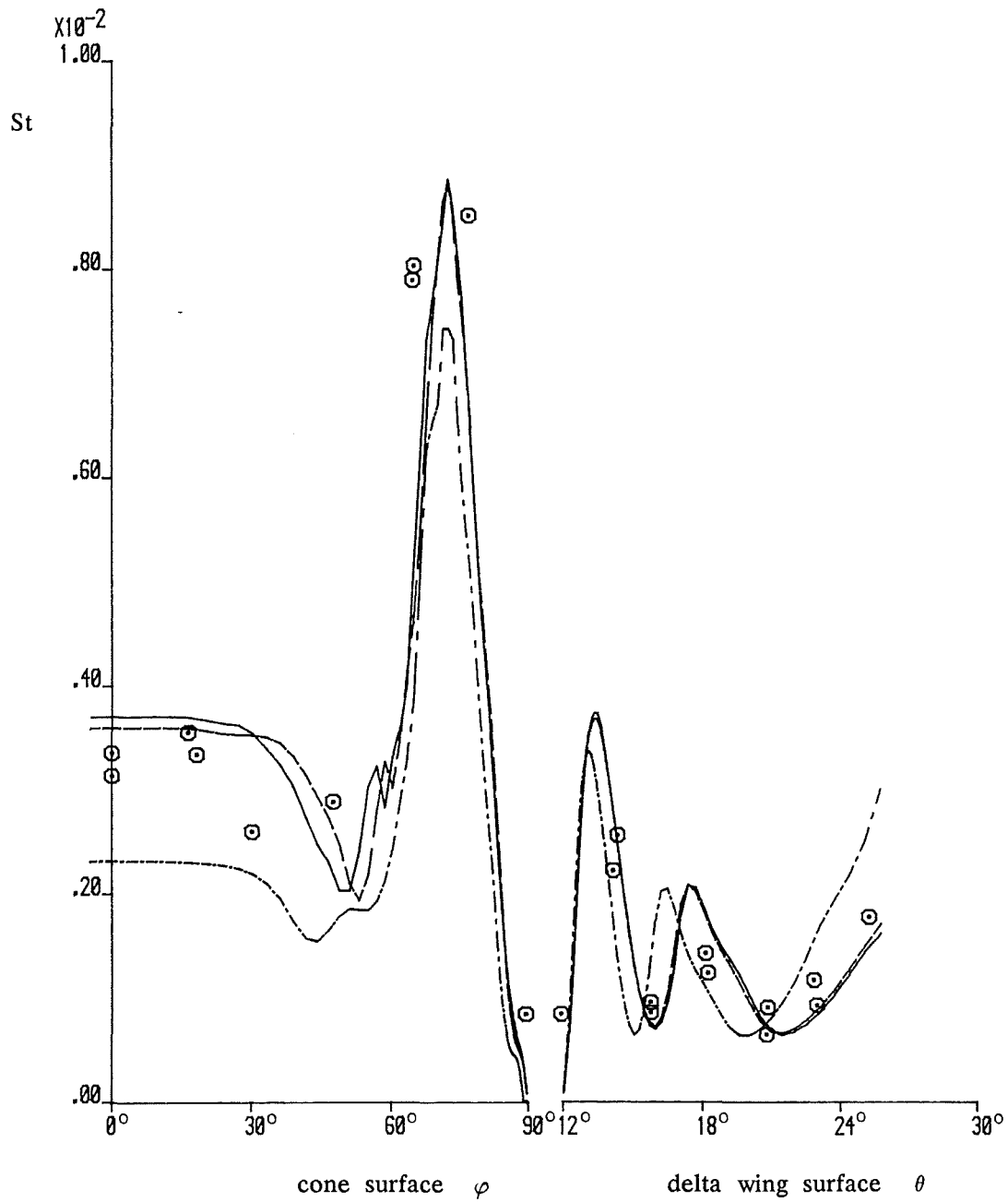
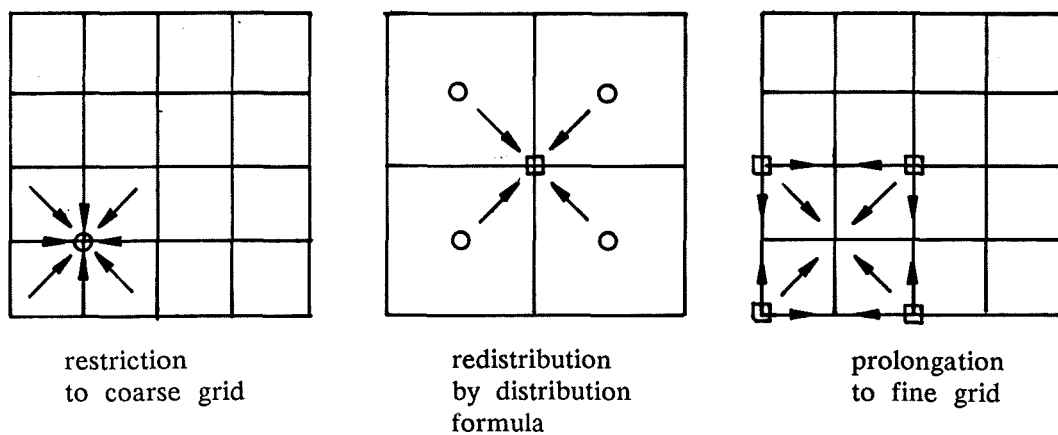
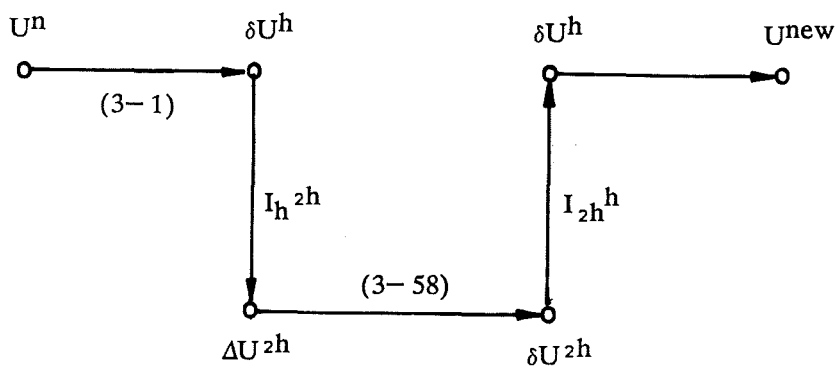


Fig. 3.1 Comparison of Heat Transfer Distribution  
Cone-delta wing combination case,  $\alpha = 0^\circ$

- simplified B-W implicit
- - - MacCormack implicit,  $\Delta t_{\text{final}} = 0.001$
- · - · MacCormack implicit,  $\Delta t_{\text{final}} = 0.005$
- ⊙ experimental data



(a)



(b)

Fig. 3.2 Ni- type Multigrid Acceleration of MacCormack Implicit Scheme

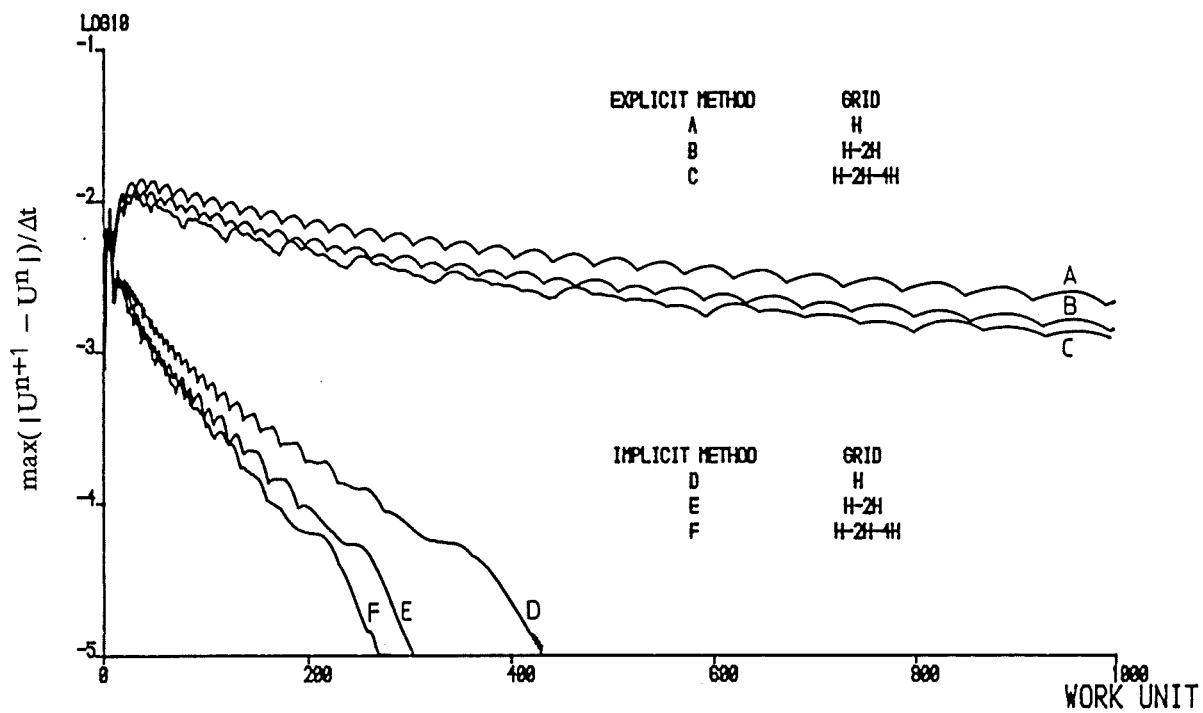
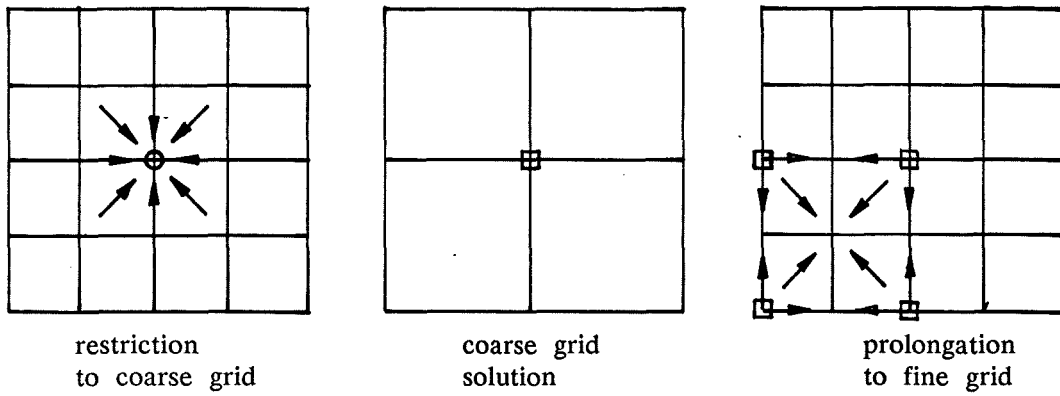
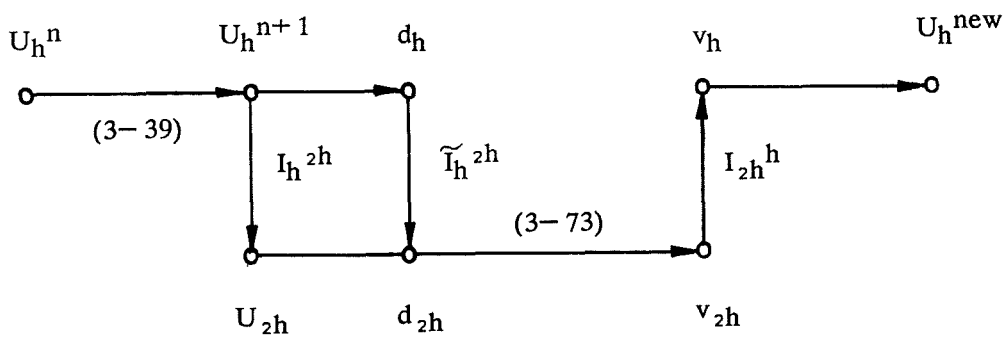


Fig. 3.3 Convergence Histories of MacCormack Explicit and Implicit Schemes with and without Multigrid Acceleration



(a)



(b)

Fig. 3.4 FAS Multigrid Acceleration of the Simplified Beam-Warming Implicit Scheme

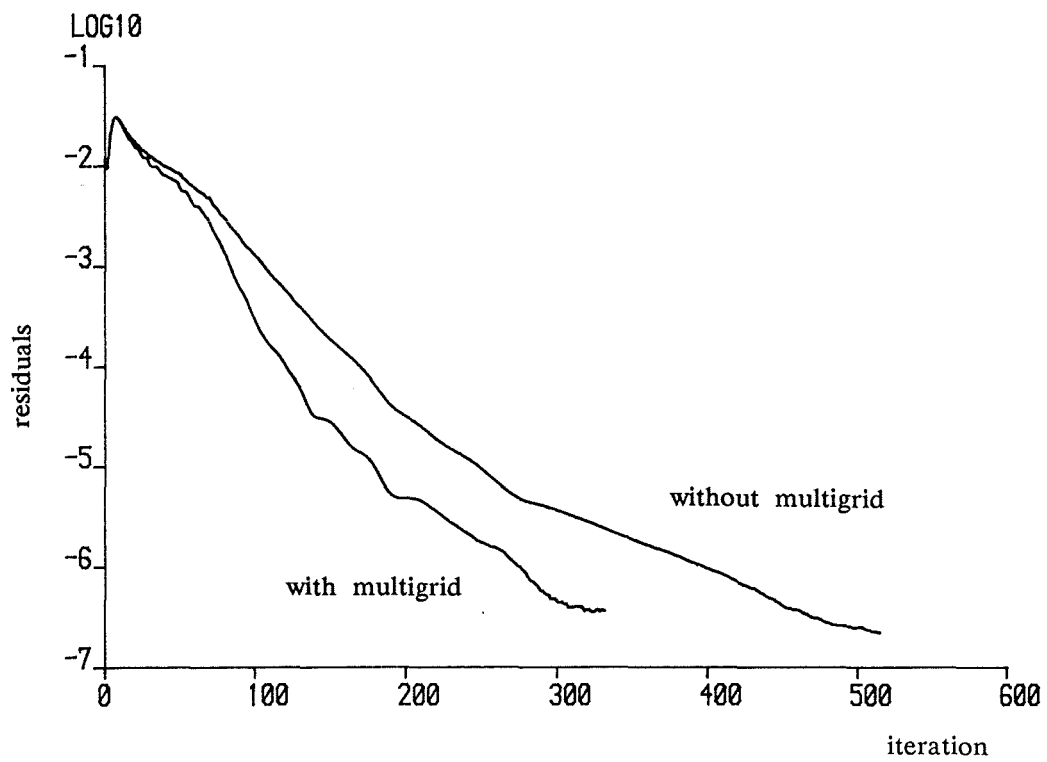


Fig. 3.5 Convergence Histories of the Simplified Beam-Warming Implicit Scheme with and without Multigrid Acceleration

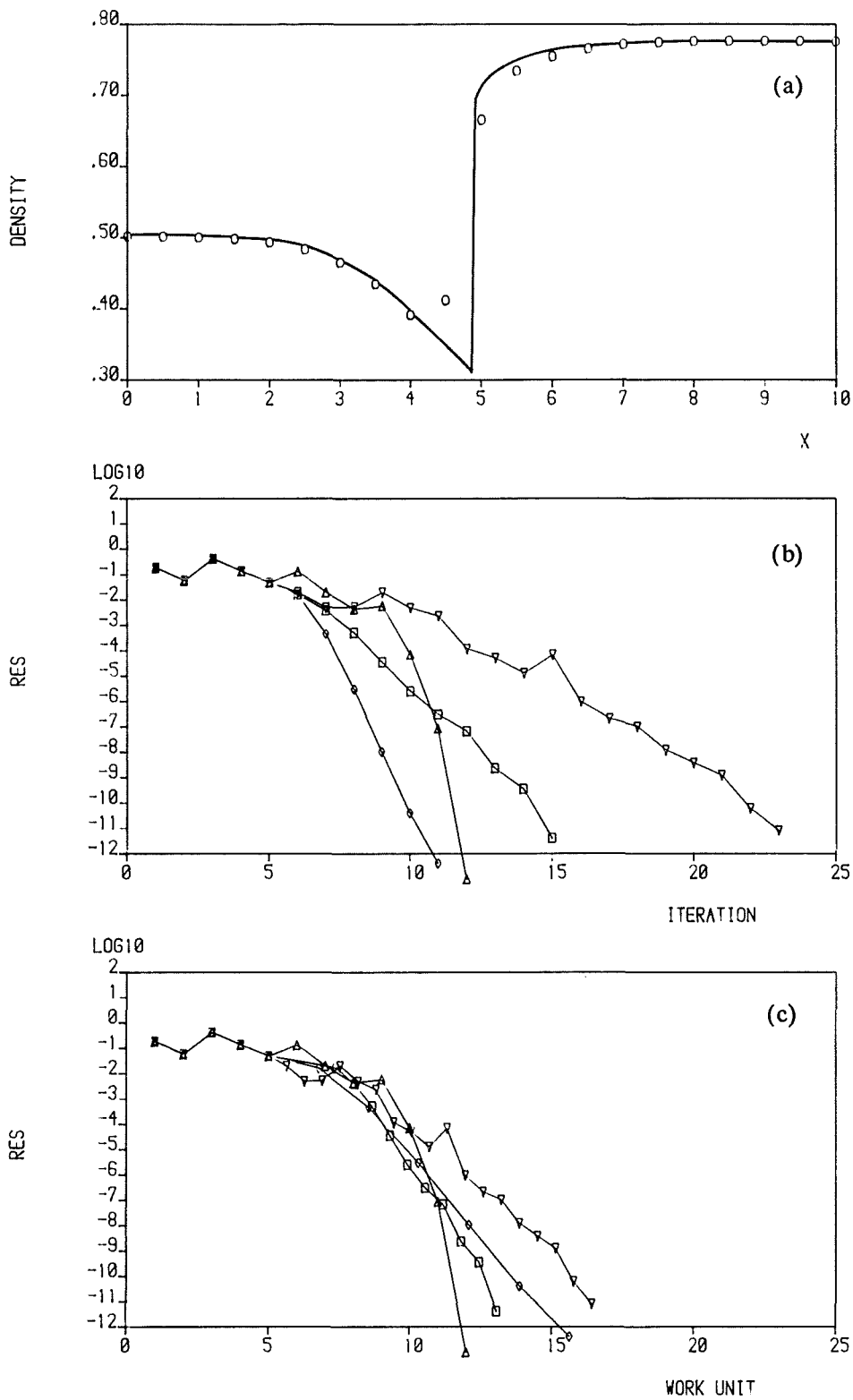


Fig. 3.6 First-Order Flux Splitting — Results of Nozzle Problem

- (a) density distribution; — exact;  $\circ$  numerical  
 (b) convergence against iteration number  
 (c) convergence against work unit

- $\triangle$  implicit
- $\square$  sparse quasi-Newton with sparse FD Newton Jacobian initialization
- $\nabla$  sparse quasi-Newton with implicit operator as initial Jacobian
- $\diamond$  sparse FD Newton

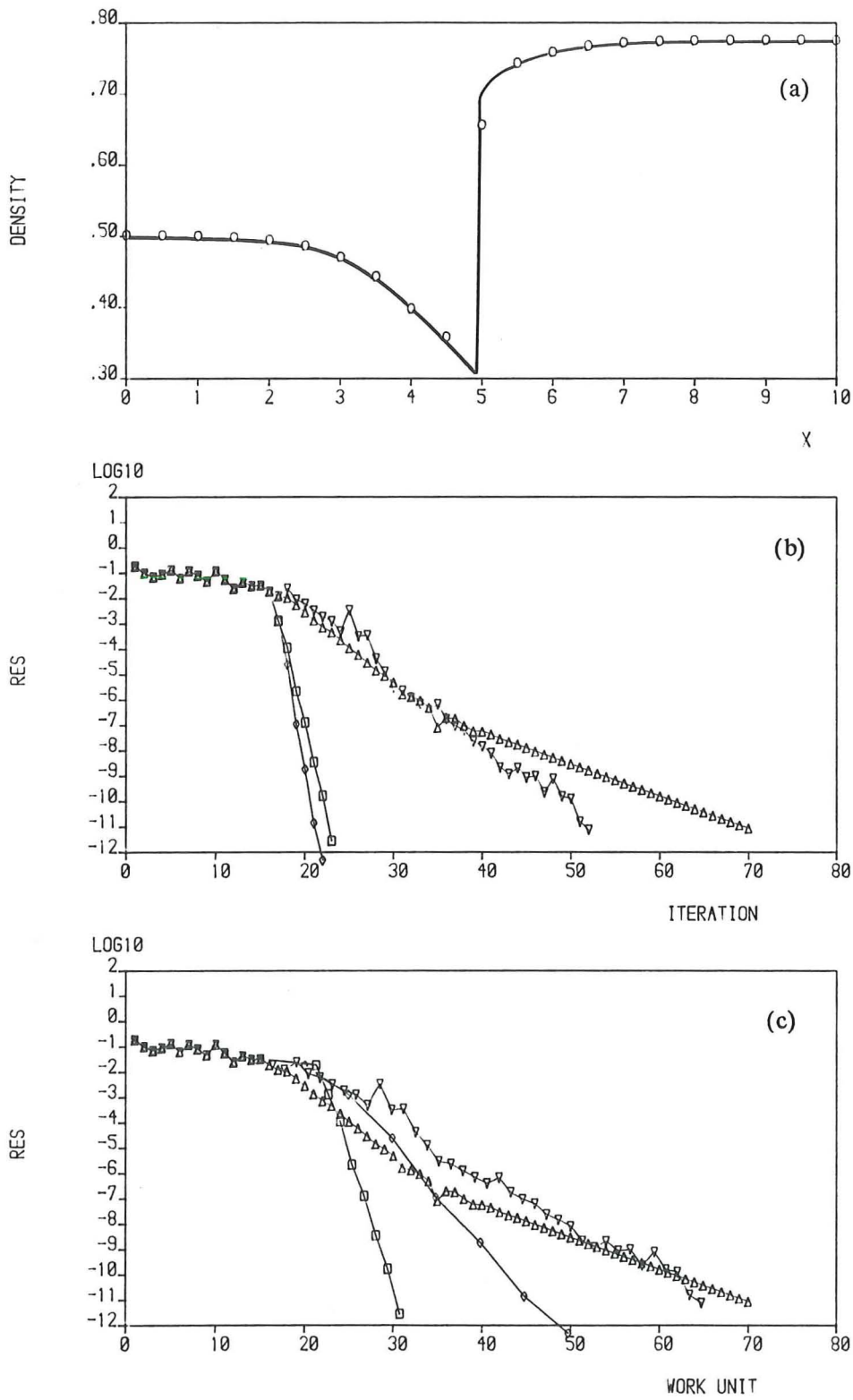


Fig. 3.7 Second Order Flux Splitting — Results of Nozzle Problem

(a) density distribution; — exact;  $\circ$  numerical

(b) convergence against iteration number

(c) convergence against work unit

$\triangle$  implicit

$\square$  sparse quasi-Newton with sparse FD Newton Jacobian initialization

$\nabla$  sparse quasi-Newton with implicit operator as initial Jacobian

$\diamond$  sparse FD Newton

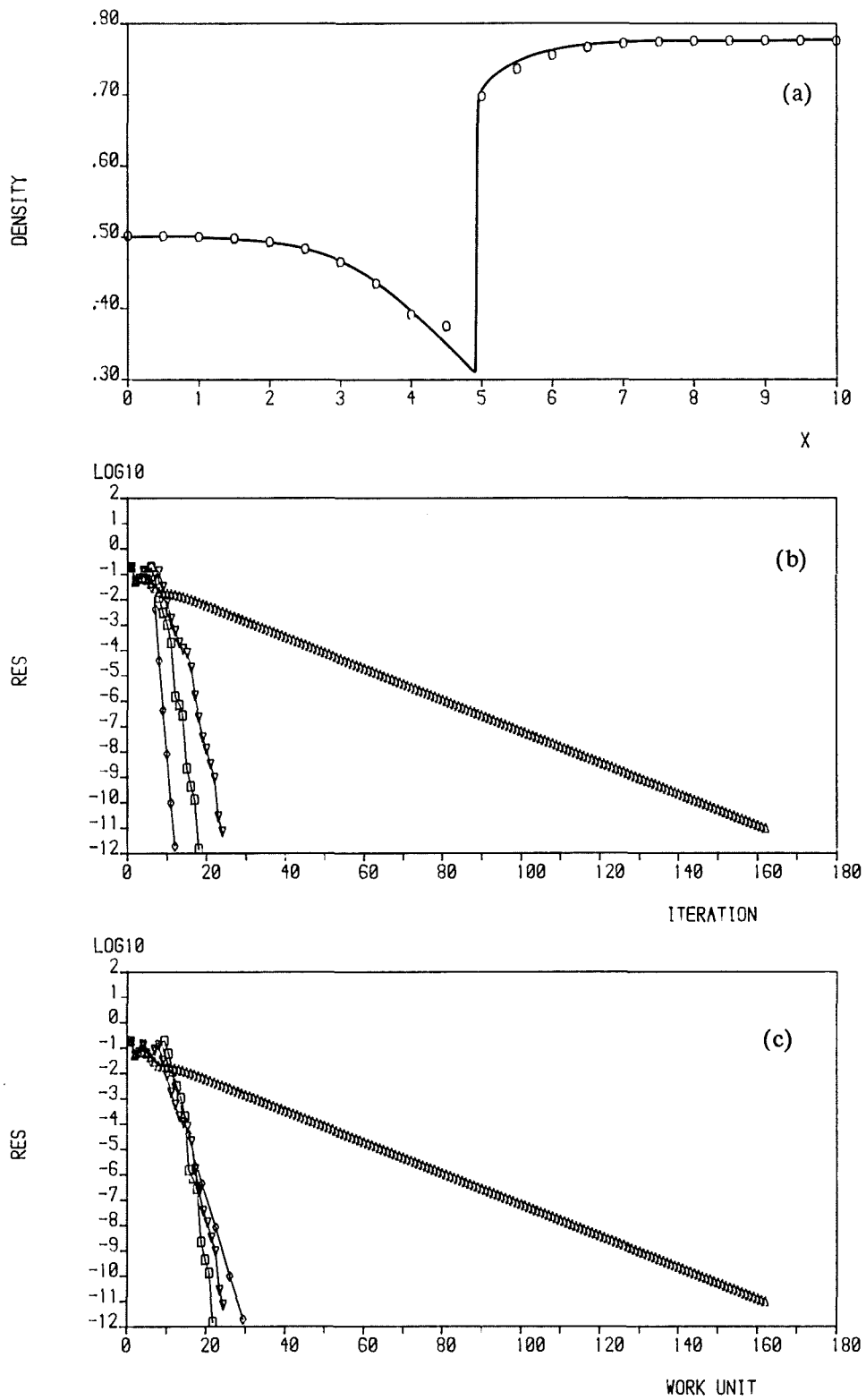


Fig. 3.8 First Order TVD — Results of Nozzle Problem

- (a) density distribution; — exact;  $\circ$  numerical  
 (b) convergence against iteration number  
 (c) convergence against work unit

- $\triangle$  implicit
- $\square$  sparse quasi-Newton with sparse FD Newton Jacobian initialization
- $\nabla$  sparse quasi-Newton with implicit operator as initial Jacobian
- $\diamond$  sparse FD Newton

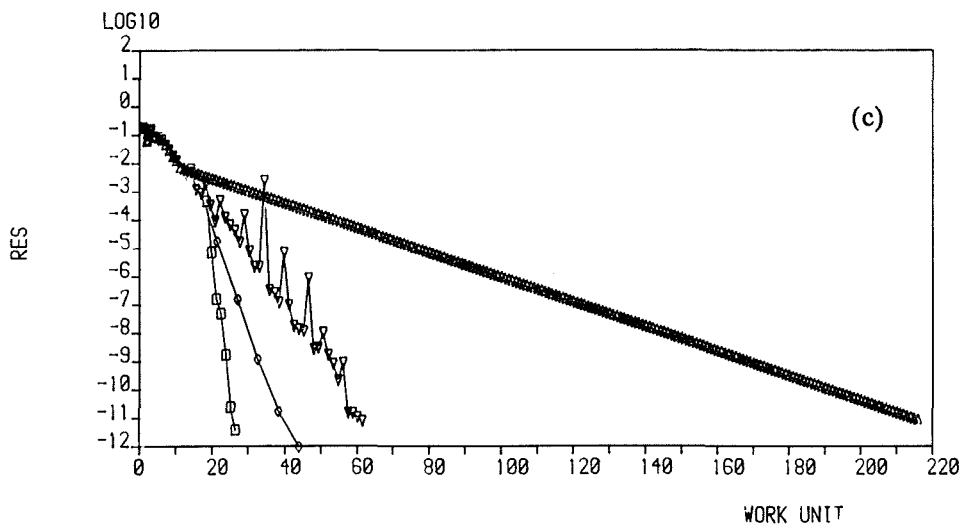
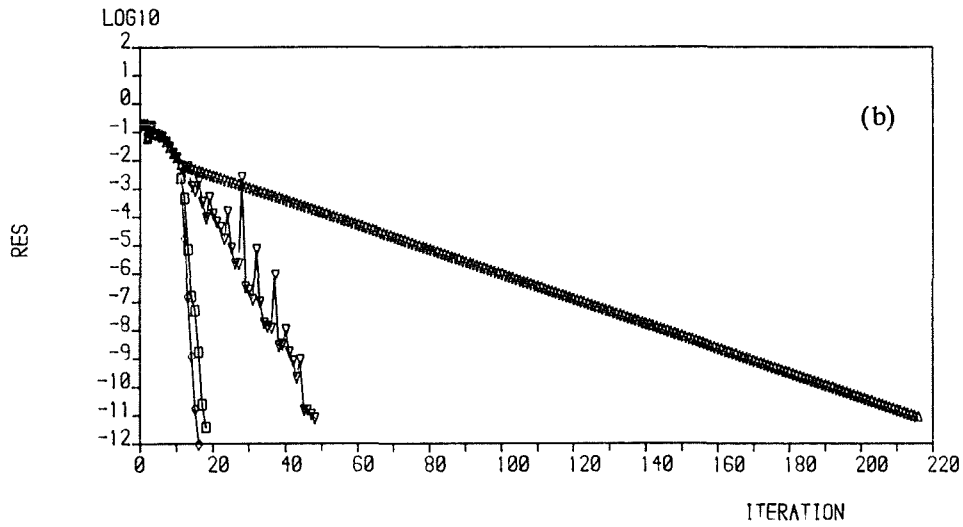
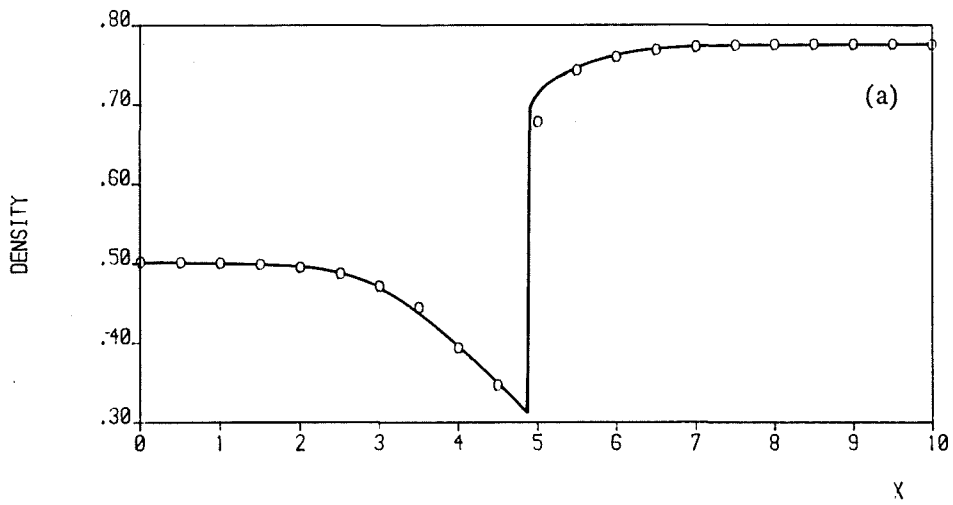


Fig. 3.9 Second Order TVD — Results of Nozzle Problem

(a) density distribution; — exact;  $\circ$  numerical

(b) convergence against iteration number

(c) convergence against work unit

$\triangle$  implicit

$\square$  sparse quasi-Newton with sparse FD Newton Jacobian initialization

$\nabla$  sparse quasi-Newton with implicit operator as initial Jacobian

$\diamond$  sparse FD Newton

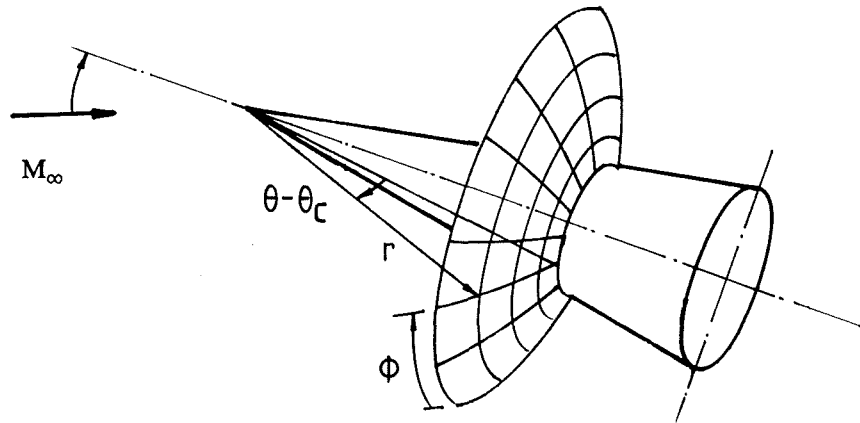


Fig. 4.1 Cone Geometry and Solution Surface

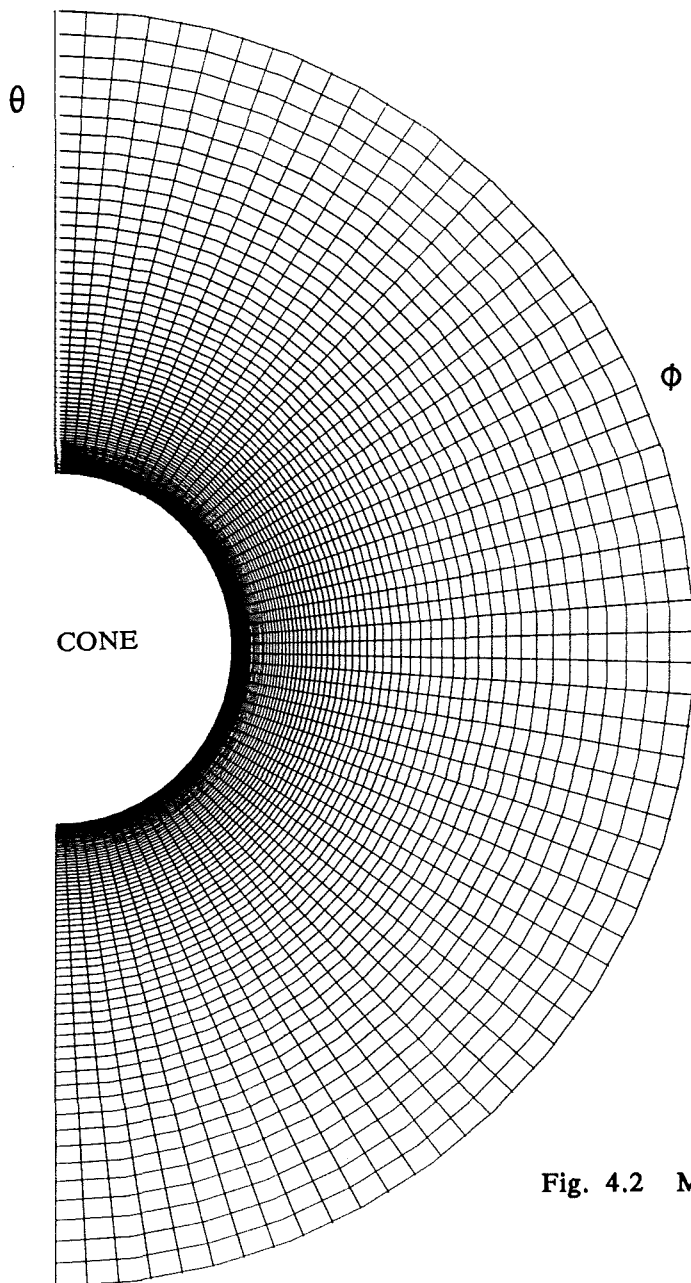


Fig. 4.2 Mesh System for Cone Case

Fig.4.3 Results for Cone Case at  $\alpha = 12^\circ$   
 (a) Crossflow Velocity – Overall View

- experimental shock position
- ▲ experimental separation point
- △ computed separation point

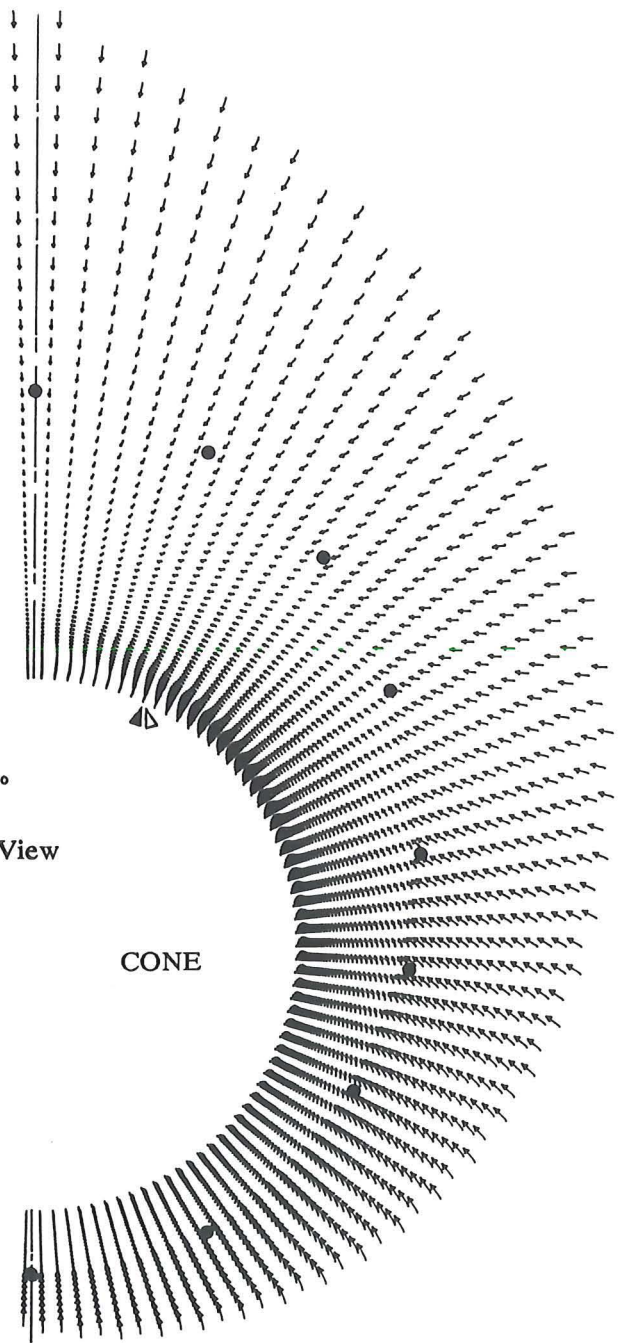
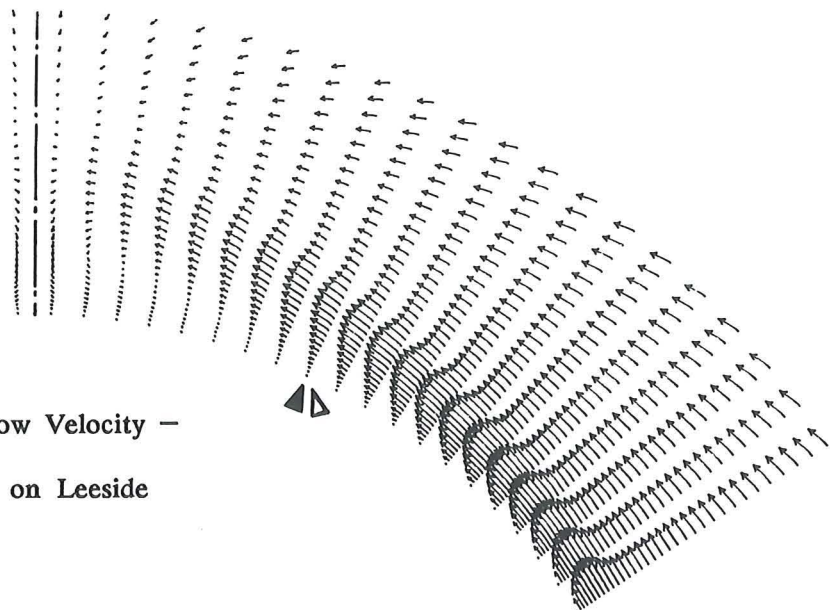


Fig. 4.3(b) Crossflow Velocity –  
 Details on Leaside



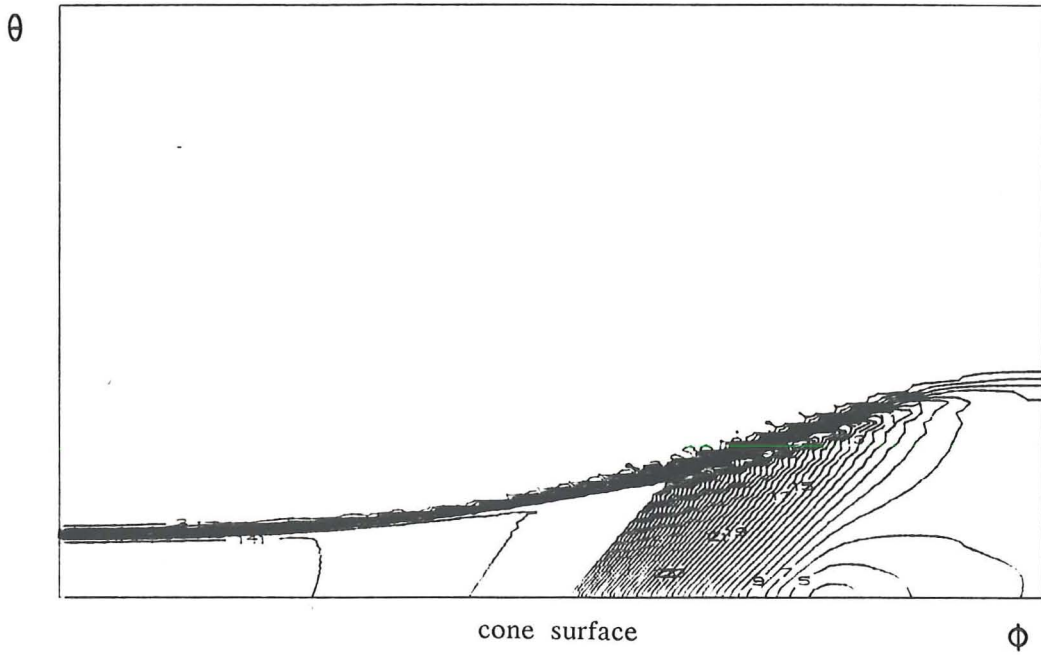


Fig. 4.3(c) Pressure Contours

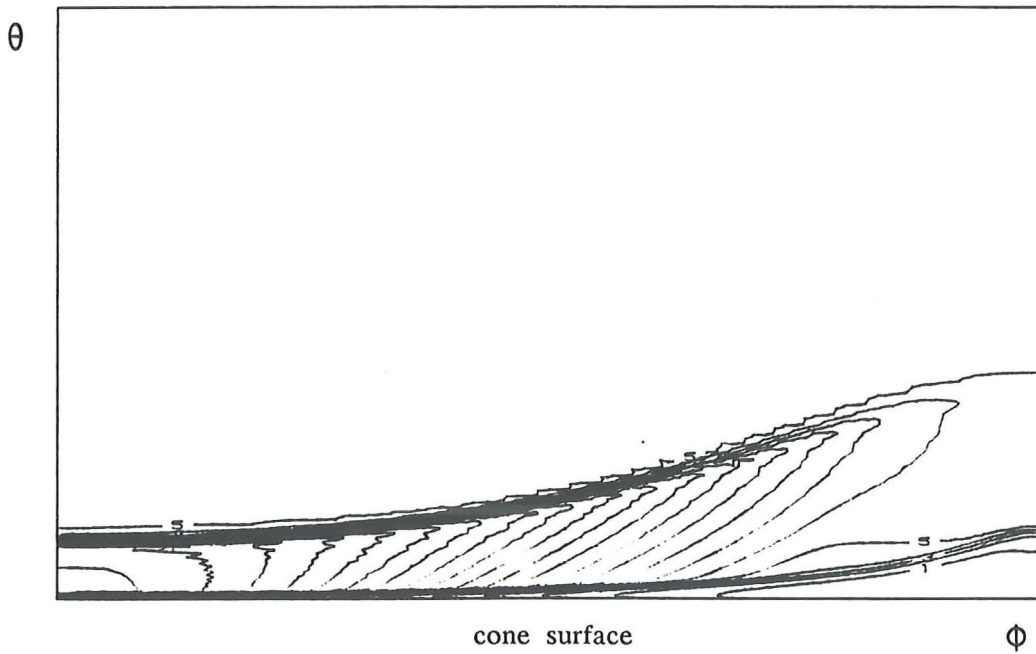


Fig. 4.3(d) Density Contours

Fig.4.4 Results for Cone Case at  $\alpha = 24^\circ$   
 (a) Crossflow Velocity – Overall View

- experimental shock position
- ▲ experimental separation point
- △ computed separation point

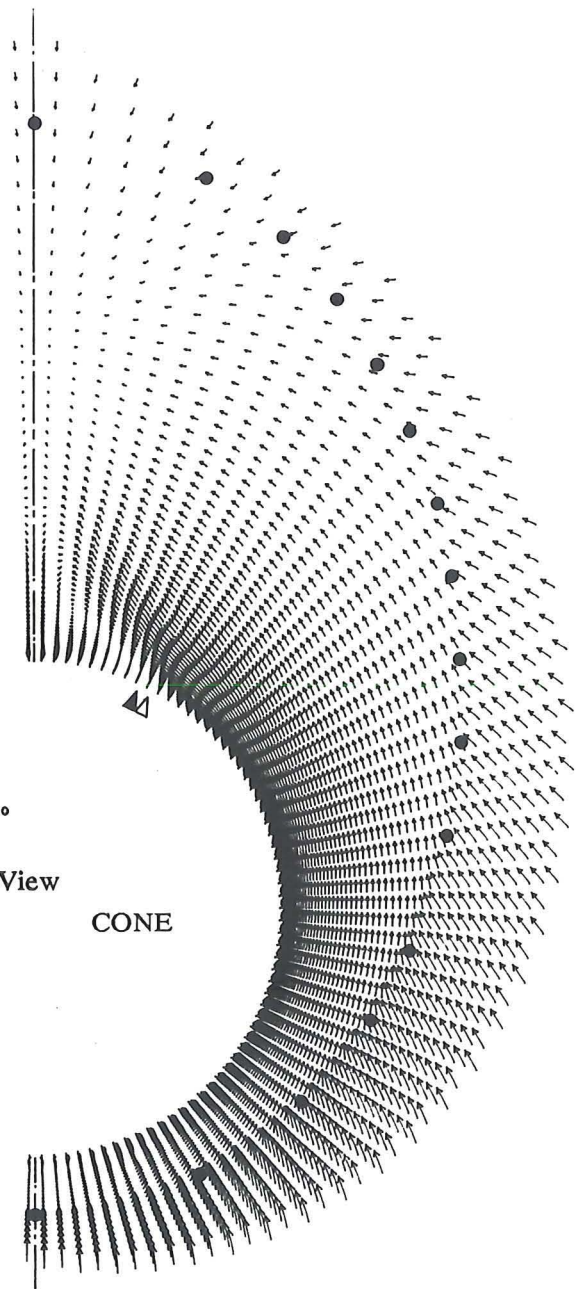
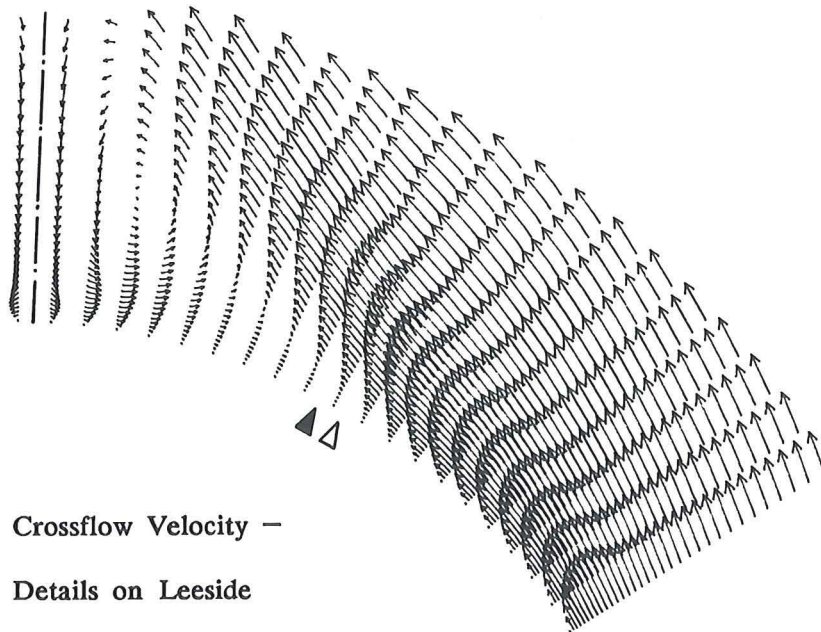


Fig. 4.4(b) Crossflow Velocity –  
 Details on Leaside



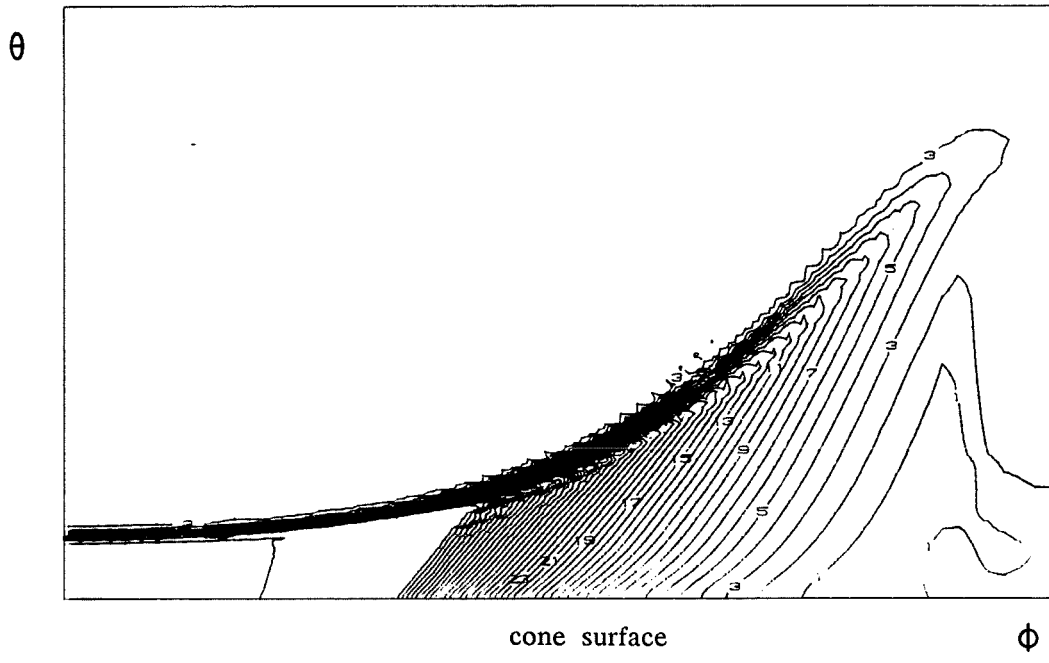


Fig. 4.4(c) Pressure Contours

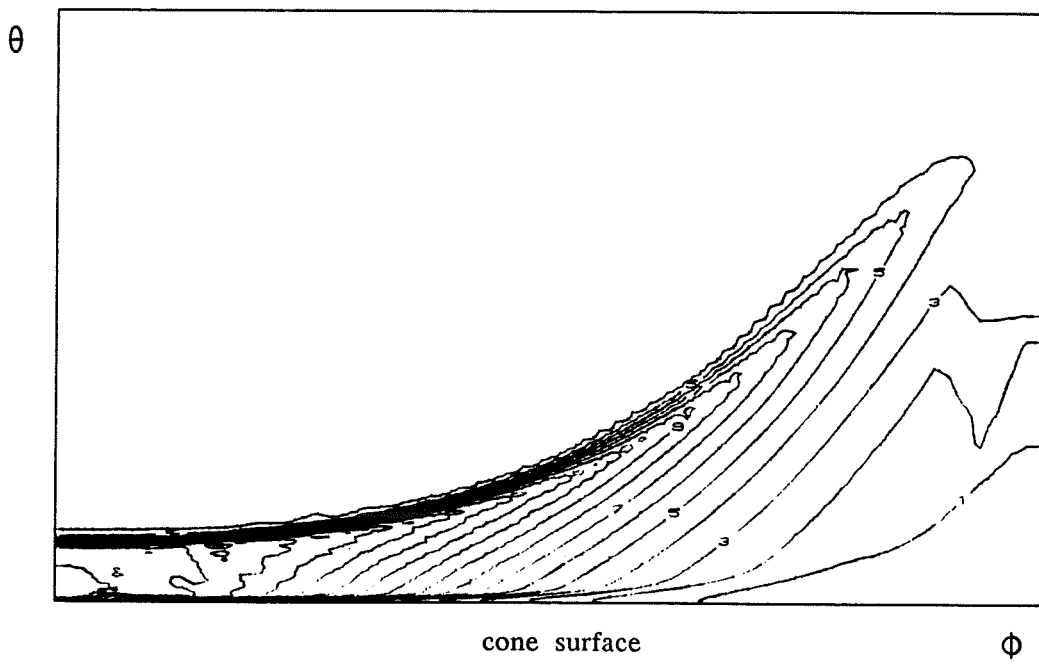


Fig. 4.4(d) Density Contours

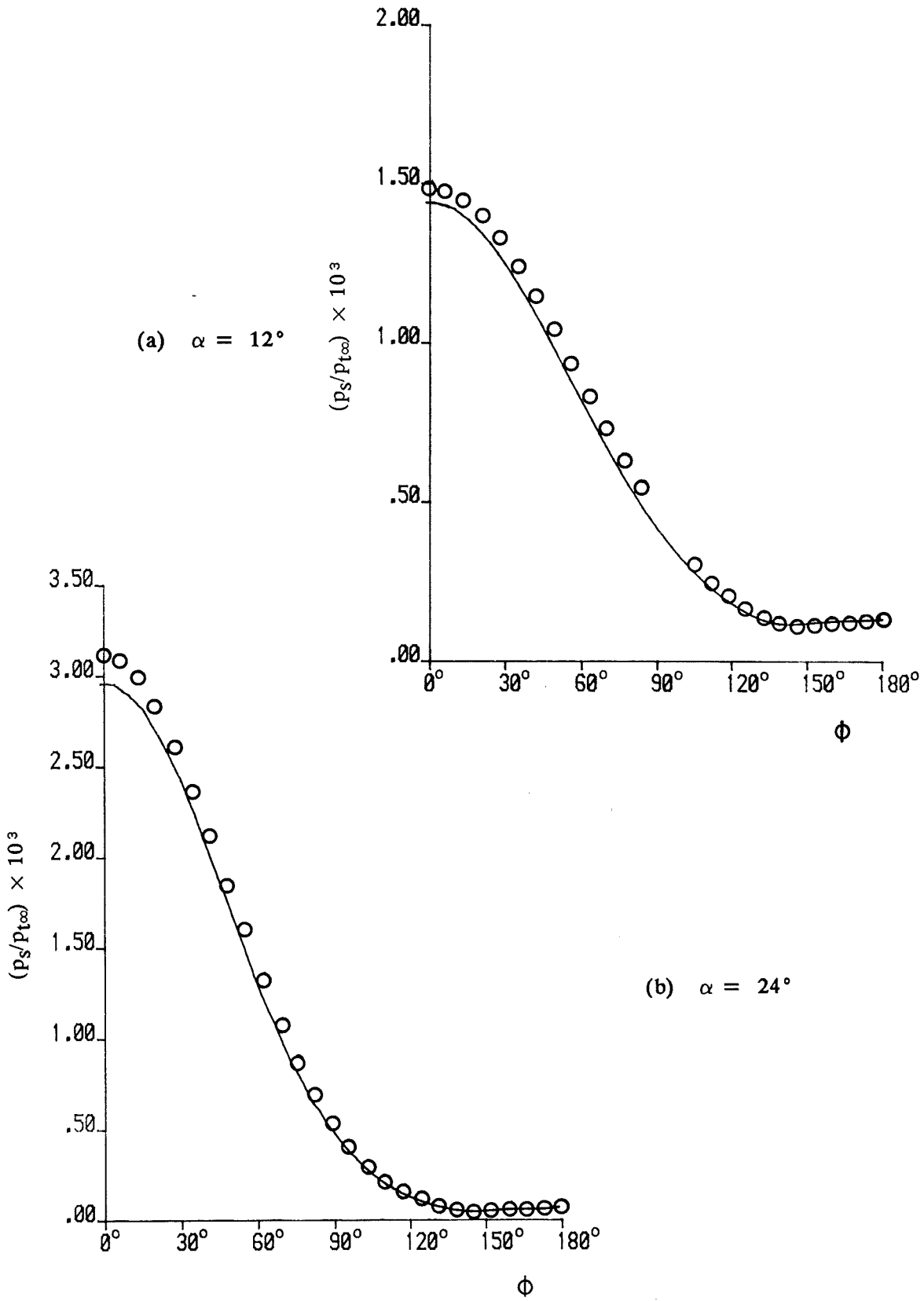


Fig. 4.5 Comparison of Cone Surface Pressure

○ experimental data  
 — computational results

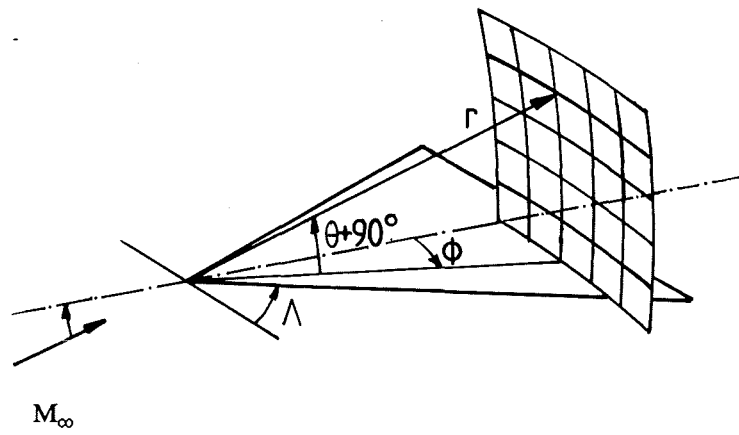


Fig. 4.6 Delta Wing Geometry and Solution Surface

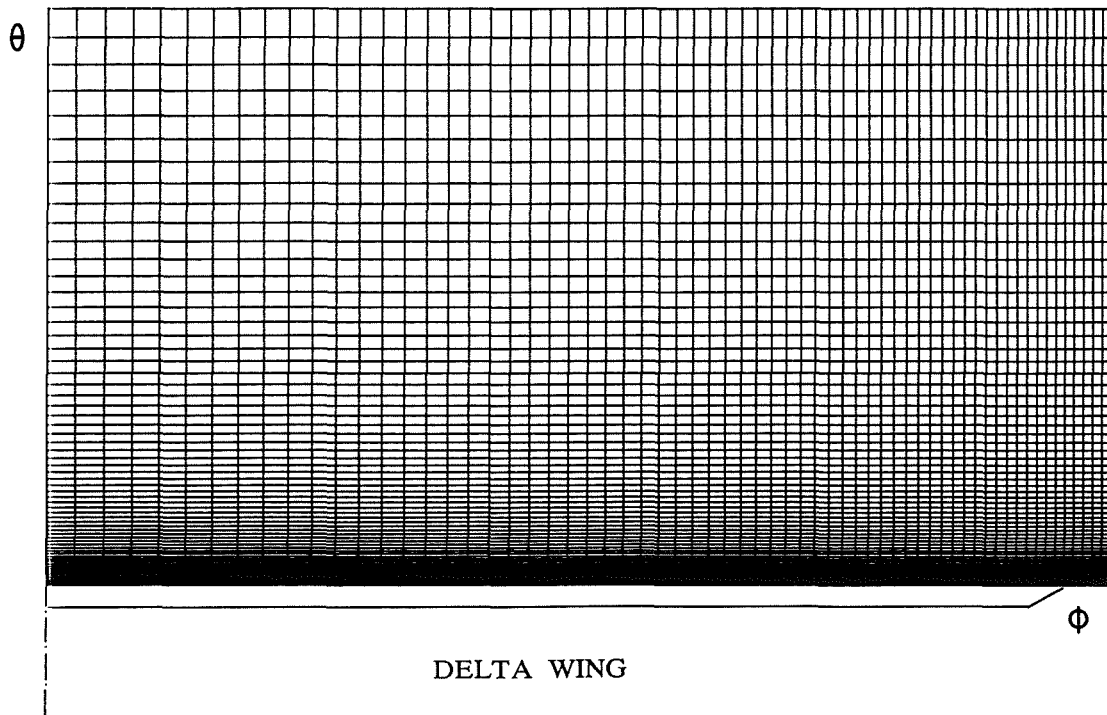
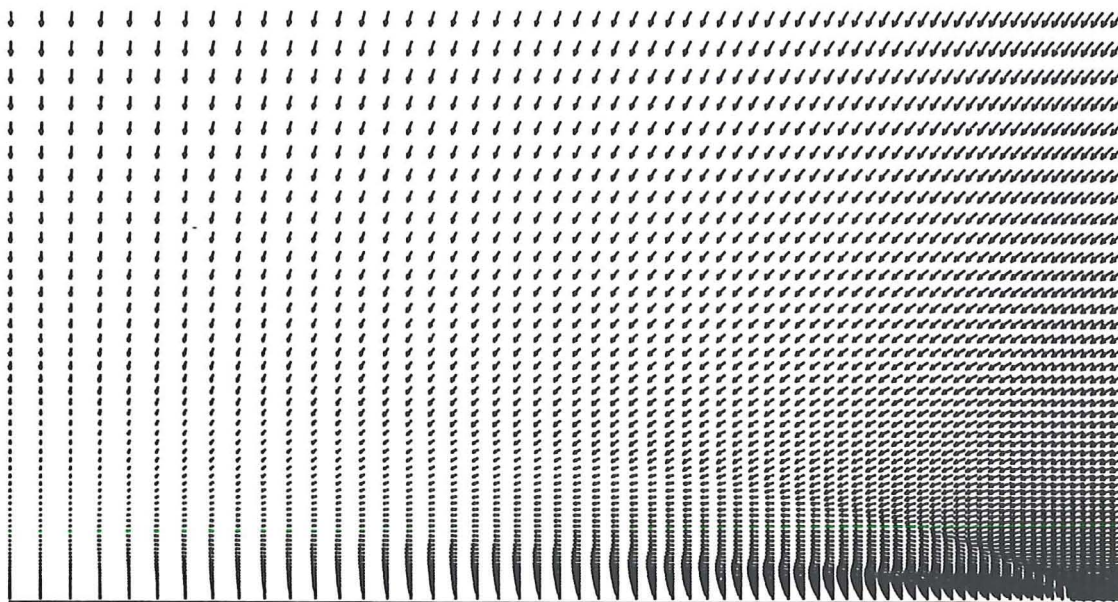


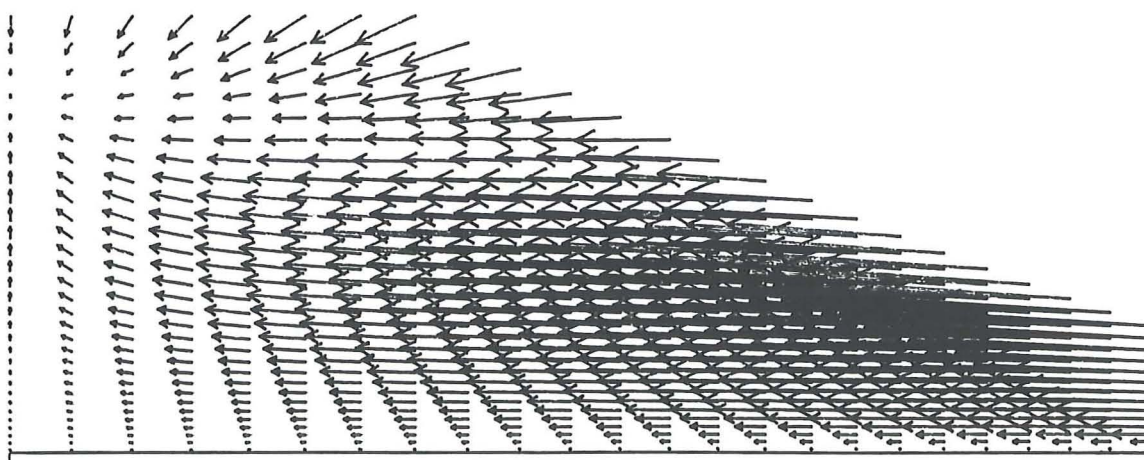
Fig. 4.7 Mesh System for Delta Wing Case



DELTA WING

Fig. 4.8 Results for Delta Wing Case at  $\alpha = 0^\circ$

(a) Crossflow Velocity - Overall View



DELTA WING

Fig. 4.8(b) Crossflow Velocity - Details near Central Line

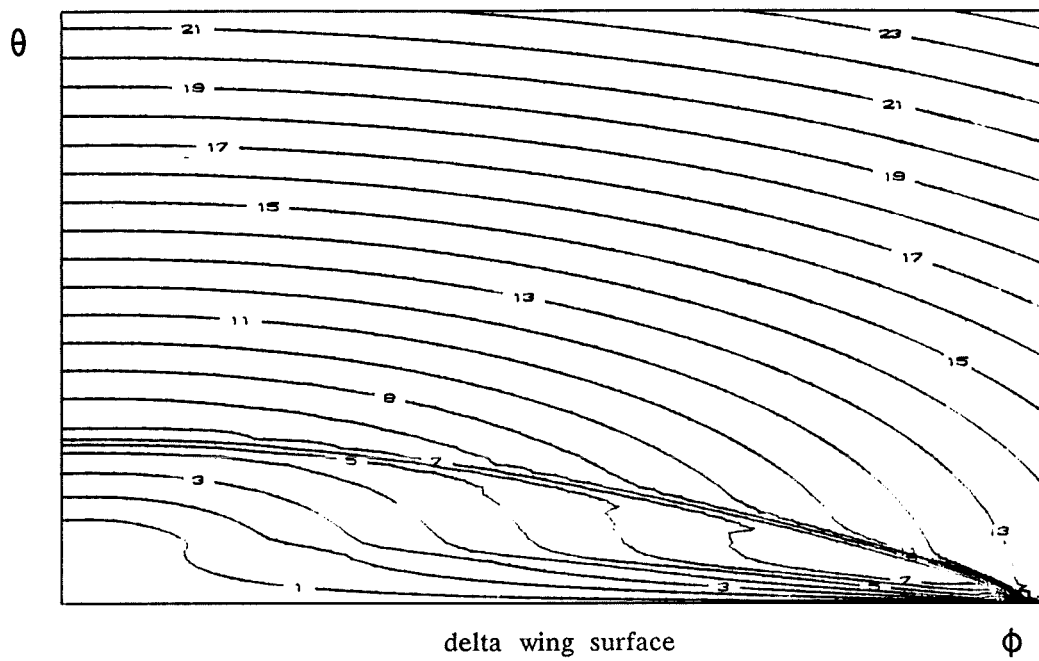


Fig. 4.8(c) Crossflow Mach Number Contours

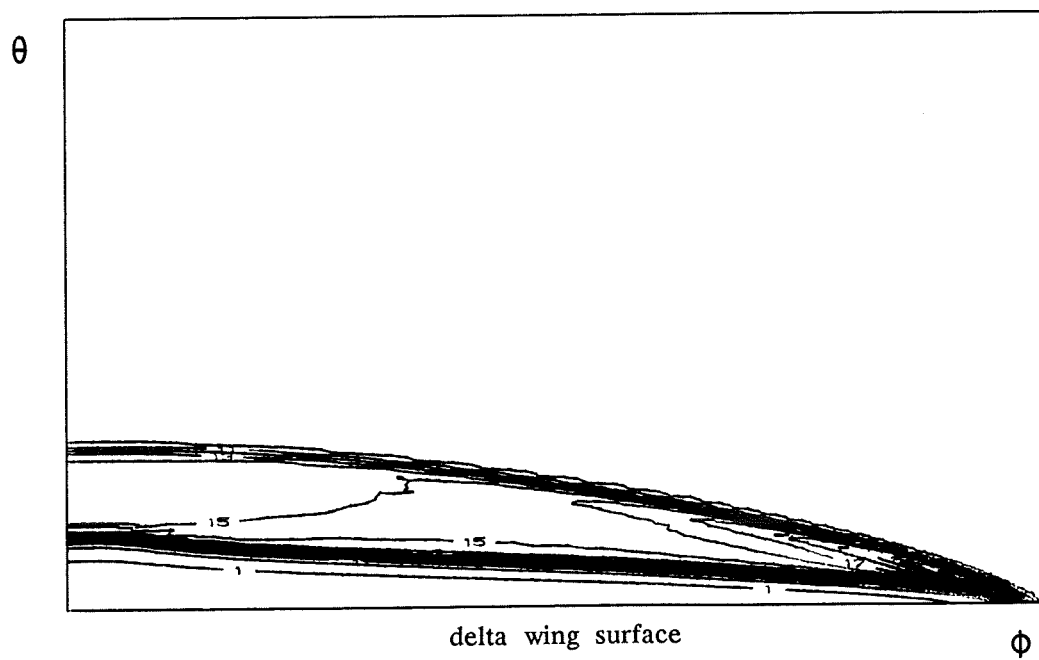


Fig. 4.8(d) Density Contours

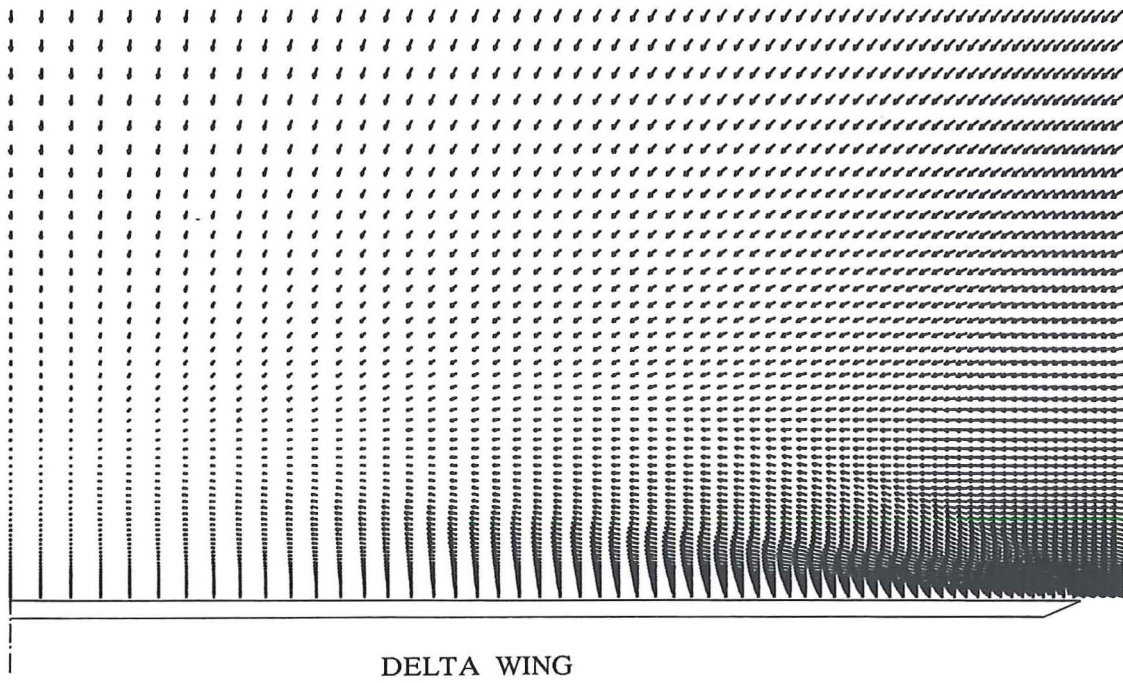


Fig. 4.9 Results for Delta Wing Case at  $\alpha = 5^\circ$

(a) Crossflow Velocity - Overall View

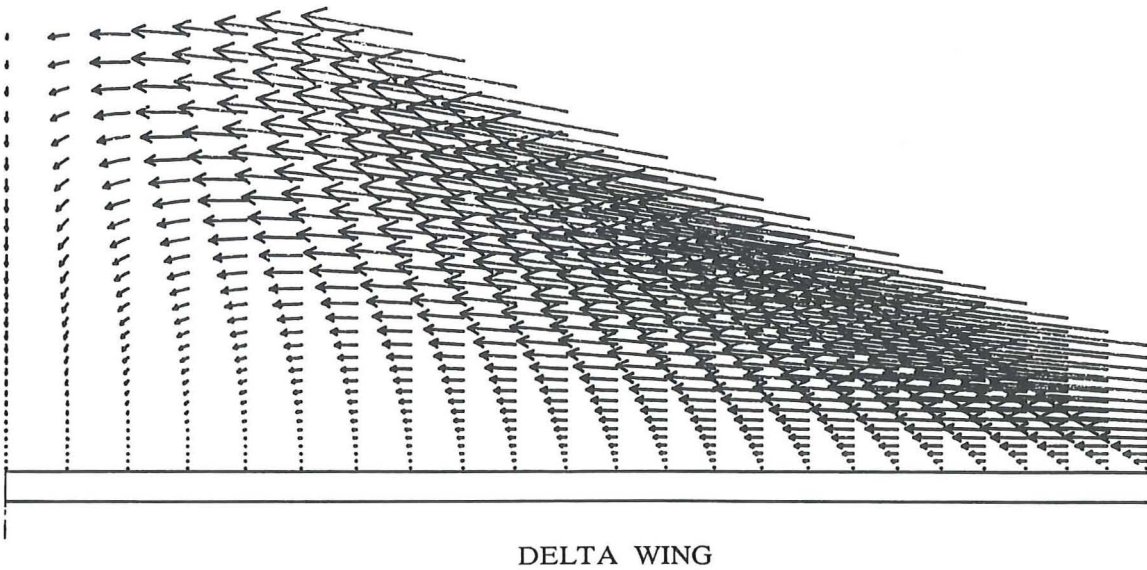


Fig. 4.9(b) Crossflow Velocity - Details near Central Line

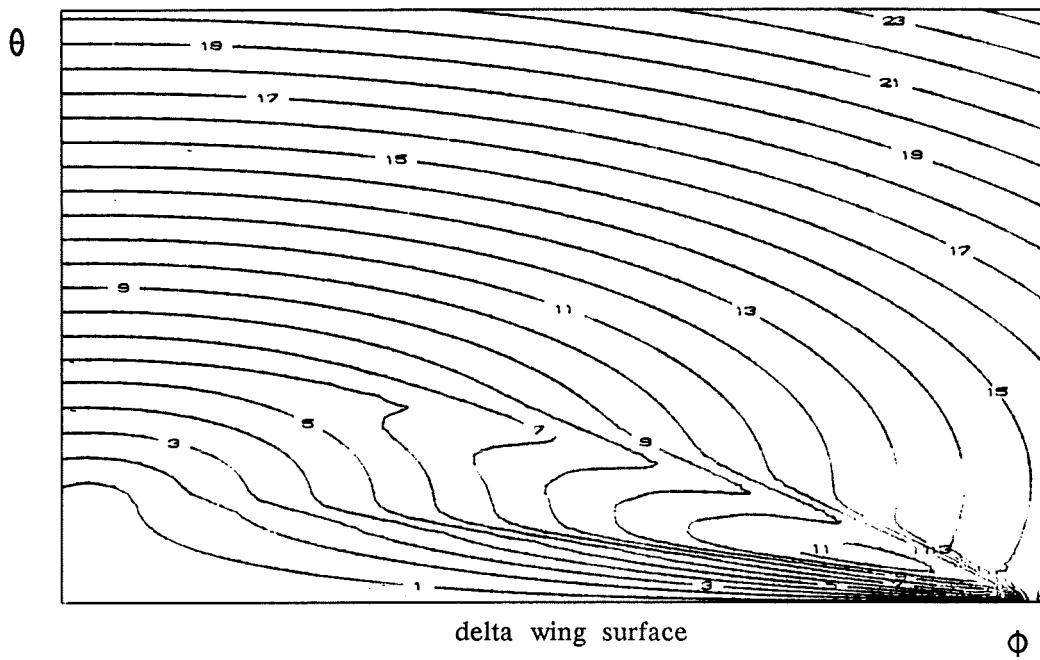


Fig. 4.9(c) Crossflow Mach Number Contours

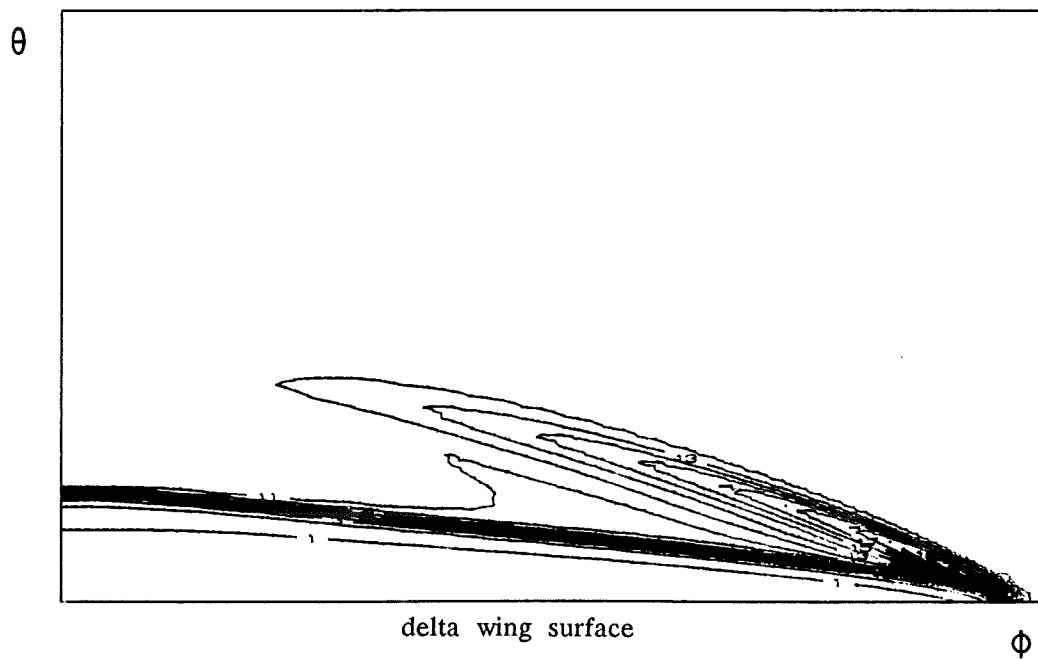


Fig. 4.9(d) Density Contours

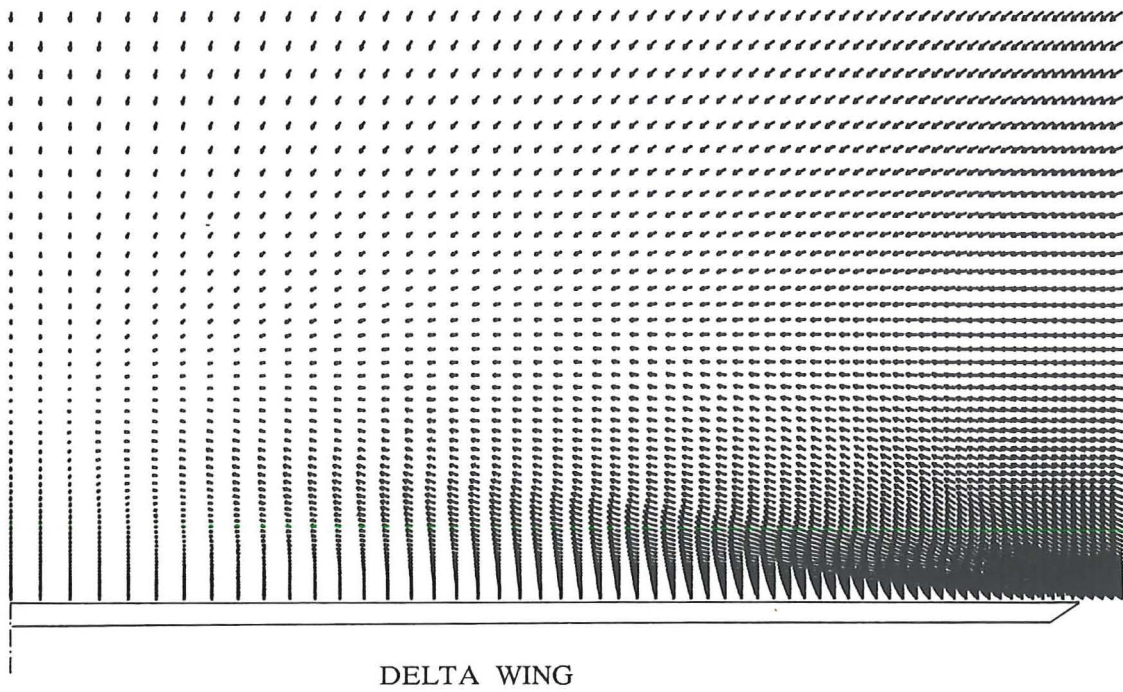


Fig. 4.10 Results for Delta Wing Case at  $\alpha = 9^\circ$

(a) Crossflow Velocity - Overall View

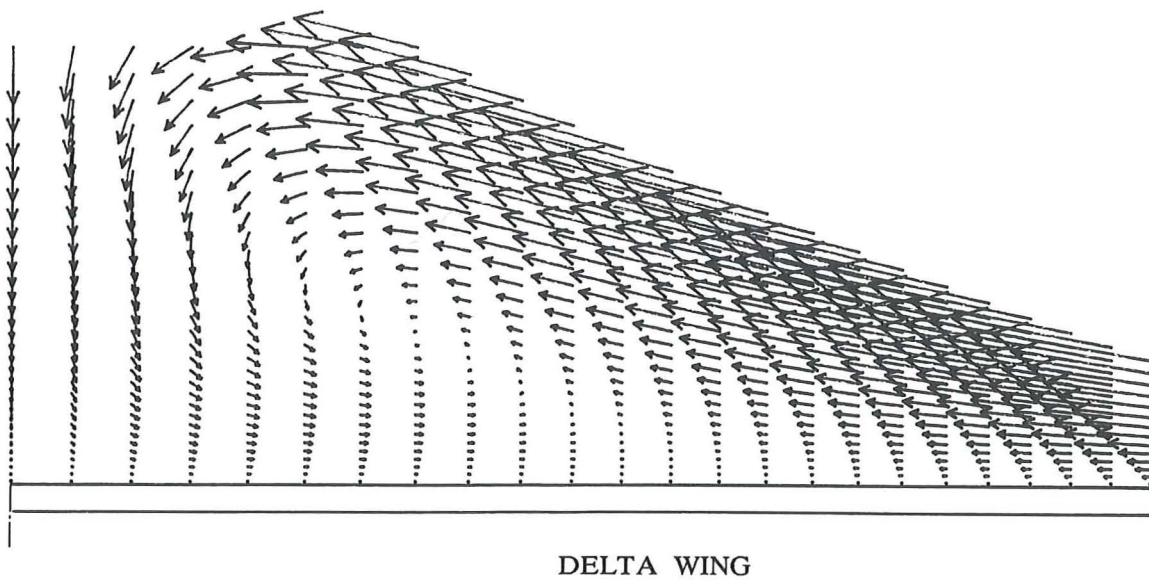


Fig. 4.10(b) Crossflow Velocity - Details near Central Line

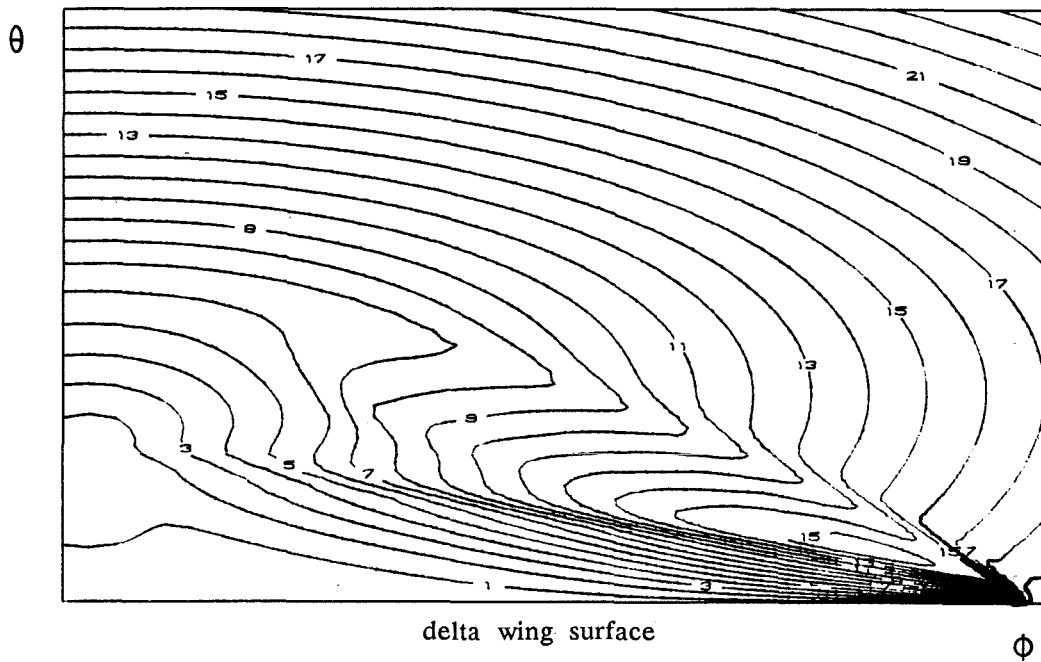


Fig. 4.10(c) Crossflow Mach Number Contours

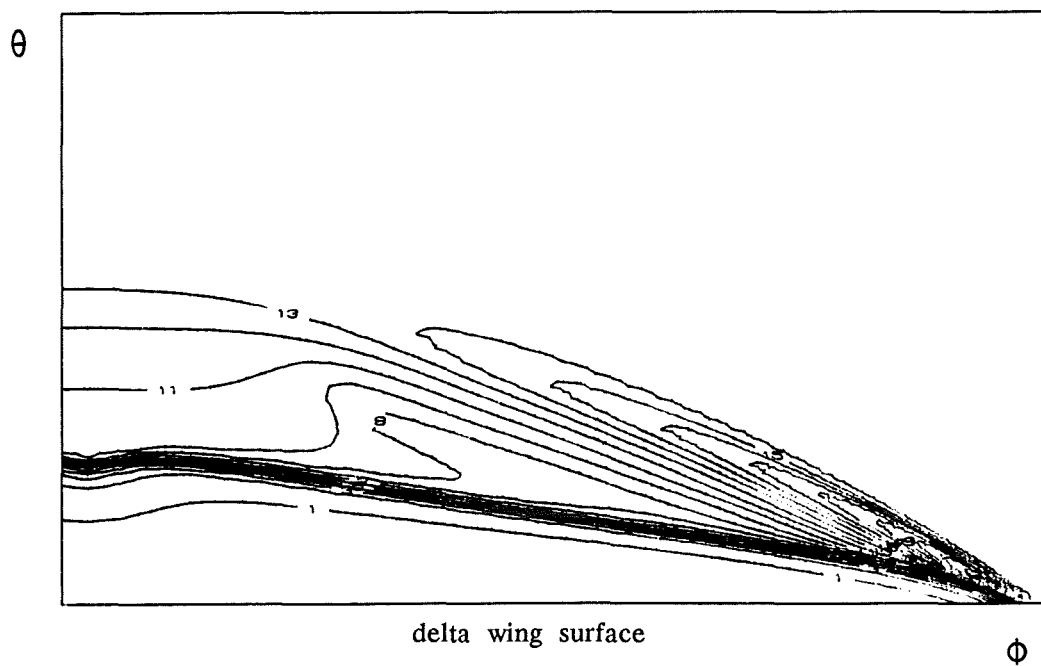


Fig. 4.10(d) Density Contours

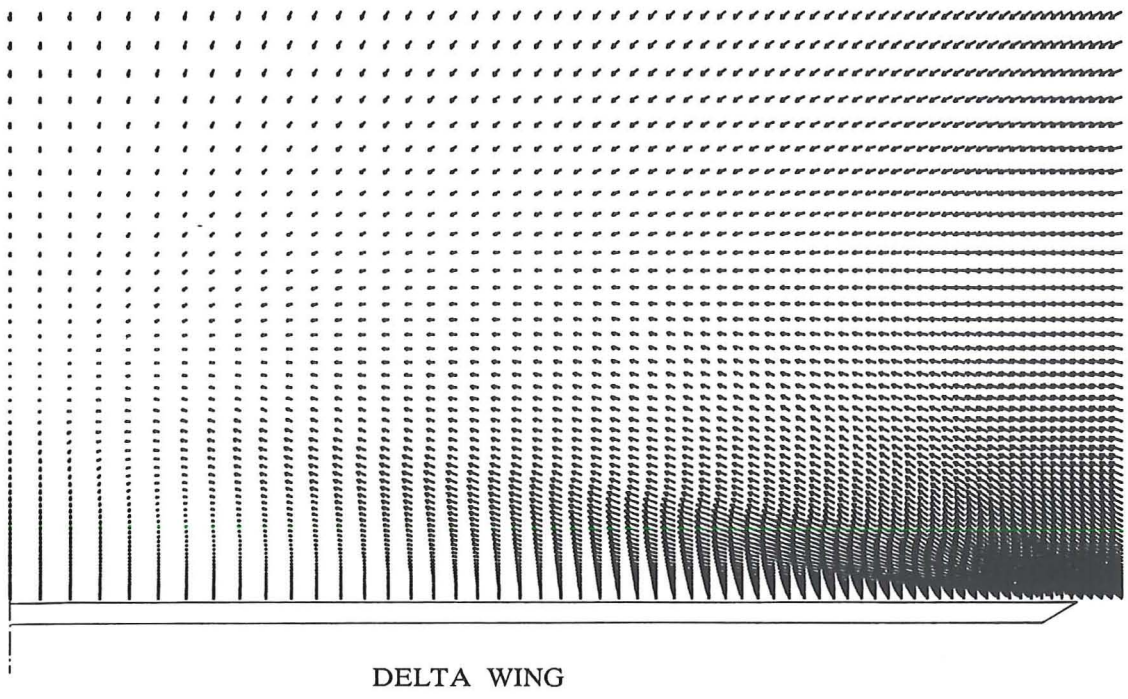


Fig. 4.11 Results for Delta Wing Case at  $\alpha = 11^\circ$

(a) Crossflow Velocity - Overall View

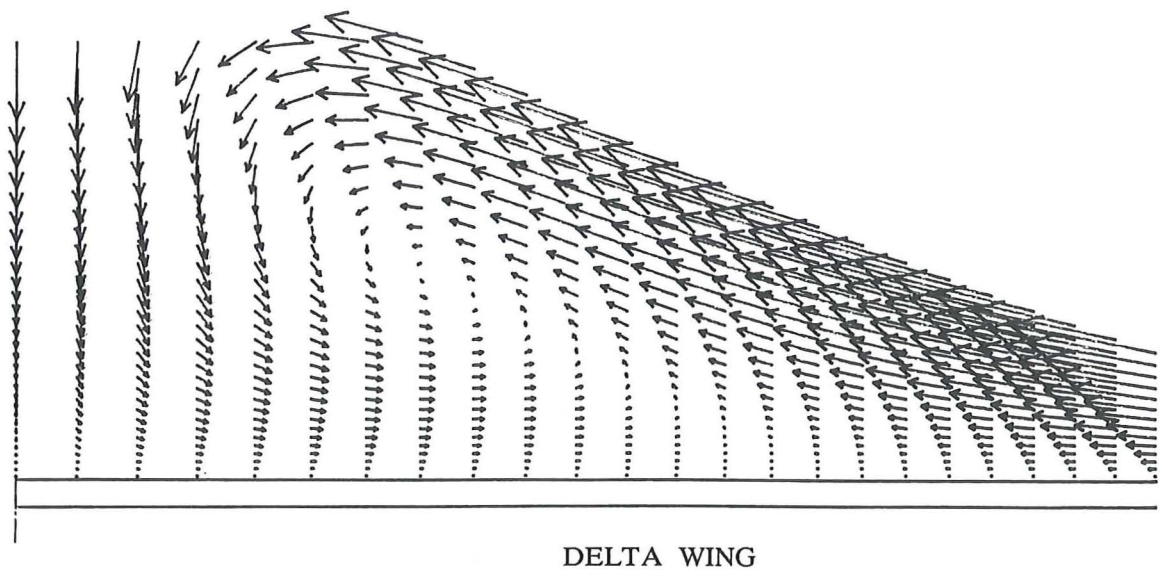


Fig. 4.11(b) Crossflow Velocity - Details near Central Line

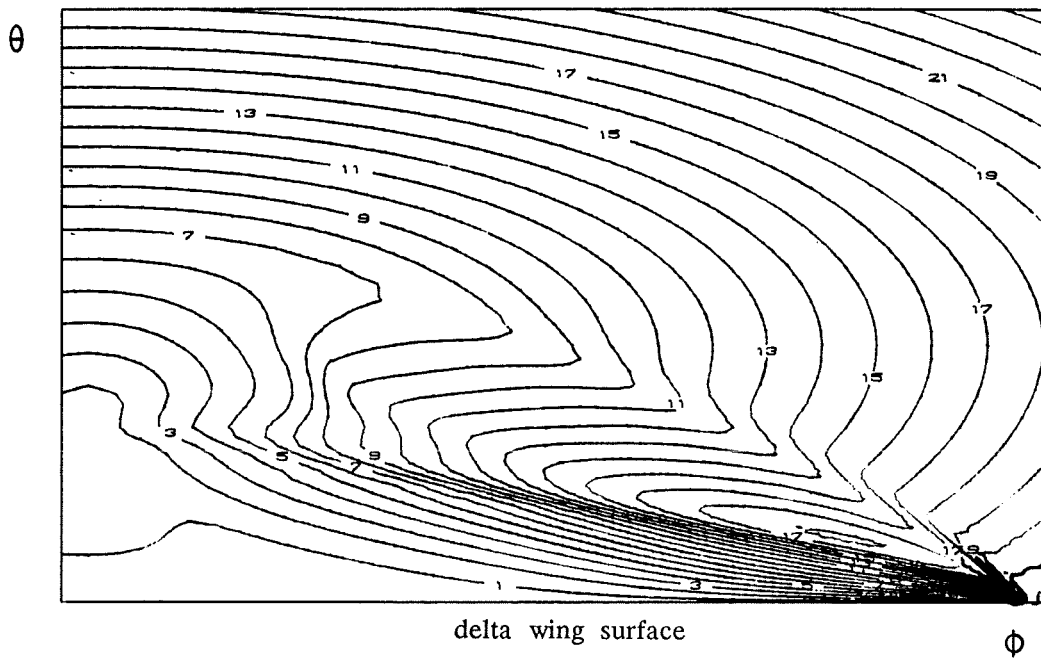


Fig. 4.11(c) Crossflow Mach Number Contours

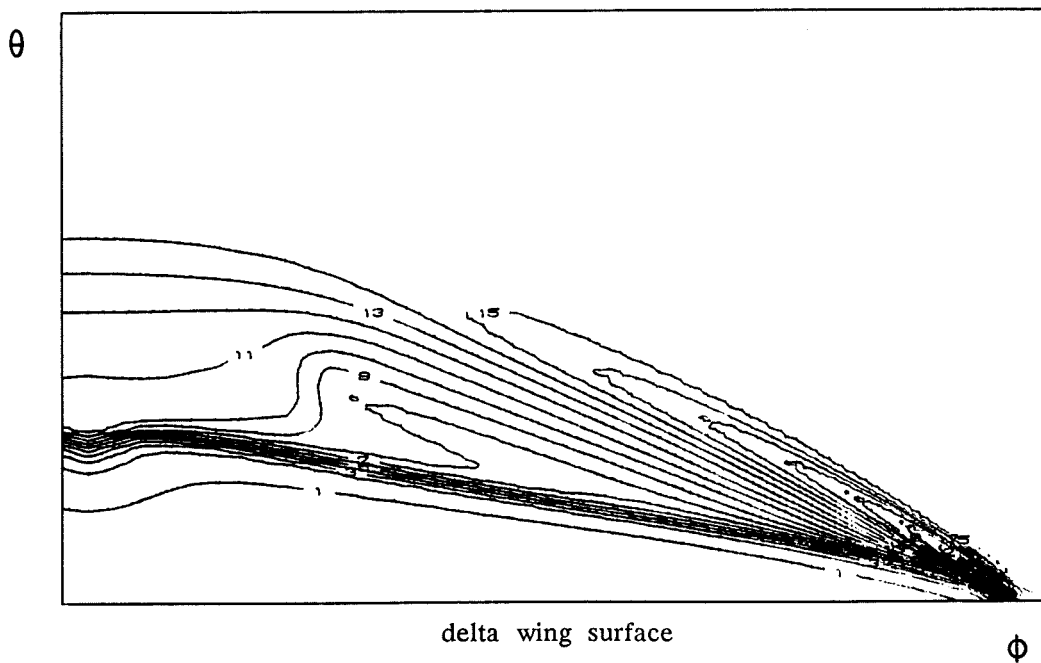


Fig. 4.11(d) Density Contours

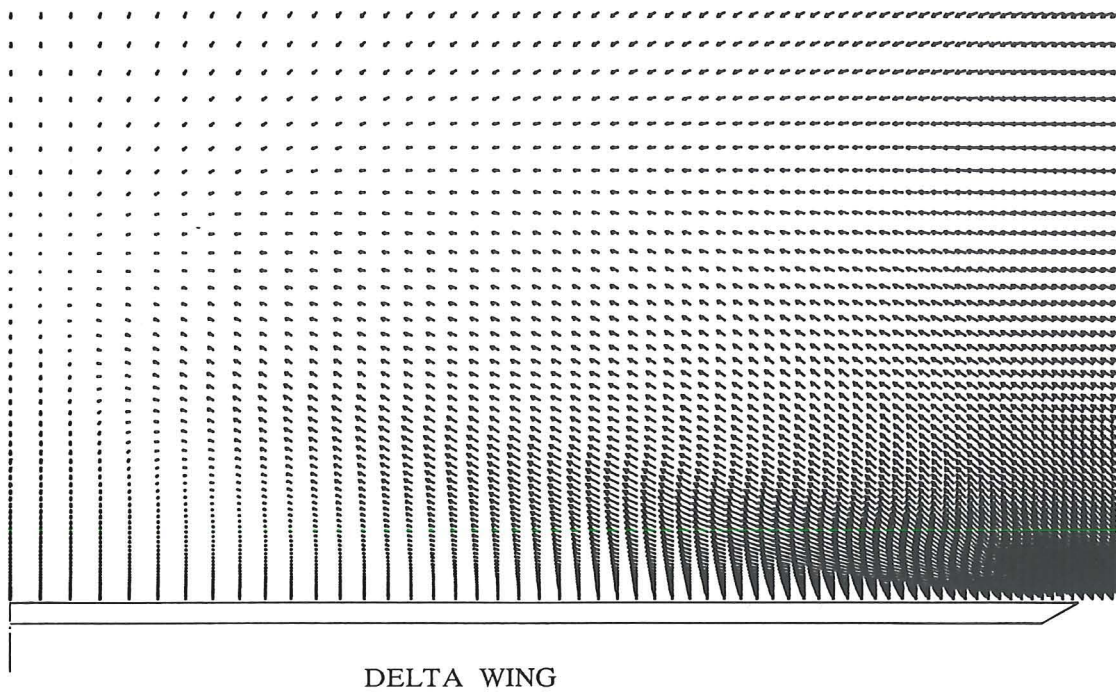


Fig. 4.12 Results for Delta Wing Case at  $\alpha = 15^\circ$

(a) Crossflow Velocity - Overall View

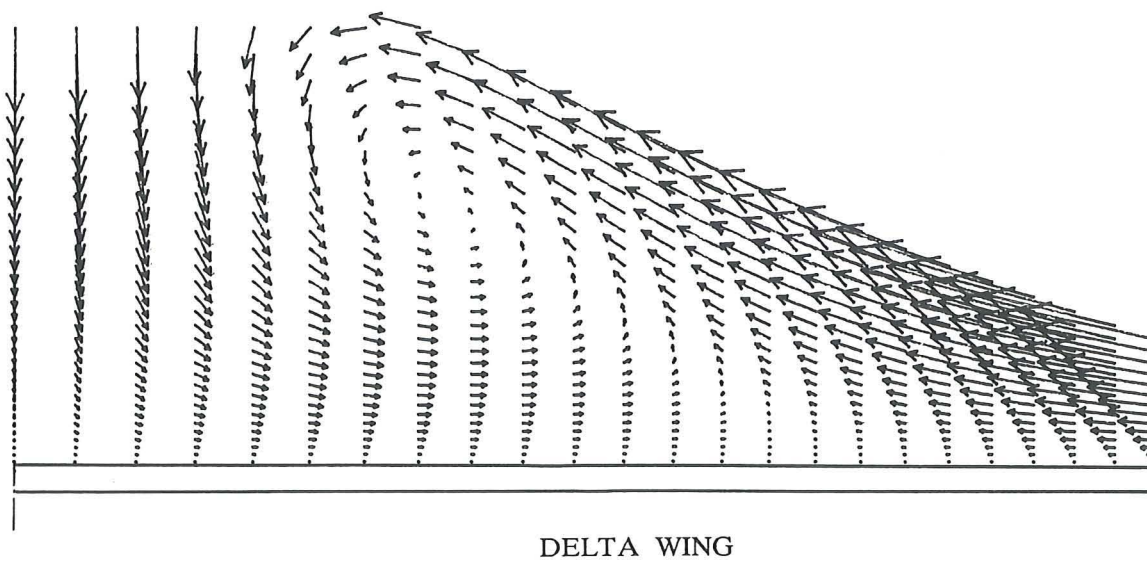


Fig. 4.12(b) Crossflow Velocity - Details near Central Line

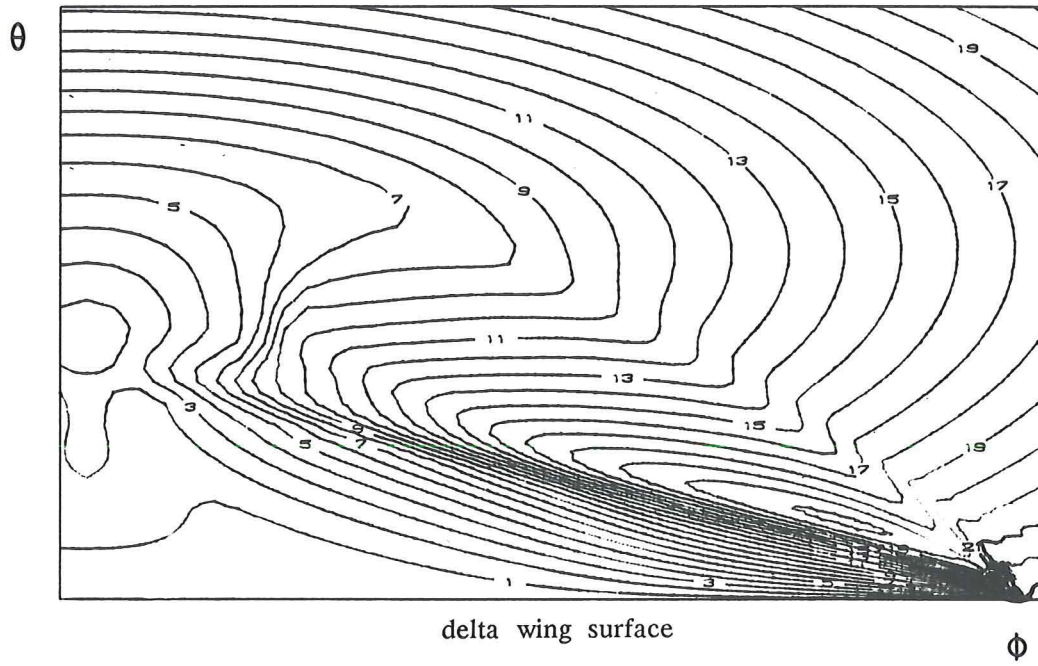


Fig. 4.12(c) Crossflow Mach Number Contours

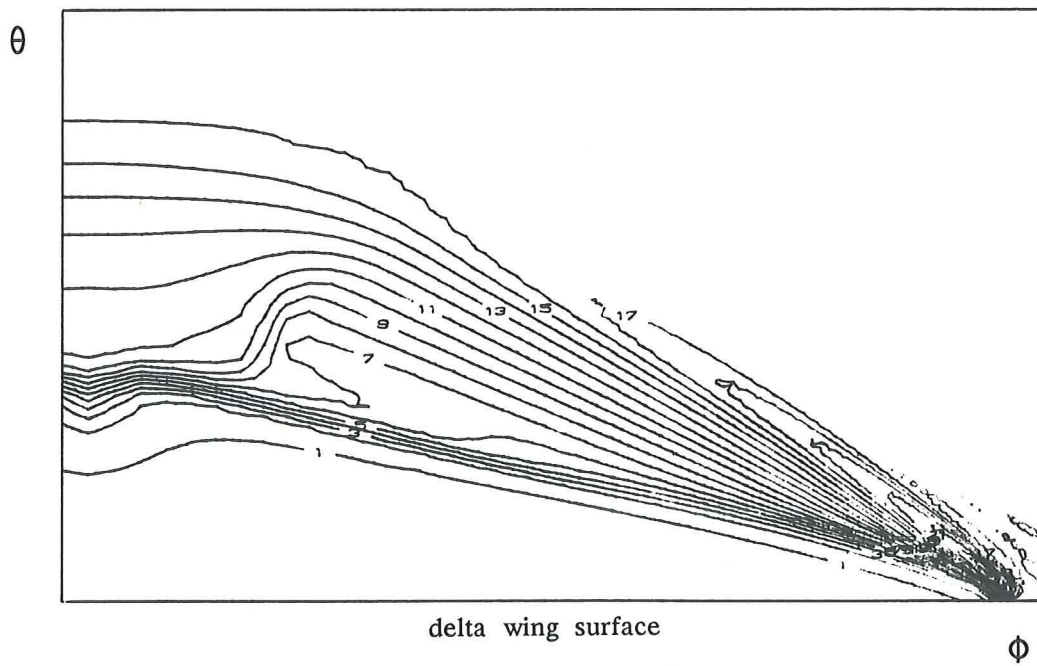


Fig. 4.12(d) Density Contours

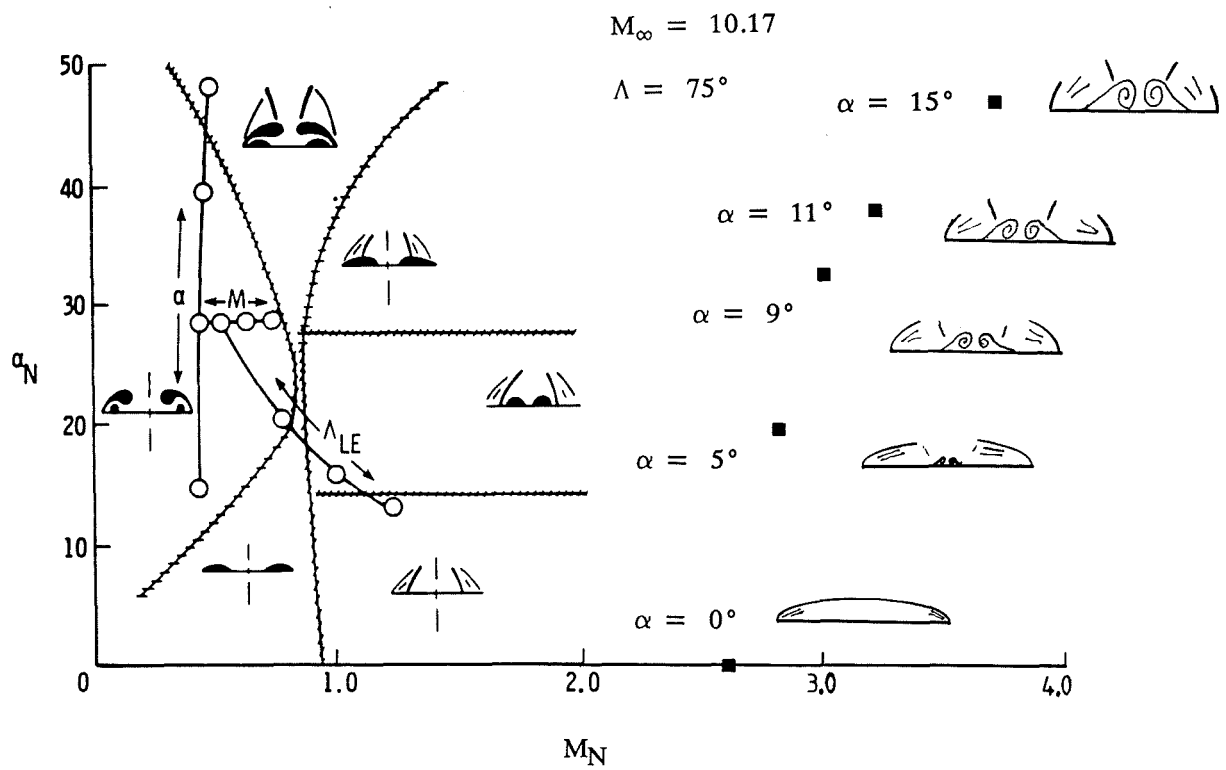


Fig. 4.13 Miller & Wood's Classification and the Present  
 Simulation of Delta Wing Flows

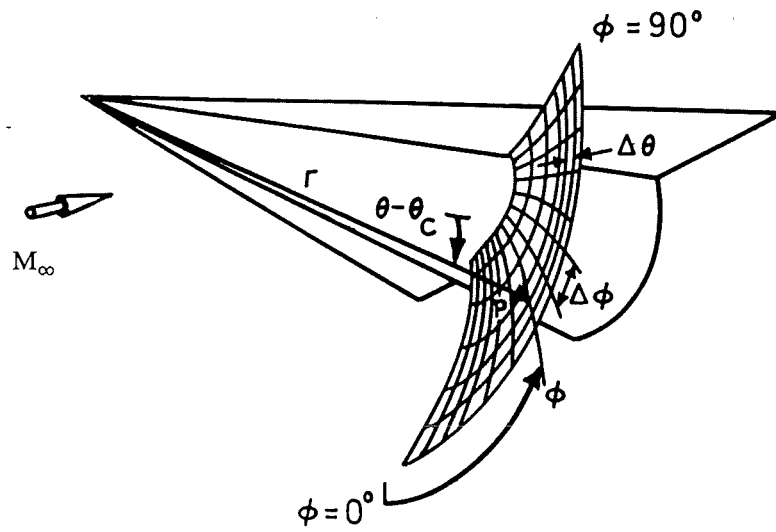


Fig. 4.14 Cone-Delta-Wing Combination Geometry  
and Solution Surface

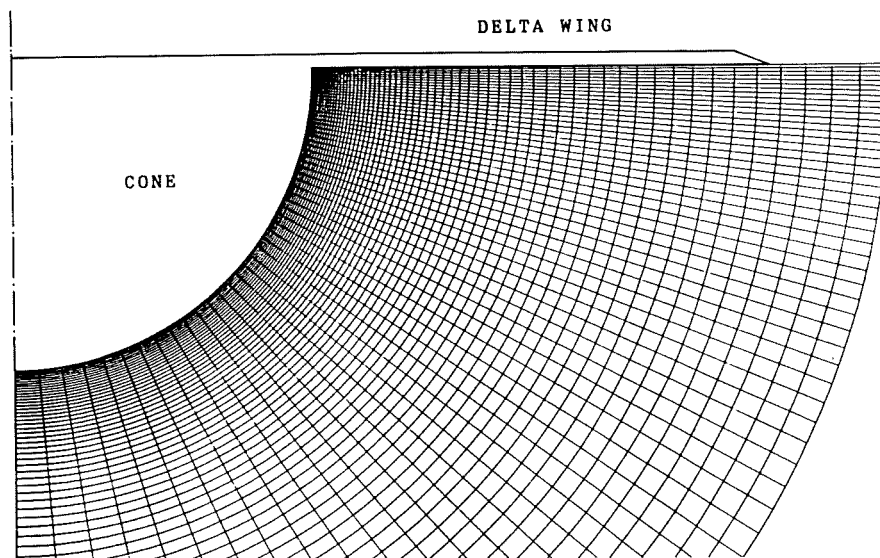


Fig. 4.15 Mesh System for Cone-Delta-Wing Combination Case

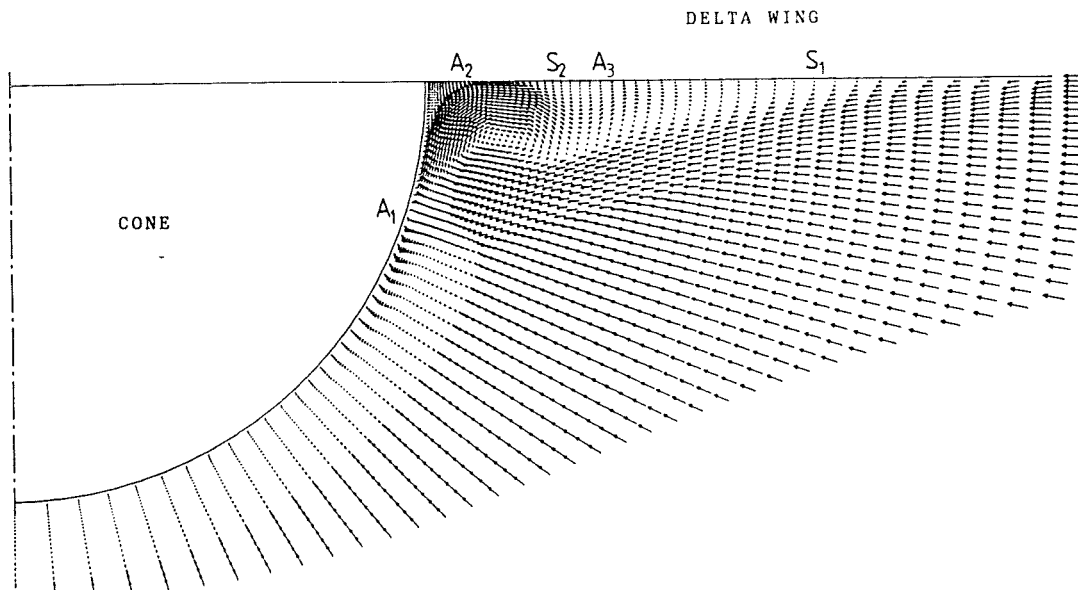


Fig. 4.16 Results for Cone-Delta-Wing Combination Case

Windward Side at  $\alpha = 0^\circ$

(a) Crossflow Velocity - Overall View

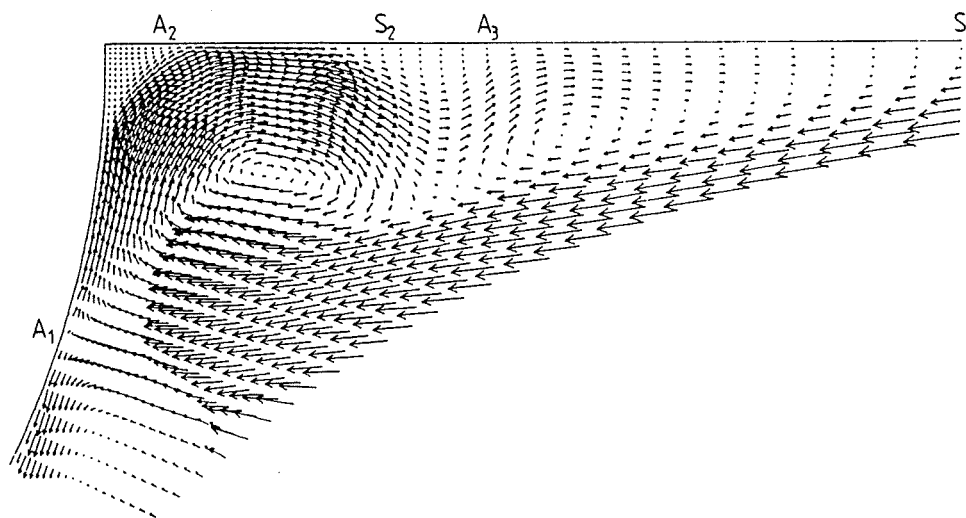


Fig. 4.16(b) Crossflow Velocity -

Details near the Junction

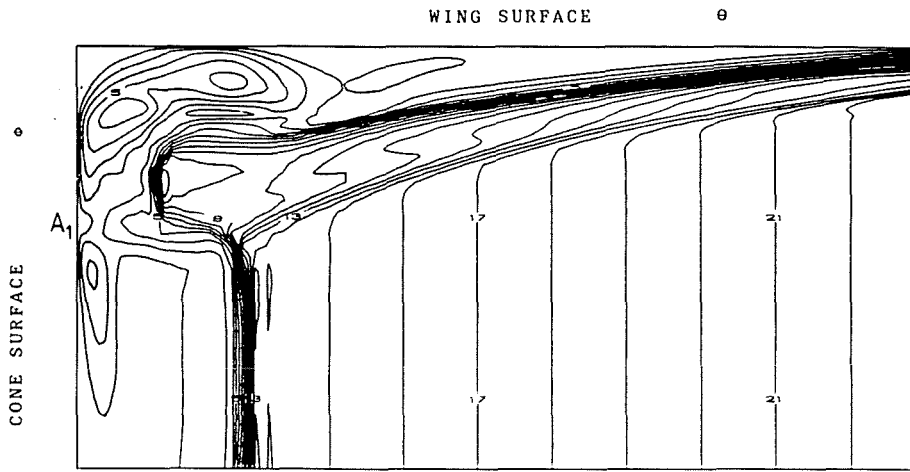


Fig. 4.16(c) Crossflow Mach Number Contours

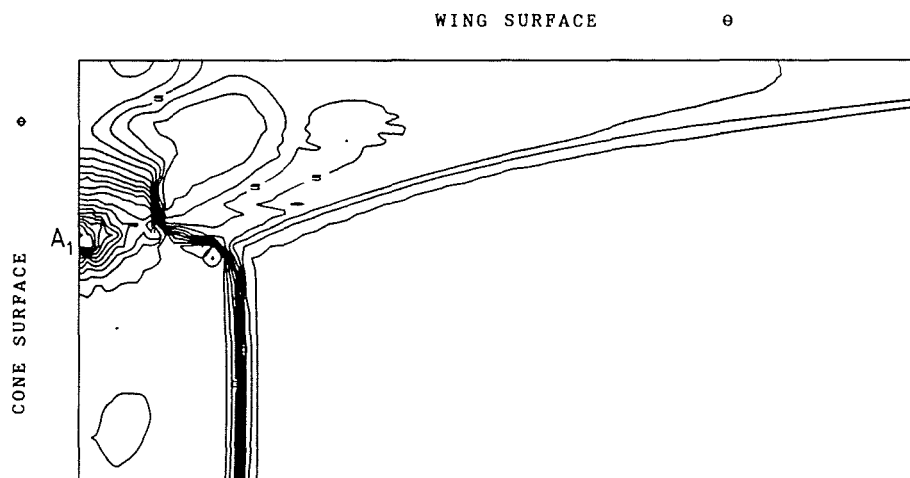


Fig. 4.16(d) Pressure Contours

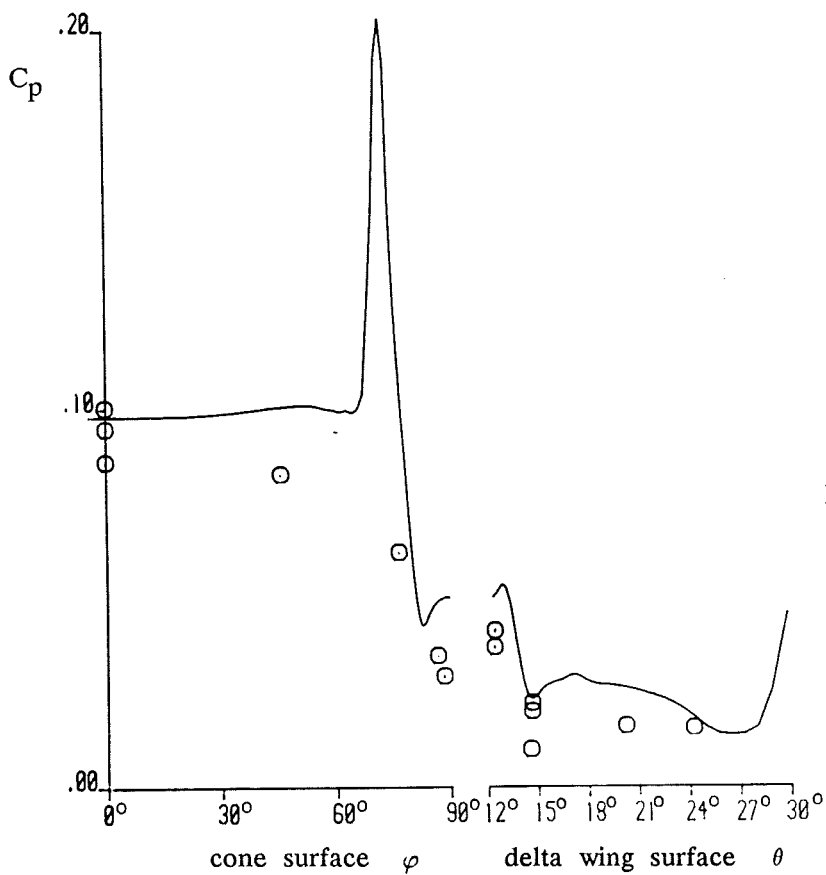
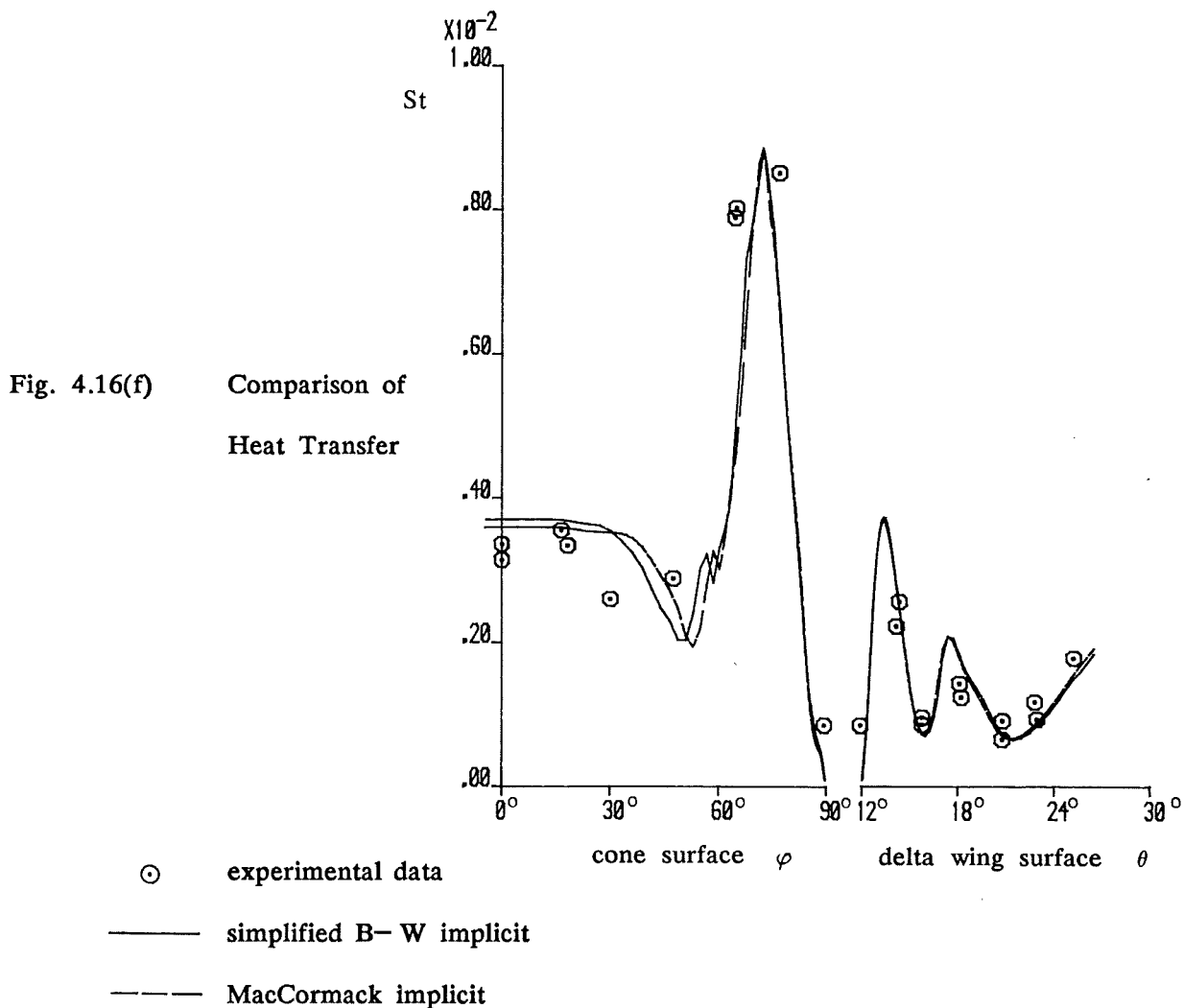


Fig. 4.16(e) Comparison of Wall Pressure



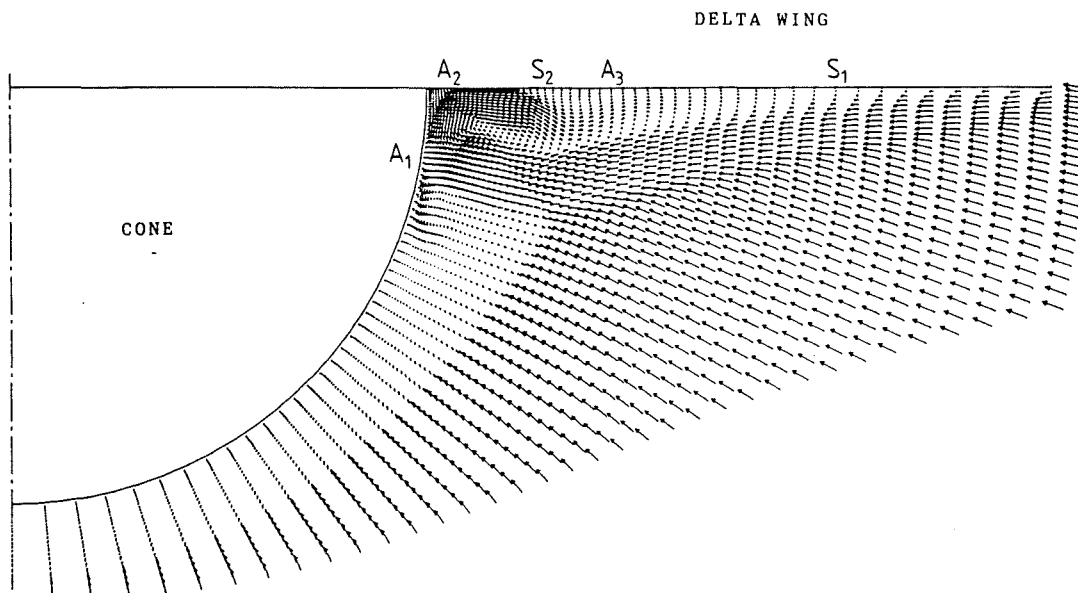


Fig. 4.17 Results for Cone-Delta-Wing Combination Case

Wingward Side at  $\alpha = 5^\circ$

(a) Crossflow Velocity - Overall View

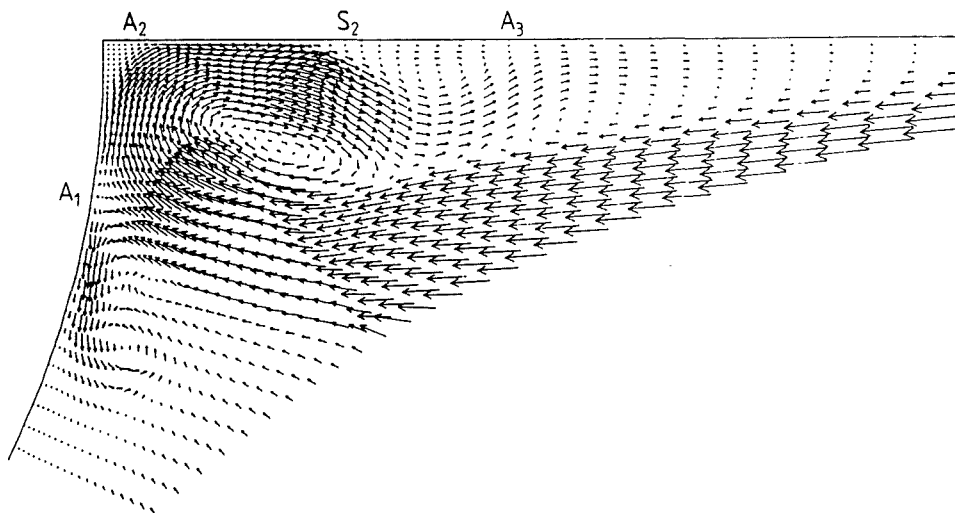


Fig. 4.17(b) Crossflow Velocity -

Details near the Junction

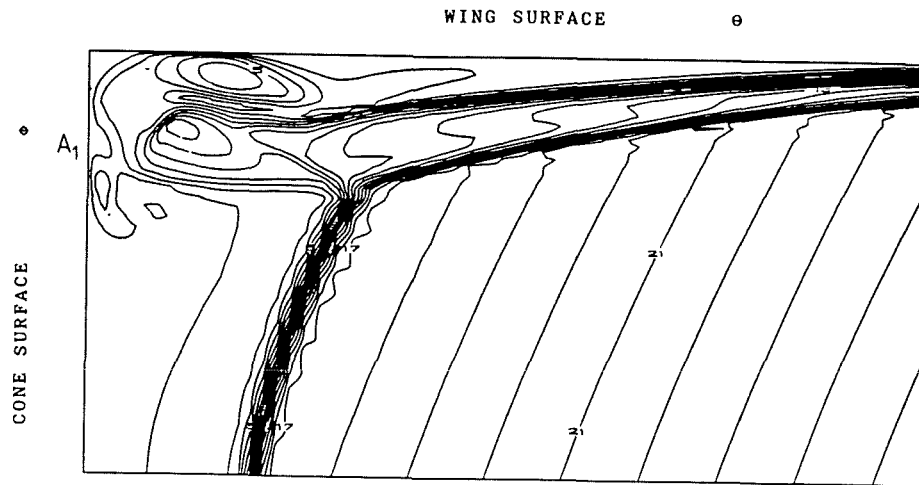


Fig. 4.17(c) Crossflow Mach Number Contours

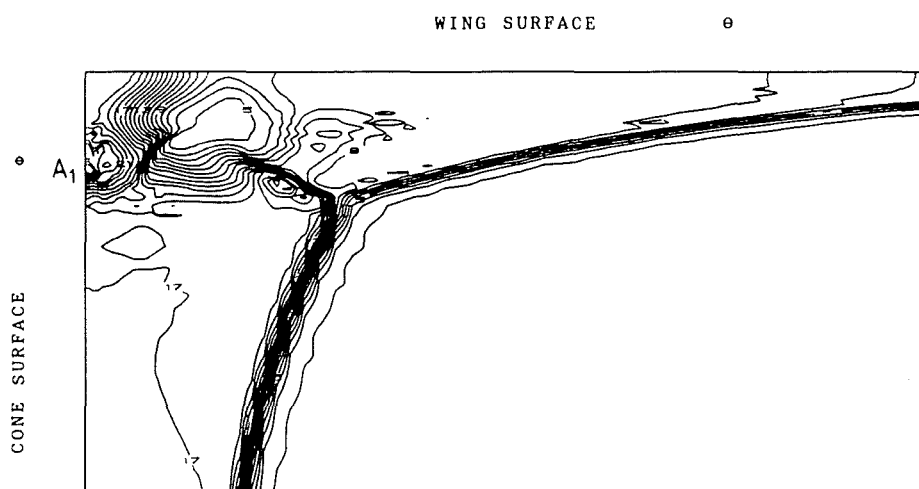


Fig. 4.17(d) Pressure Contours

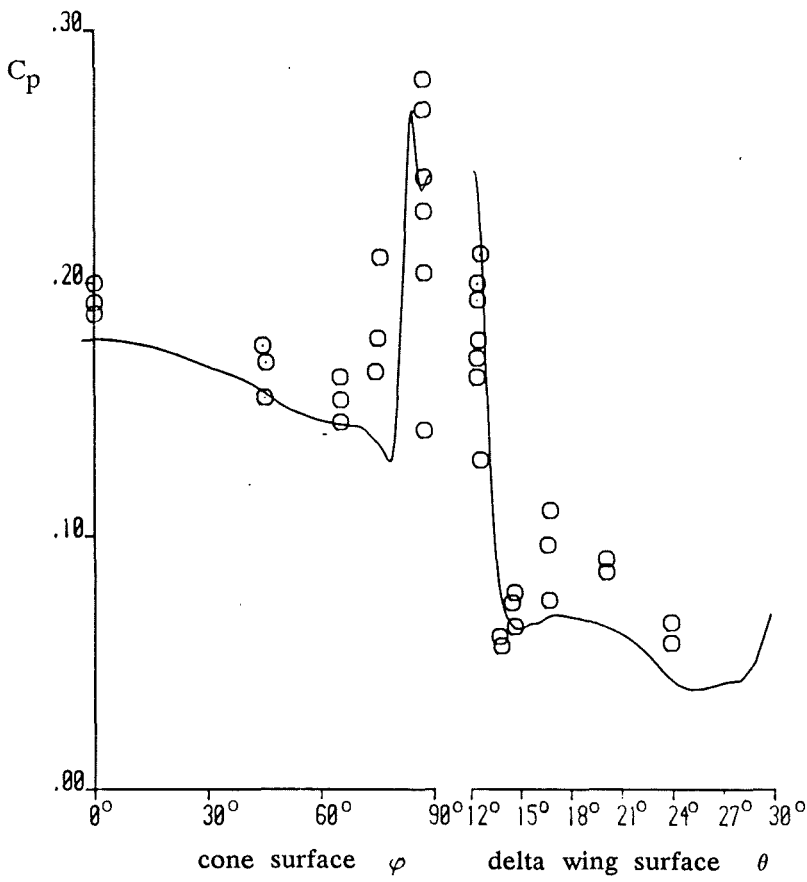


Fig. 4.17(e) Comparison of Wall Pressure

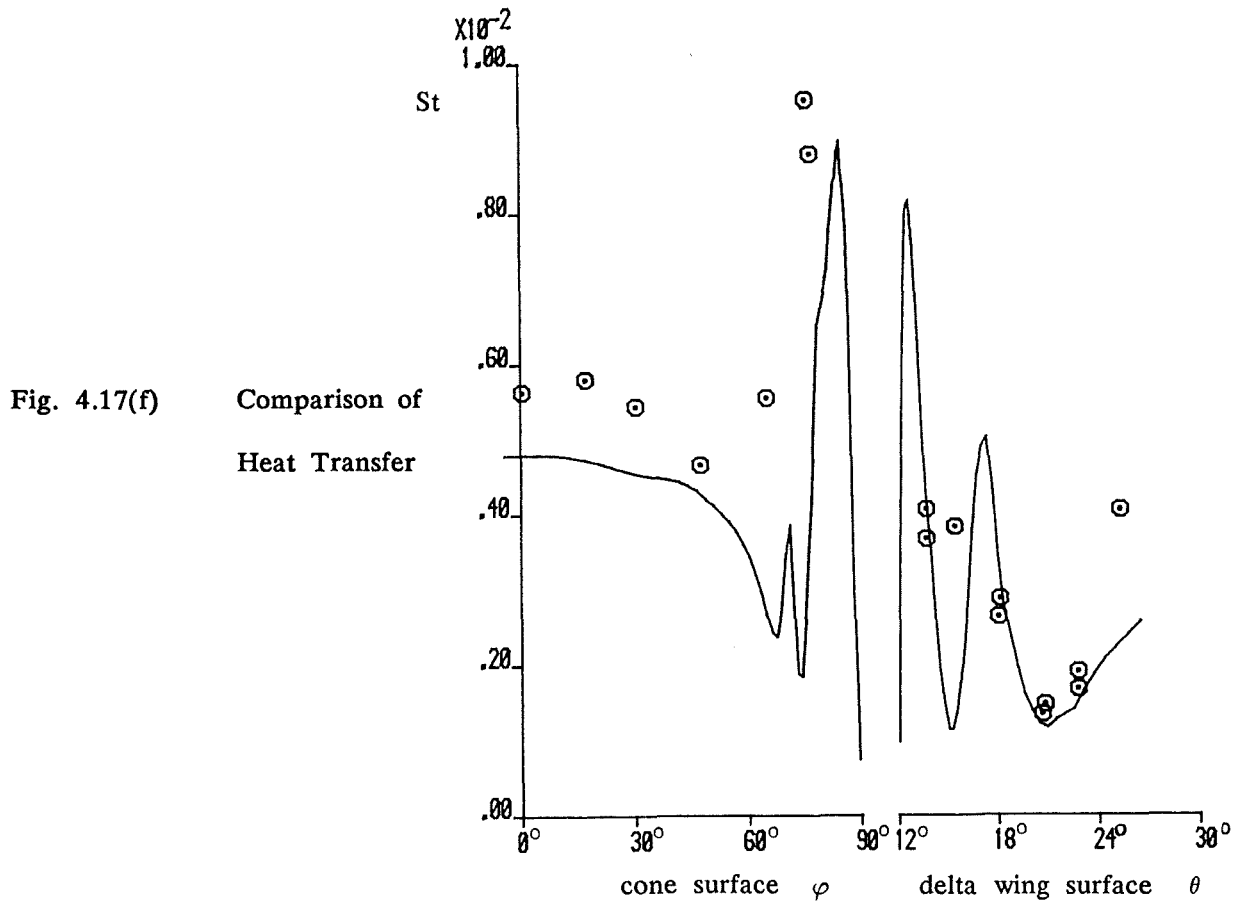


Fig. 4.17(f) Comparison of Heat Transfer

⊙ experimental data  
 — computation

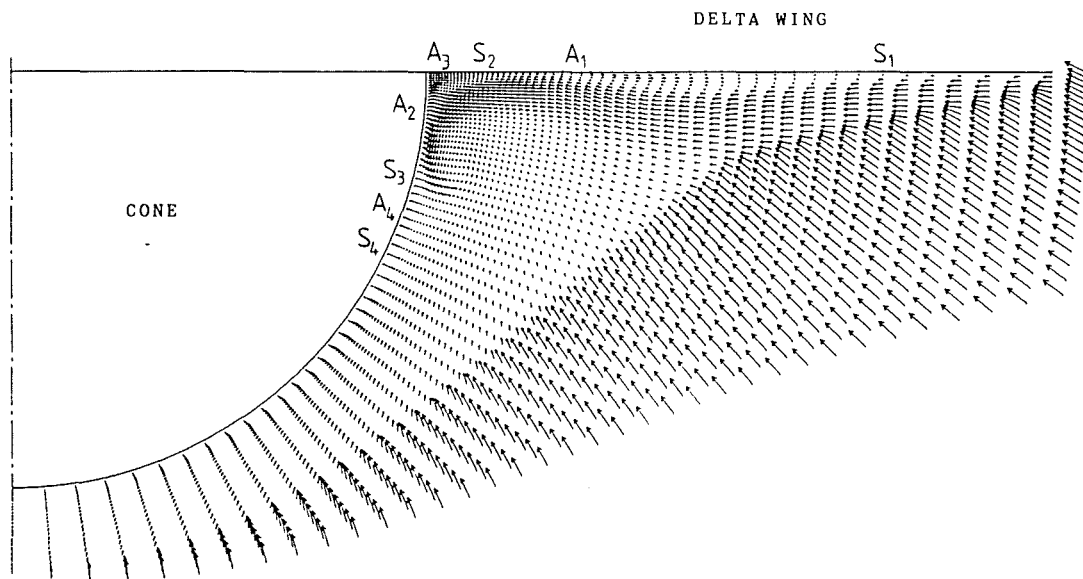


Fig. 4.18 Results for Cone-Delta-Wing Combination Case  
Windward Side at  $\alpha = 15^\circ$

(a) Crossflow Velocity - Overall View

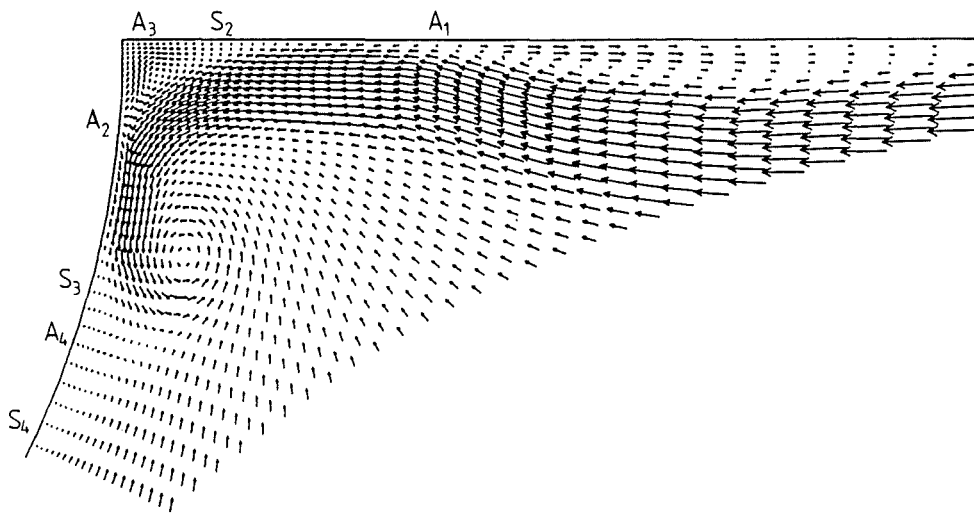


Fig. 4.18(b) Crossflow Velocity -  
Details near the Junction

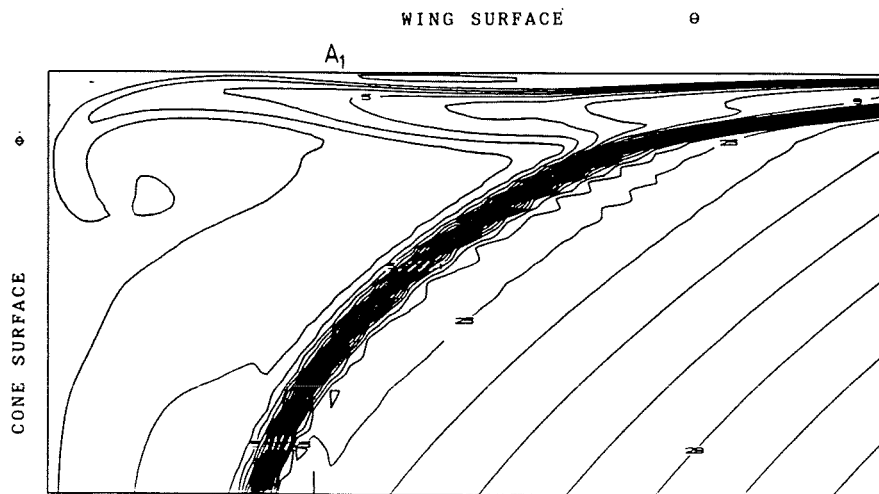


Fig. 4.18(c) Crossflow Mach Number Contours

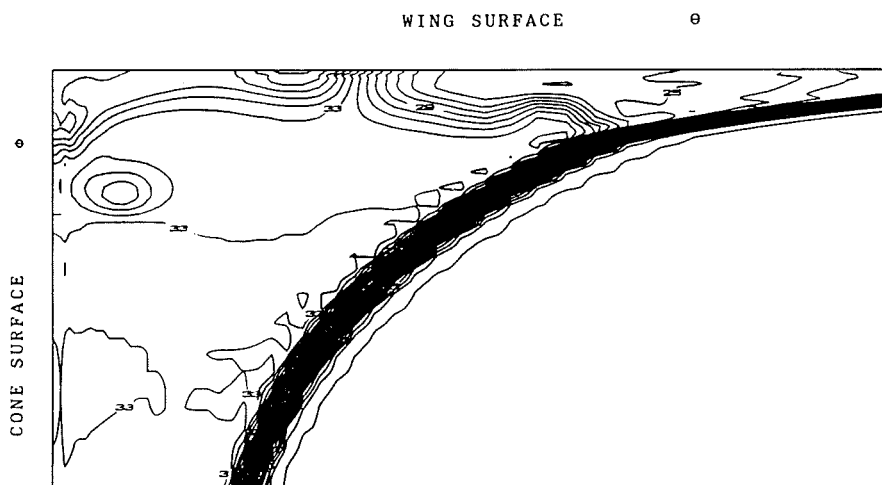


Fig. 4.18(d) Pressure Contours

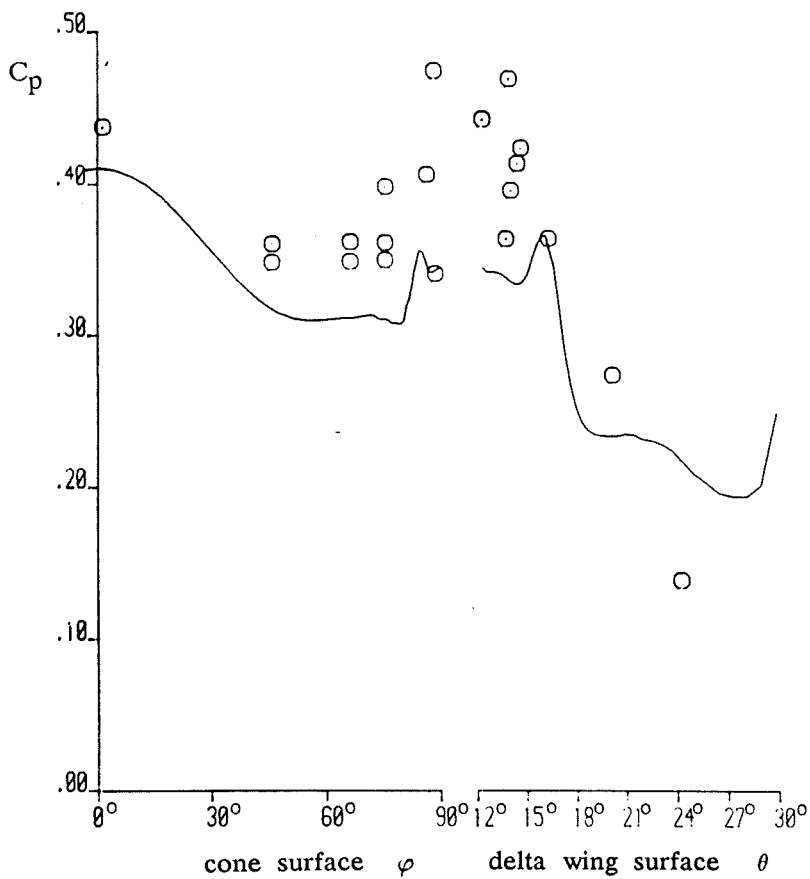
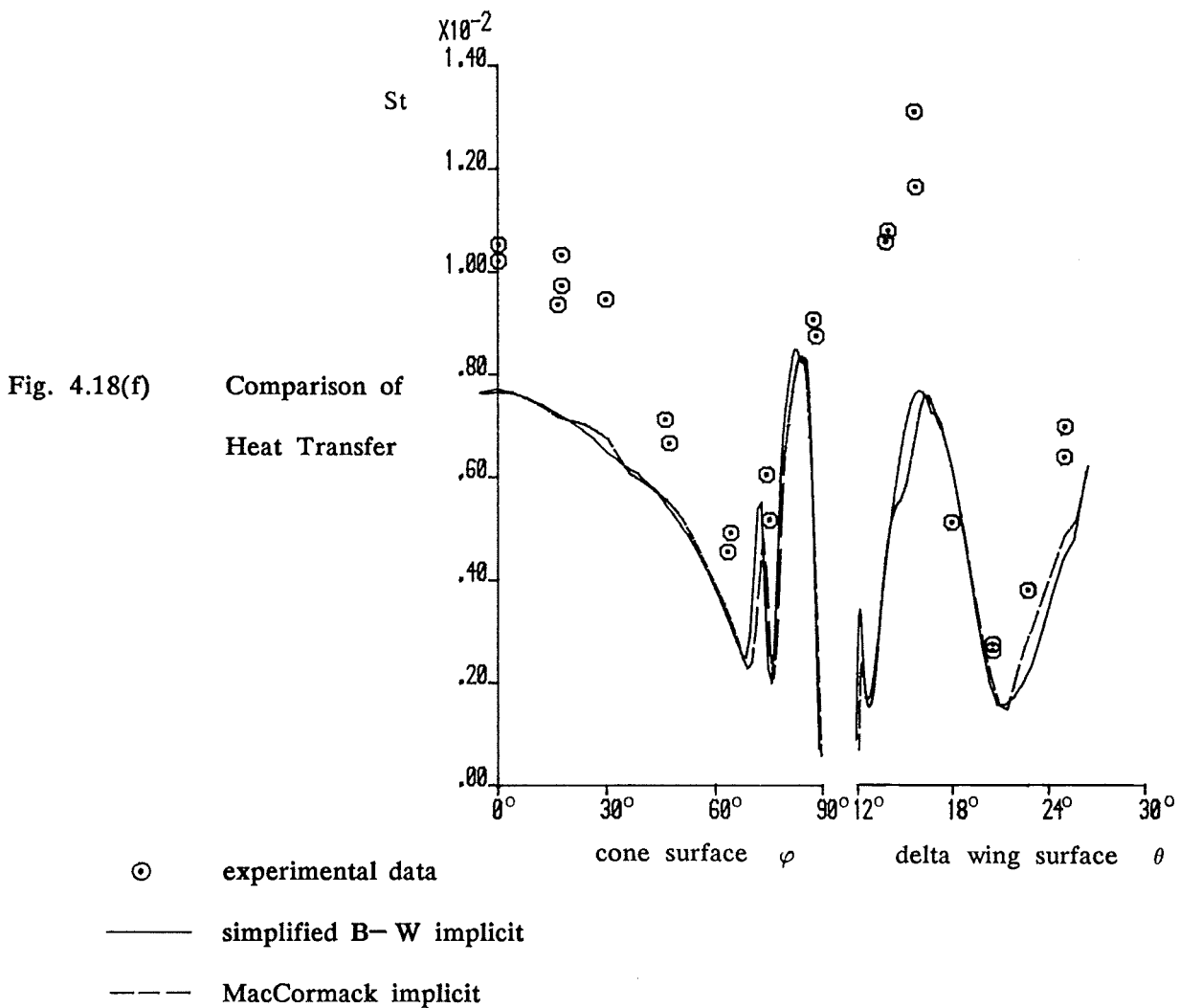
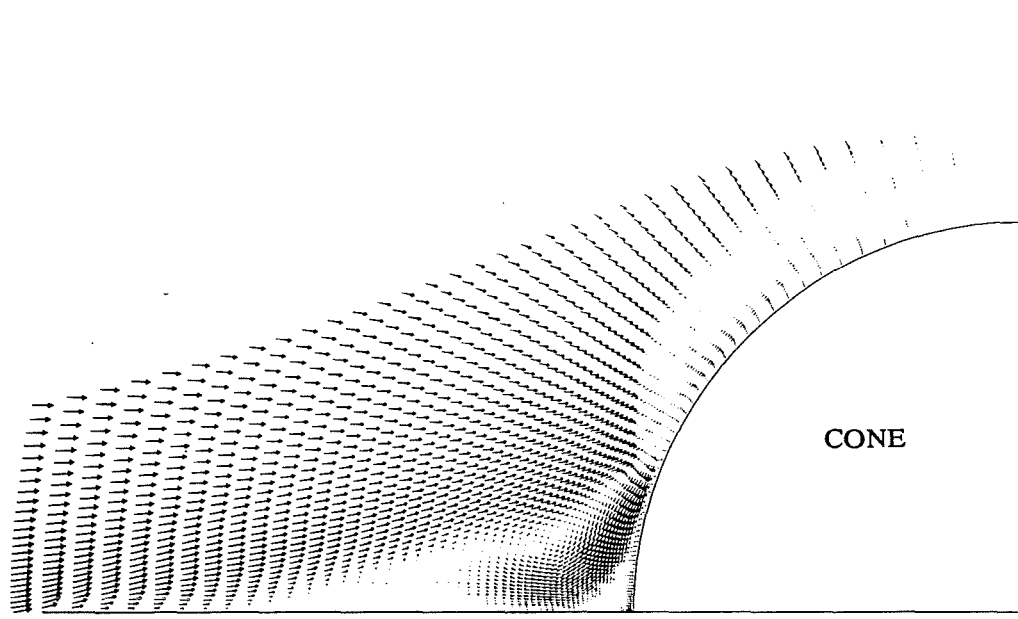


Fig. 4.18(e) Comparison of Wall Pressure

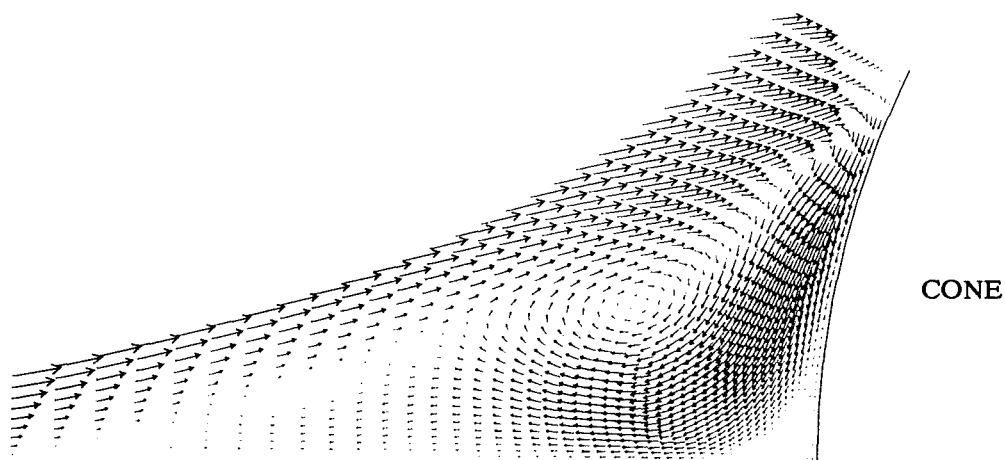




DELTA WING

Fig. 4.19 Results for Cone-Delta-Wing Combination Case  
Leeward Side at  $\alpha = 5^\circ$

(a) Crossflow Velocity - Overall View



DELTA WING

Fig. 4.19(b) Crossflow Velocity -  
Details near the Junction

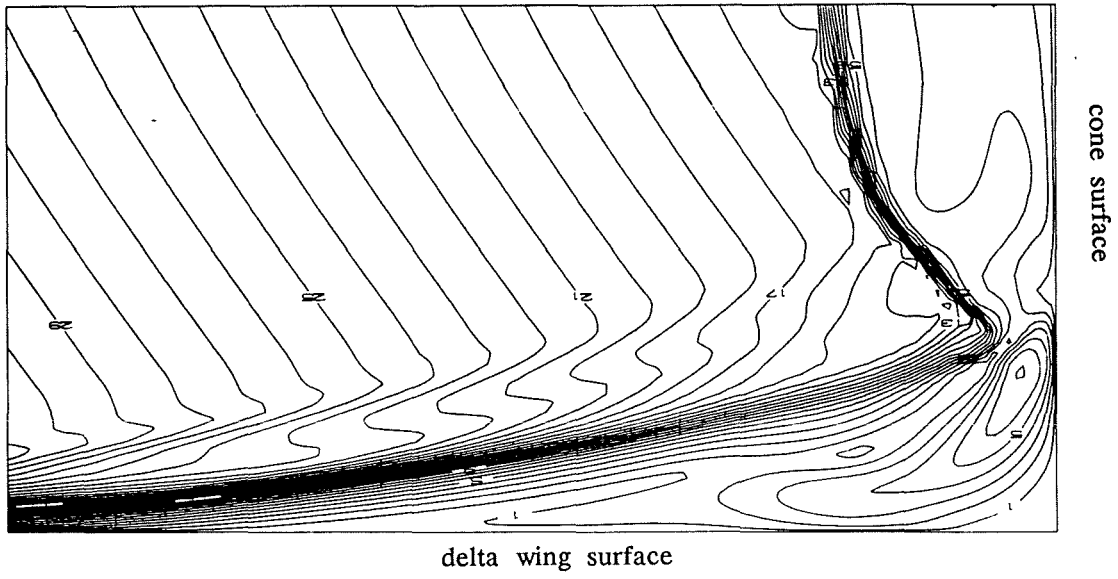


Fig. 4.19(c) Crossflow Mach Number Contours

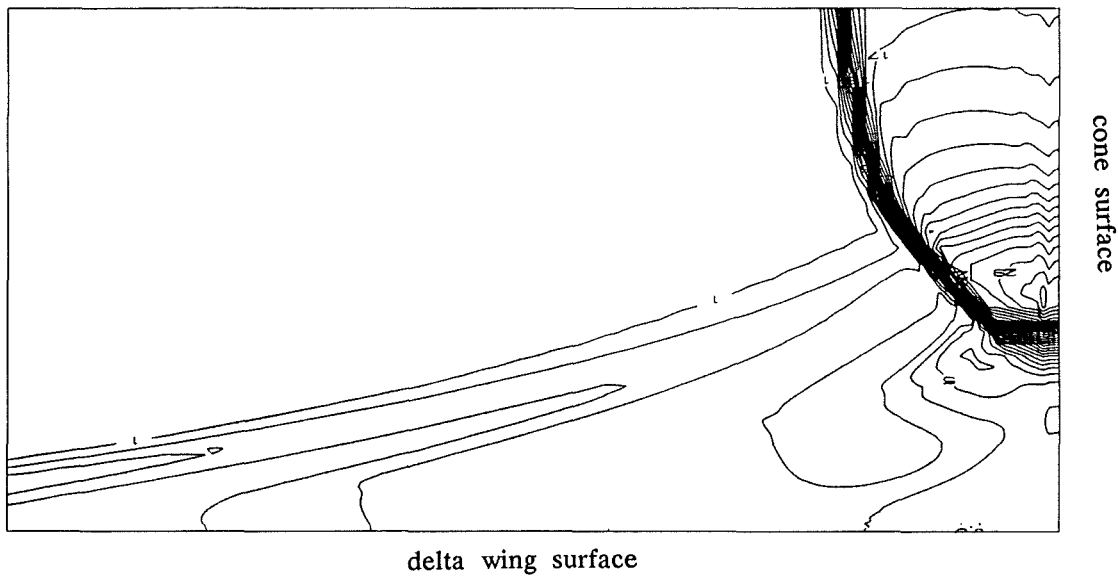


Fig. 4.19(d) Pressure Contours

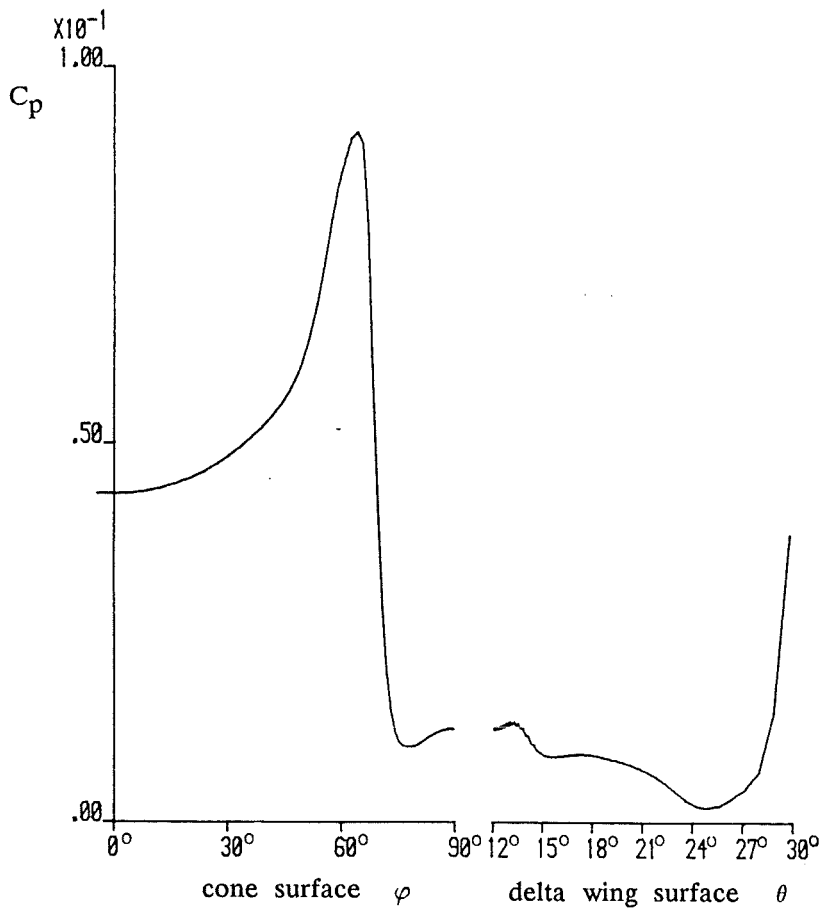


Fig. 4.19(e) Wall Pressure

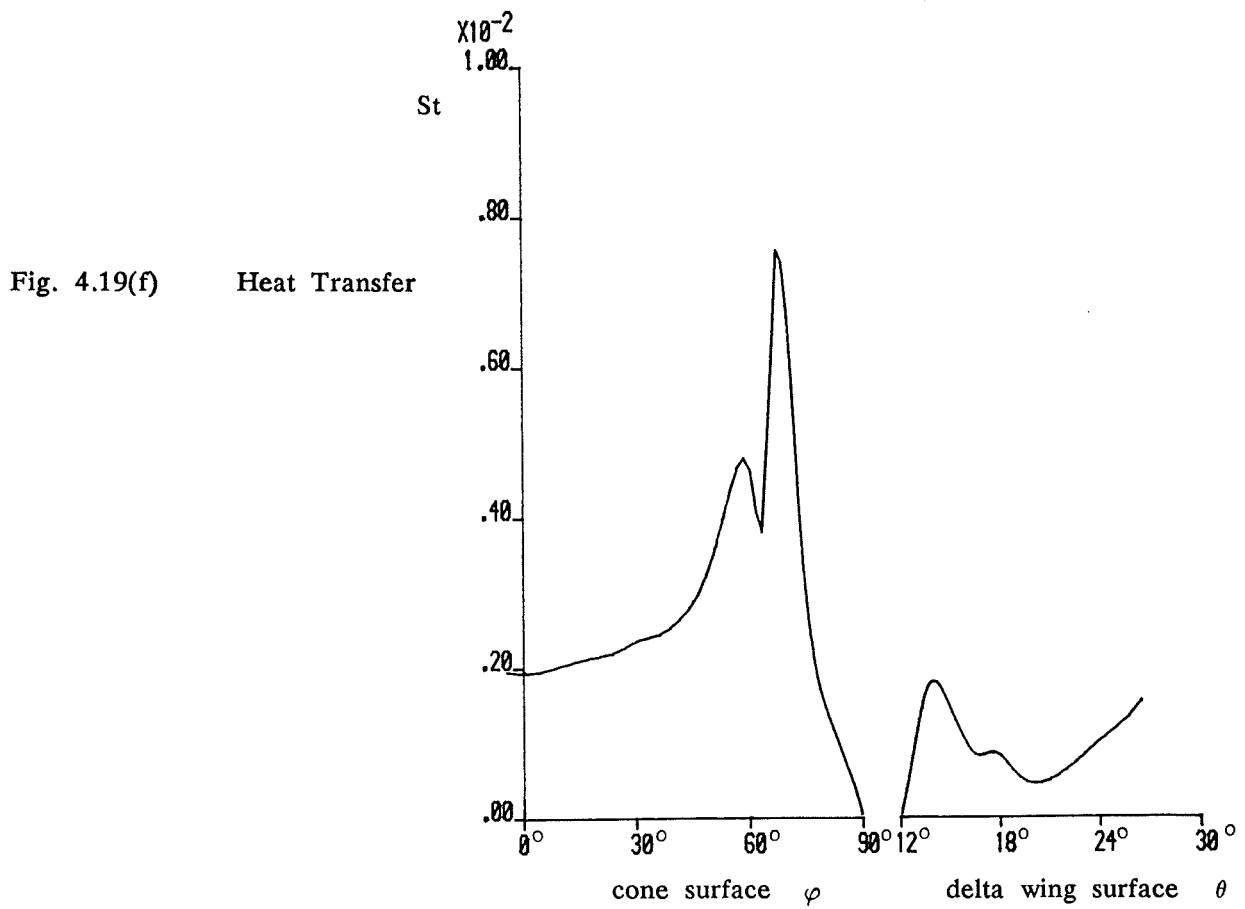


Fig. 4.19(f) Heat Transfer

DELTA WING

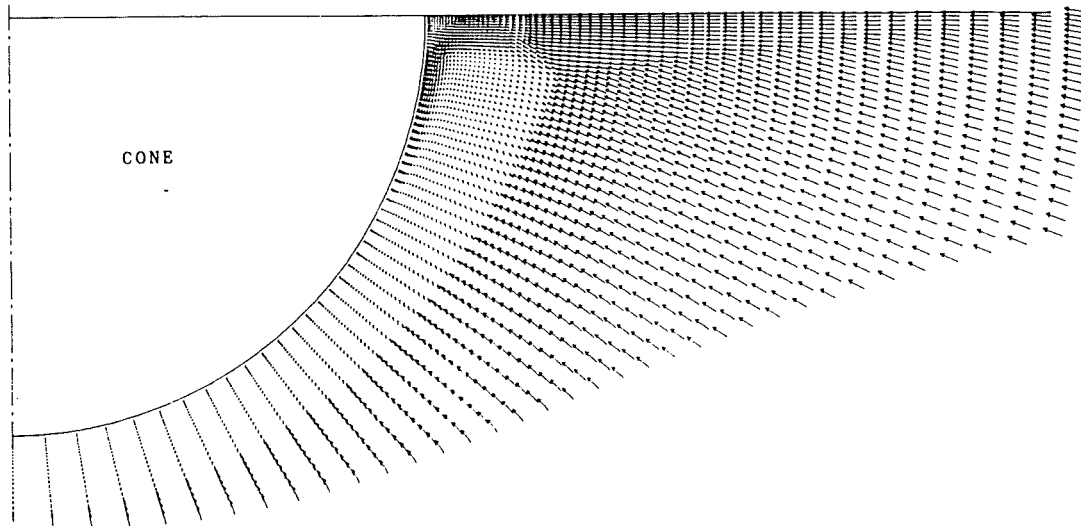


Fig. 4.20 Results for Cone-Delta-Wing Combination Case  
Windward Side at  $\alpha = 5^\circ$ ; Euler Solution  
(a) Crossflow Velocity - Overall View

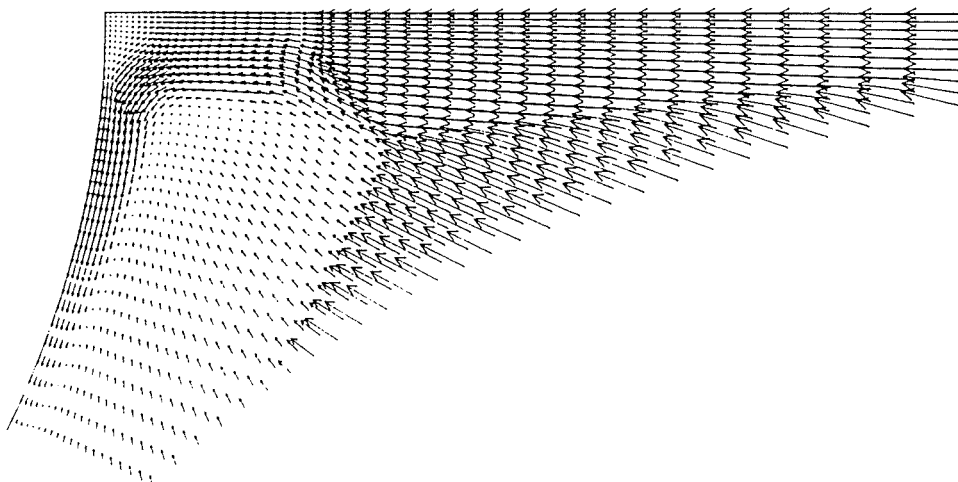


Fig. 4.20(b) Crossflow Velocity -  
Details near the Junction

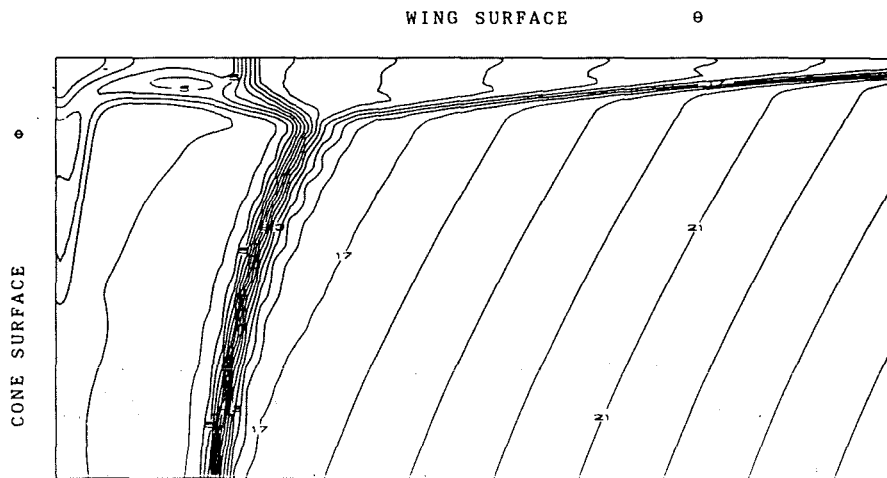


Fig. 4.20(c) Crossflow Mach Number Contours

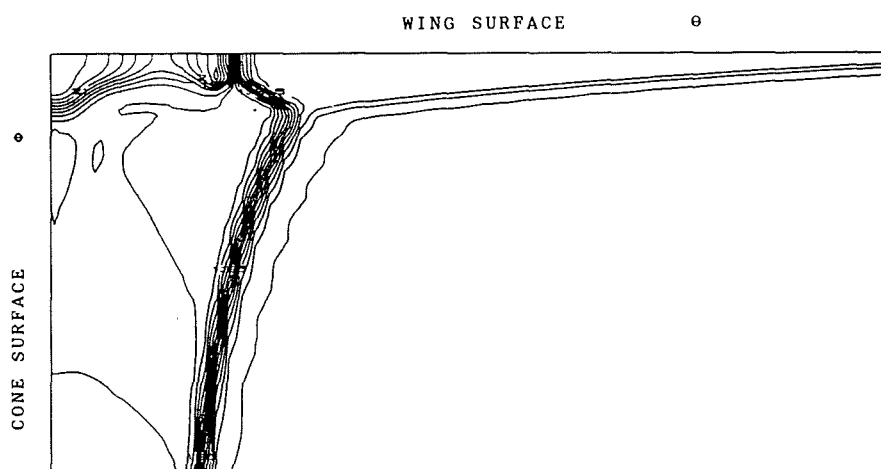


Fig. 4.20(d) Pressure Contours